Transient rheology model of the oceanic asthenosphere inferred from the 2012 Indian Ocean earthquake using a finite element method

有限要素法を用いて 2012 年インド洋地震から推定した海洋アセノスフェアの非定常レオロジーモデル

Cecep Pratama

Graduate School of Environmental Studies,

Nagoya University

2018

Transient rheology model of the oceanic asthenosphere inferred from the 2012 Indian Ocean earthquake using a finite element method

有限要素法を用いて 2012 年インド洋地震から推定した海洋アセノスフェアの非定常レオロジーモデル

Cecep Pratama

A dissertation for the degree of Doctor of Science

Department of Earth and Environmental Sciences,

Graduate School of Environmental Studies,

Nagoya University

2018

Acknowledgements

In the name of God, the Most Gracious, the Most Merciful

I bear witness that there is no God except Allah Subhana Wa Ta'ala, and I bear witness that Muhammad Sallallahu Alayhi Wa Salaam is the Messenger of Allah.

I would like to express my sincere gratitude and regards to all the people who helped me during my study and make all this work achievable. The first and foremost person is my advisor Dr. Takeo Ito, for his knowledge, support, guidance and encouragement to accomplish my study. I learn from him in a countless discussion of Earth Science both theoretically and experimentally. I had a joyful experience during my field observation with him. I am deeply grateful to Dr. Takeshi Sagiya, for sharply, carefully and intelligently review my research through seminar and personal discussion. I am deeply appreciated by my thesis committee members, Dr. Yamaoka Koshun and Dr. Takao Tabei for their valuable questions and comments. I wish to thank all teachers, researchers and students in the Earth and Planetary Dynamics department for valuable discussion and help. I owe thanks to Dr. Irwan Meilano for giving a nice recommendation to study Tectonic Geodesy at Nagoya University, Japan. I am grateful to the Ministry of Education, Sports, Science, and Technology of Japan for remarkable funding for my living in Japan.

I would like to thank the researchers and institutes who provide important data for my study. I would like to thank Dr. Brad Aagaard and the team of Computational Infrastructures of Geodynamics for helpful advice and discussion on the use of PyLith, where the code is freely available for geoscience community. Dr. Emma Hill for providing me with coseismic fault model and discussion during American Geophysical Union Fall Meeting. Dr. Sri Widiyantoro for providing me with the 3D sub-surface velocity structure.

Finally, I would like to thank my lovely family and my parents for their endless support and pray for me. My wife, Novita, for her sharing, caring and sacrifice through any occasion with me event it severely cost her life. And also to my children, Azka, Aziz, Azrina who make our beloved home become warmer and colorful.

Abstract

Plate tectonics are extensively considered to play a major role in the global dynamics and evolution of the Earth. The rheological properties, such as the viscosity of the oceanic asthenosphere and thickness of the oceanic lithosphere, exhibit a first-order influence on the nature of plate tectonics. However, rheological structures under the ocean are still poorly understood. Large oceanic intraplate earthquakes provide opportunities to investigate the rheological properties of the lithosphere and asthenosphere under the ocean. Rheological properties are important to understand the plate tectonics and the driving forces of plate movement.

On April 11, 2012, an Mw 8.6 earthquake struck approximately 400 km off the west coast of northern Sumatra that was followed by an Mw 8.2 earthquake two hours later. The 2012 Indian Ocean earthquake sequence, which was the largest intraplate earthquake in the recorded history, yielded seismic moments of 1.2–1.3 × 10^{22} and 0.2–0.3 × 10^{22} N m for the Mw 8.6 and Mw 8.2 earthquakes, respectively. Large oceanic intraplate earthquakes are extremely rare and provide valuable opportunities to investigate the rheological properties under the ocean.

In this dissertation, I analyzed the two-year postseismic (04/11/2012–04/10/2014) motion that was caused by the 2012 Indian Ocean earthquake sequence to reveal the rheological structure. A three-dimensional spherical-earth finite-element model was constructed, in which a heterogeneous subducting slab included due to the complex subduction region. In the initial two months of the postseismic stage, the continuous Global Navigation Satellite System (GNSS) data pattern in northern

Sumatra clearly exhibited a rapid transient motion. Here, we investigate the necessary contribution of transient rheology in the oceanic asthenosphere to reproduce the short- and long-term transitional features of the postseismic signals.

I conducted a systematic grid search of several rheological models to estimate the oceanic asthenospheric viscosity and the oceanic lithospheric thickness. First, I modeled the oceanic asthenospheric viscosity as a Maxwell model, which has also been assumed in previous studies. I obtained an optimal rheological model that comprised 5×10^{17} Pa s of the Maxwell viscosity and 70 km of the oceanic lithospheric thickness. However, this optimal model cannot explain the transient motion and significantly underestimates the observations in the postseismic signals that were observed during the initial two months. This indicates that the assumption of the Maxwell model is insufficient to explain the rapid transitional changes.

Second, I modeled the oceanic asthenospheric viscosity using a Burgers model, which represents a large change in the viscosity from a low transient Kelvin viscosity to a steady-state Maxwell viscosity. I obtained an optimal rheological model consisting of a Kelvin viscosity of 5×10^{16} Pa s, a Maxwell viscosity of 1×10^{18} Pa s, and an oceanic lithospheric thickness of 75 km. This model could explain most of the rapid postseismic transient motions. This result exhibits that transient rheology is necessary to reproduce the rapid changes. However, the vertical component of the model slightly overestimates the late stage (>1 year). Additional deformation, which caused the subsidence, is also necessary. This indicates that the afterslip was likely to be detected in northern Sumatra.

In the third model, I combined the Burgers viscoelastic relaxation model in the oceanic asthenosphere with stress-driven afterslip in the lithosphere. The afterslip was modeled based on the coseismic stress change. Based on this combined mechanism, I

obtained an optimal rheological model with an oceanic lithospheric thickness of 75 km, an asthenospheric Kelvin viscosity of 1×10^{17} Pa s, and a Maxwell viscosity of 3×10^{18} Pa s. This third model exhibits a better agreement with our GNSS dataset and reduces the misfit by 37% as compared to the second model. This observation is consistent with that of Masuti et al. (2016) who assumed an afterslip a priori. However, my result is contrary with that of Hu et al. (2016) who found that the afterslip worsens the model.

The third model, which is the best-fit rheological model, is able to explain the rapid changes in the horizontal component and to moderate rapid transient uplift in the fore-arc within the initial two months after the earthquake. The transient Kelvin viscosity and afterslip can primarily explain the early stage of the postseismic deformation during the first two months. Additionally, we observed that the coupled transient viscoelastic relaxation and afterslip were necessary to model the postseismic deformation process after the earthquake sequence.

Transient rheology plays an essential element to accommodate transient stress due to coseismic stress change. Our best-fit rheology model consists of Kelvin and Maxwell viscosities. The obtained Maxwell viscosity is similar with the viscosity derived from postglacial rebound data (Paulson and Richards, 2009; James et al., 2009) and geoid data (Schaber et al., 2009) that are not affected by the transient stress of coseismic stress change. Adding to this, the Maxwell viscosity and thickness of the asthenosphere under the ocean are important factors to explain the shear stress that was induced by the plate motion. Based on the best-fit model, the estimated shear stress induced by the plate motion is approximately 0.03 MPa, which is below the upper bound limit 0.1 MPa from the observed stress state within the middle-to-old oceanic lithosphere (Wiens and Stein, 1985). Additionally, the estimated 75-km

lithospheric thickness implied that the 2012 Indian Ocean earthquake occurred in a rigid cold oceanic plate that exhibited an age of 40–60 Myr, which was consistent with the thickness that was derived from the thermal structure studies (McKenzie et al., 2005) and the observed bottom of oceanic lithosphere in other oceanic regions within the same plate age deduced from seismic observation (Kawakatsu et al., 2009).

Finally, through this study, the rheological model that was combined with the stress-driven afterslip was estimated based on two years of the GNSS postseismic signals resulting from the 2012 Indian Ocean earthquake sequence. The best-fit model in this study is able to reproduce the short- and long-term transitional features of the postseismic signals. Therefore, the results indicate that large changes in the viscosity and afterslip are essential to reproduce the rapidly changing motion of the postseismic deformation in the middle-field area. In terms of plate tectonics, the results of these rheological structures demonstrate the appropriate magnitude of the weak asthenosphere that can be used as a lubricant layer to maintain the driving force of plate movement.

Table of contents

List of Tables

List of Figures

Glossary of Abbreviations

3-D	Three Dimensional
AGNeSS	Aceh GNSS Network for Sumatran fault System
CIG	Computational Infrastructure for Geodynamics
CODE	Center for Orbit Determination in Europe
ECEF	Earth Fixed Earth Centered
EOS	Earth Observatory of Singapore
FE	Finite Element
FES2004	Finite Element Solutions 2004
GCMT	Global Centroid Moment Tensor
GNSS	Global Navigation Satellite System
GPS	Global Positioning System
GRACE	Gravity Recovery and Climate Experiment
IGS	International GNSS Service
ITB	Bandung Institute of Technology
ITRF	International Terrestrial Reference Frame
LIPI	Indonesian Institute of Sciences
NEIC	The United States National Earthquake Information Center
RINEX	Receiver Independent Exchange Format
SRTM	Shuttle Radar Topography Mission
SOPAC	Scripps Orbit and Permanent Array Center
SuGAr	Sumatran GPS Array
UNSYIAH	Syiah Kuala University
USGS	United States Geological Survey

1 Introduction

1.1 Background

The seismic moment and stress that are released by large earthquakes cause extensive and long-lasting postseismic deformation within the lithosphere and asthenosphere. Postseismic motion, which can be detected by geodetic observations, may reflect a large contribution of viscoelastic relaxation in the upper mantle (Wang et al., 2012). This mechanism could explain the rheological properties in the mantle, which are fundamental to understand the plate tectonics.

Plate tectonics are extensively considered to play a major role in the global dynamics and evolution of the Earth. Plate tectonics control most of the geological processes in terrestrial planets. The rheological properties, such as the viscosity of the oceanic asthenosphere and thickness of the oceanic lithosphere, exhibit a first-order influence on the nature of plate tectonics. However, oceanic rheological structures that exist under the Indian Ocean are still poorly understood. Large oceanic intraplate earthquakes provide opportunities to investigate the rheological properties of the lithosphere and asthenosphere under the ocean. Rheological

properties are important to understand the plate tectonics and the driving forces of plate movement.

On April 11, 2012, a large oceanic earthquake (Mw 8.6) struck approximately 150 km to the west of the Sunda Trench off the west coast of northern Sumatra and was followed by a large aftershock (Mw 8.2) that was observed approximately two hours after the main shock (Satriano et al., 2012; Yue et al., 2012) (Figure 1.1). This sequence, which was the largest instrumentally recorded intraplate earthquake in history, yielded a total seismic moment of approximately 12–13 $\times$ 10^{21} and 2–3 $\times$ 10^{21} N m for the main shock and the aftershock, respectively (Duputel et al., 2012; Hill et al., 2015; Meng et al., 2012; Wei et al., 2013; Yue et al., 2012). Clear coseismic displacement was observed by the AGNeSS (Aceh GNSS Network for Sumatran Fault System) network (Ito et al., 2016) (Figure 1.1). Large oceanic intraplate earthquakes are extremely rare and provide valuable opportunities to investigate the rheological properties under the ocean.

Previous studies have explored the rheology of the oceanic asthenosphere layer after the 2012 Indian Ocean earthquake. Based on the postseismic gravity changes using the data obtained from the gravity recovery and climate experiment (GRACE), Han et al. (2015), assuming a 60-km oceanic lithosphere, indicated a biviscous flow with transient and steady-state viscosities of approximately 1 $\times$ 10^{18} and 1 $\times$ 10^{19} Pa s, respectively. Conversely, Hu et al. (2016) estimated Maxwell viscosity 2 $\times$ 10^{18} Pa s and 80-km asthenosphere thickness based on the mid-field (<500 km from the epicenter) and far-field (>500 km from the epicenter) GNSS (Global Navigation Satellite System) data that were obtained for the three years after the earthquake. Hu et al. (2016) assumed the oceanic lithosphere thickness

about 50-km. Meanwhile, Masuti et al. (2016), which assumed a stress-dependent viscosity (power-law viscosity), obtained a minimum water content of oceanic asthenosphere about 1600 H atoms per million Si atoms with a fixed 80-km oceanic lithosphere thickness. Although Masuti et al. (2016) objective are to estimate the water content of the oceanic asthenosphere; the effective viscosity can be derived. Based on the estimated water content, the maximum effective viscosity was 5×10^{17} Pa s.

These previous analyses obtained different values for the viscosity of the asthenosphere; this discrepancy may be caused due to the complex geometries and the different modeling assumptions. Additionally, Hu et al. (2016) apparently failed to explain the mid-field data where transient motion was observed, whereas Masuti et al. (2016) overestimated the horizontal component within a short observational period. These phenomena may indicate that the mid-field GNSS data are sensitive to different assumptions of the rheological structure.

Previous studies have also used different fixed oceanic lithospheric thicknesses to serve as prior assumptions. The oceanic lithospheric thicknesses range from 50 km in Hu et al. (2016) to 80 km in Masuti et al. (2016). However, there is no direct constraint on the oceanic lithospheric thickness beneath the Indian Ocean. Additionally, the different assumptions of oceanic lithospheric thickness indicate that the lithospheric thickness beneath the ocean remains poorly understood.

In this study, we analyze the mid-field data to obtain the oceanic lithospheric thickness and transient rheology beneath the Indian Ocean. We constructed a three-dimensional (3-D) spherical-earth finite-element model with a 3-D heterogeneous Earth-velocity structure based on seismic tomography and a

subducting slab due to the complex subduction region. We used two years of GNSS postseismic-motion data and focused on the mid-field stations in northern Sumatra to obtain a strong constraint on the viscosity, particularly the transient viscosity.

Postseismic deformation due to strike-slip earthquakes has been extensively modeled as viscoelastic relaxation (Freed et al., 2006; Hu et al., 2016), afterslip (Freed, 2007), and poroelastic rebound (Peltzer et al., 1998). We did not consider the poroelastic rebound due to the limited geodetic network and because the decay time was short (a few weeks); further, the rebound exhibited a relatively small amplitude. In this study, we combine the remaining two possible mechanisms (afterslip and viscoelastic relaxation).

1.2 Objectives

The primary objective of this study is to understand the rheological structure of the oceanic lithosphere and asthenosphere based on the postseismic deformation due to the 2012 Indian Ocean earthquake, which is inferred from the mid-field (less than 500 km from the epicenter) GNSS data. The primary mid-field data in northern Sumatra were obtained using the AGNeSS network (Ito et al., 2012), which was initiated by a collaboration of Japanese (Nagoya University, Kochi University, and Tohoku University) and Indonesian (Syiah Kuala University and the Bandung Insitute of Technology) universities.

We implement a 3-D finite element model based on the available heterogeneous structures of the rupture area and its surroundings to resolve and investigate the necessity of large temporal changes in the viscosity of the oceanic asthenosphere. Previous studies have modeled the postseismic deformation following the 2012 Indian

Ocean earthquake with different assumptions about the viscosity structure. However, all of these models failed to satisfactorily explain the mid-field GNSS data in both the horizontal and vertical components. Therefore, the primary objective of this study is to investigate an appropriate oceanic asthenospheric viscosity model.

Additionally, we intend to determine the oceanic lithospheric thickness based on the GNSS observations. In previous studies the oceanic lithospheric thicknesses were assumed a priori; however, this factor may exhibit a large trade-off with the oceanic asthenospheric viscosity reflected in the mid-field GNSS data. We construct a 3-D model and perform a grid search to systematically search for the best estimate of the oceanic lithospheric thickness and the oceanic asthenospheric viscosity. Therefore, the second objective of this study is to investigate the appropriate oceanic lithospheric thickness.

1.3 Dissertation Outline

This thesis comprises seven chapters. In Chapter 2, we review the tectonic background of the Indian Ocean region and the Sunda Trench and the historical earthquakes and crustal deformation in the vicinity of the Indian Ocean region.

In Chapter 3, we describe the GNSS data surrounding the Indian Ocean region that comprised GNSS data from the Andaman and Nicobar Islands, Sumatra (AGNeSS and SuGAr), and the International GNSS Service (IGS) site. We analyze the GNSS data in northern Sumatra to obtain a strong constraint of transient rheology. Additionally, this chapter explains the GNSS processing and modeling that was used to isolate the postseismic signal due to the 2012 Indian Ocean earthquake.

Chapter 4 describes the methodology used in this study. Because our strategy is to conduct 3-D finite element modeling due to the complex subduction zone, we describe the manner in which we construct the model geometry and further explored the space model to understand the sensitivity of each model parameter.

Chapter 5 presents the analysis of the coseismic deformation. There are several coseismic fault models based on previous studies. We collected the additional coseismic offset data and evaluated the coseismic fault model based on our 3-D finite element model. We used the preferred coseismic fault model in the postseismic deformation modeling based on this chapter.

Chapter 6 presents the analysis of the postseismic deformation. To obtain a clear definition, we describe the oceanic rheological model and the postseismic mechanism based on previous studies. We propose several models based on our analysis of previous studies. Further, we obtain the best-fit model as compared to the GNSS observation data.

In Chapter 7, the final chapter, we discuss and interpret the preferred rheological structure and its implications to study plate tectonics. We obtain fundamental findings, which we plan to publish in several research journals and proceedings or conferences. One of our studies has been published in the Journal of Asian Earth Science (October 2017), entitled “Transient rheology of oceanic asthenosphere following the 2012 Indian Ocean earthquake inferred from geodetic data.”. Another study has been published in the American Institute of Physics (AIP) conference proceedings (July 2018), entitled “Evaluation of the 2012 Indian Ocean coseismic fault model in 3-D heterogeneous structure based on vertical and horizontal GNSS observation.”

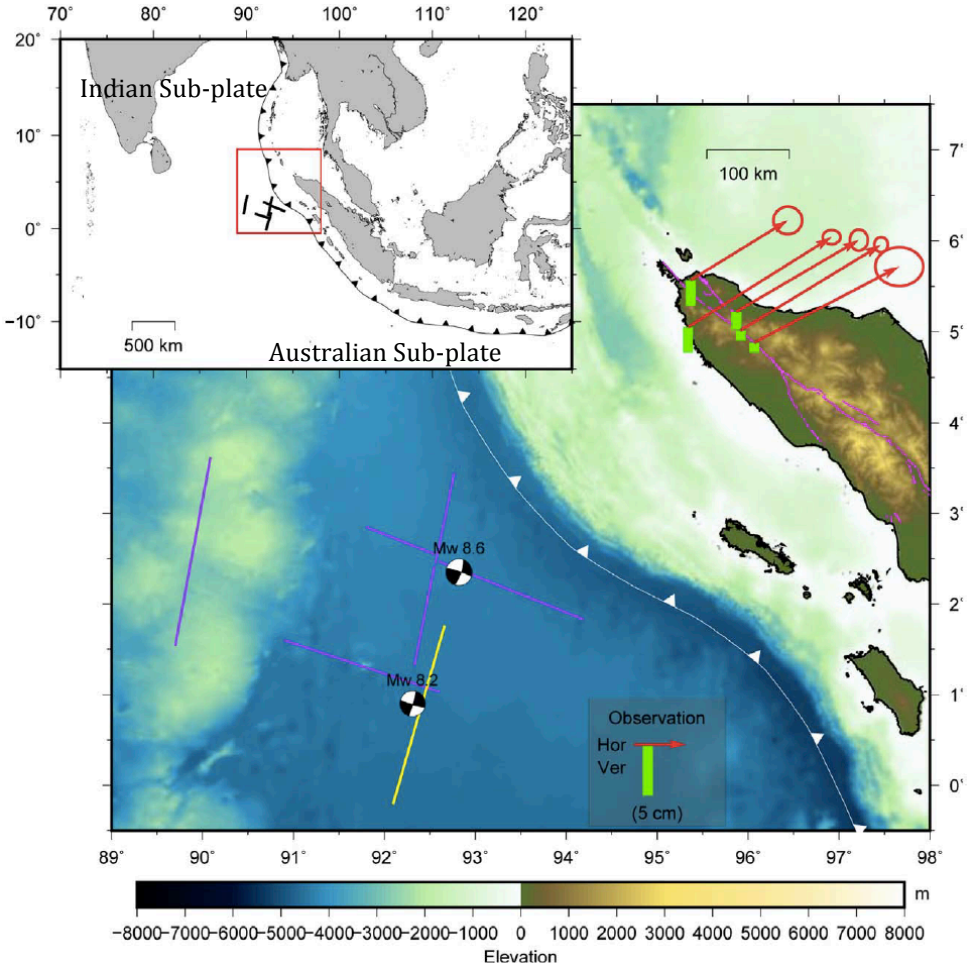

Figure 1.1. The general tectonic setting and coseismic displacement observed by the AGNeSS network due to the 2012 Indian Ocean earthquake. Red square shows the region of this study. White or black lines with triangles represent the Sunda Trench. Purple and yellow lines indicate fault surface traces due to the Mw 8.6 mainshock based on Hill et al. (2015) and the largest (Mw 8.2) aftershock based on Wei et al. (2013), respectively. Magenta lines on the Sumatra Island indicate the Great Sumatran Fault

2 Tectonic Background of the Indian Ocean

To model and interpret crustal deformation, we need to first understand the structures and tectonic settings of the region. In this chapter, we will outline the tectonic background of the Indian Ocean. First, we introduce the model of a diffuse boundary, which will be used to explain the deformation features between the Indian sub-plate and the Australian sub-plate. Second, we describe the Indian and Australian sub-plates as a complex and unique major tectonic plate boundary. Third, we elaborate on the historical seismicity, plate age and plate motion based on previous observations of the 2012 Indian Ocean rupture area.

2.1 The Indian Ocean as a Diffuse Boundary

Plate tectonics is a unifying theory that describes the kinematics and surface tectonic features of the earth. One of the major types of tectonic features that we can see from the surface is the three classes of plate boundaries. Boundaries, where one plate is being subducted beneath another, are known as trenches. Boundaries, where different plates are diverging, are known as ridges, and boundaries, where two plates are moving side by side are known as transform faults. The origin of these boundaries was not understood well until the theory of plate tectonics was proposed.

Plate tectonics, which is a culmination of the seafloor spreading hypothesis, was first quantitatively proposed as six rigid plates in motion separated by narrow boundaries that are moveable relative to each other (Le Pichon, 1968). This built on the preceding hypothesis of rigid and angular rotation of plates (McKenzie and Parker, 1967; Morgan, 1968; Wilson, 1965). Gordon (1998) summarized that the key assumption of plate tectonics is that the plates are rigid and form a narrow boundary. However, in many other oceanic and continental deformation zones, this key assumption has been inconsistent with observed plate motion and seismicity. This lead to the development of the concept of other types of the plate that are non-rigid and have a wide (diffuse) boundary (Gordon and Stein, 1992; Gordon, 1998; Royer and Gordon, 1997; Wiens et al., 1985).

When Gordon (1998) used the term "narrow boundaries," he was describing boundaries with a deformation zone a few kilometers in width. Types of narrow plate boundaries include mid-oceanic ridges, subduction/collision zones, and oceanic transform faults. Rigid plates separated by narrow boundaries cover 85% of the Earth's surface (Gordon, 1998). Conversely, there are wide boundaries that accommodate deformation over hundreds or thousands of kilometers. These wide

boundaries such as the Indian Ocean region, where the 2012 Indian Ocean earthquake occurred, cover 15% of the Earth's surface (Gordon, 1998).

2.2 Indian and Australian Sub-Plates

The epicenter of the 2012 Indian Ocean earthquake is situated between the Indian and Australian sub-plates (Figure 1.1). Before 1985, many scientists considered the Indo–Australian plate to be one single large plate (Wiens et al., 1985; Gordon and Stein, 1992) (Figure 2.1a). However, this single Indo–Australian plate has perplexing tectonic regions. The southeastern Indo–Australian plate is subducting beneath the southeastern part of the Eurasian plate along the Sunda trench, while the northwestern Indo–Australian plate is colliding with the central part of the Eurasian plate along the Himalayan arc (DeMets et al., 1994; Hamilton, 1979; Jade et al., 2017; Simons et al., 2007) (Figure 2.1a). There is also a hotspot track, the north–south trending Ninetyeast Ridge (90ER), that separates the Indian Ocean into the Central Indian Basin and the Wharton Basin (Frey et al., 2011; Nobre Silva et al., 2013). Each has distinct tectonic features; there is north–south compression in the Central Indian Basin due to the India-Eurasia collision, and northwest–southeast compression with northeast-southwest extension in the Wharton Basin due to slab pull forces in the Indo–Australia–Eurasia plate boundary along Sumatra (Andrade and Rajendran, 2014; Cloetingh and Wortel, 1986; Delescluse et al., 2012; Sager et al., 2013).

DeMets et al. (1988) suggested a different model for Indian Ocean tectonics that describes a diffuse boundary between the Indian and Australian sub-plates (Figure 2.1b). Adding to this, Royer and Gordon (1997) redefined the deformation zone that is surrounded by India, Australia (AUS), and Capricorn (CAP) sub-plates (Figure 2.1c). Although the exact location of the boundary between the Indian and Australian sub-

plates within the Indian Ocean is debatable (Gordon, 1998; Petroy and Wiens, 1989; Royer and Gordon, 1997; Wiens et al., 1985), the 2012 Indian Ocean earthquake occurred within the Indian Ocean deforming zone. New fault plains that are not aligned with older structures, inferred from this earthquake, suggest that there is a transition from a diffuse (wide) boundary to a localized (narrow) boundary between the Indian and Australian sub-plates (Hill et al. 2015; Wei et al. 2013).

2.3 Historical Seismicity, Plate Age and Plate Motion of Indian Ocean

2.3.1 Historical Seismicity

The Indian Ocean region has the most seismically active intraplate oceanic lithosphere in the world (Andrade and Rajendran, 2014; Bergman and Solomon, 1985; Delescluse and Chamot-Rooke, 2007; Petroy and Wiens, 1989; Sasajima and Ito, 2016; Wiens et al., 1985, Kreemer et al., 2014). The presence of active deformation has been confirmed by the large earthquakes that occur in the region, such as the June 2000 (Mw 7.9) Enggano earthquake, the June 2000 (Mw 7.8) Cocos Island earthquake (Abercrombie, 2003; Robinson et al., 2001), the July 2003 (Mw 7.6) mid-Indian Ocean earthquake (Antolik et al., 2006), the June 2010 (Mw 7.5) Nicobar earthquakes (Rajendran et al., 2011), the April 2012 (Mw 8.6 & Mw 8.2) Indian Ocean earthquake (Delescluse et al., 2012; Duputel et al., 2012; Meng et al., 2012), and the March 2016 (Mw 7.8) northwestern Wharton Basin earthquake (Lay et al., 2016). There were numerous historical (pre-2000) earthquakes of note (Mw >7) that have been compiled by several recent studies (Aderhold and Abercrombie, 2016; Andrade and Rajendran, 2014; Delescluse and Chamot-Rooke, 2007). The discovery of a conjugate system of faults, which accommodates present-day intraplate

deformation in the Wharton Basin, is also evidence of active deformation in the Indian Ocean regions (Singh et al., 2017).

2.3.2 Plate Age

The location of the 2012 Indian Ocean earthquake is on a plate with an age of 40–60 Myrs (Figure 2.2). Characteristics of the oceanic lithosphere, such as the elastic thickness and the seismogenic depth, reflect the plate age. In the Indian Ocean region, the centroid locations of frequent historical earthquakes, including the 2012 Indian Ocean earthquake, are found throughout the seismogenic mantle, constrained by the 600^{o}C isotherm corresponding to the estimated oceanic lithospheric age (Aderhold and Abercrombie, 2016; McKenzie et al., 2005). In a later chapter, we will discuss our optimum model in comparison with the plate age calculated in previous studies.

2.3.3 Plate Motion

Plate motion in the Indian Ocean region varies due to the collision of the Indian sub-plate with the Eurasian plate far to the north along the Himalayan arc. The Australian sub-plate is also exerting slab pull forces on the Eurasian plate along the Sunda trench (Figure 2.3). The west side of the Indian sub-plate is colliding with the east side of Himalayan arc at a rate of 37–44 mm/yr (Jade et al., 2017; Paul et al., 2001). On the other side of the Indian Ocean, the oceanic lithosphere near the Andaman Islands is moving at a rate of 39 mm/yr. Along the Sunda trench at western Sumatra, relative plate motion is 47–52 mm/yr. The relative plate motion along the Sunda trench at southern Java is 63 mm/yr (McCaffrey, 2009; Prawirodirdjo et al.,

2000; Subarya et al., 2006). In the discussion chapter of this thesis, we will discuss our optimum model and compare it to the average regional plate motion.

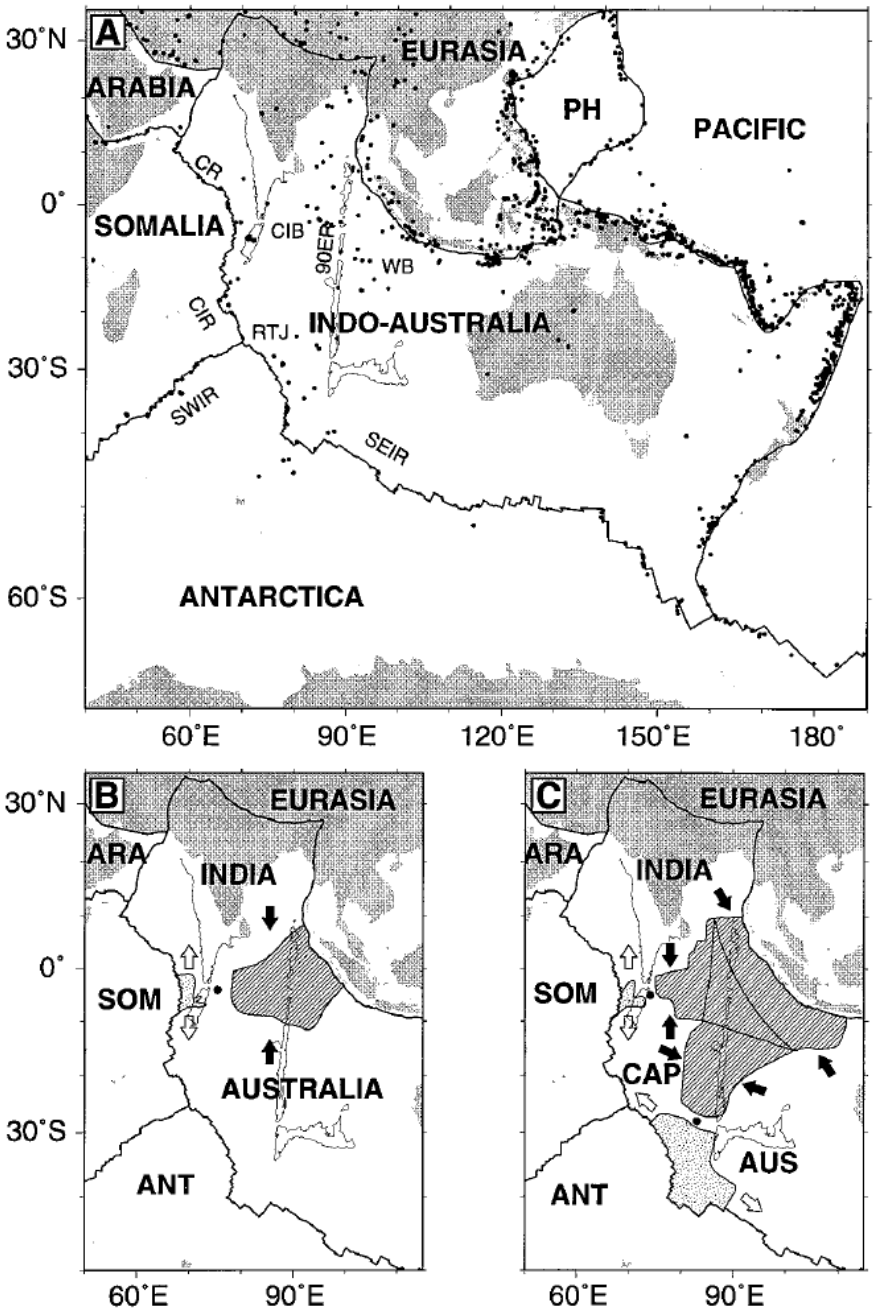

Figure 2.1 (A) Traditional Indo–Australian plate boundaries shown as a single plate with background seismicity (mb > 5.5) shown by small solid circles. Wharton Basin (WB), Central Indian Basin (CIB), Southeast Indian Ridge (SEIR), Philippine Sea Plate (PH), Ninetyeast Ridge (90ER), Southwest Indian Ridge (SWIR), Rodrigue Triple Junction (RTJ), Carlsberg Ridge (CR), and Central Indian Ridge (CIR). (B) Diffuset plate boundary model from DeMets et al., (1988). (C) Plate geometry proposed in Royer and Gordon (1997). Capricorn Plate (CAP), redefined Australian plate (AUS). Stipples denote a new diffuse boundary. (Same as Figure 1 of Royer and Gordon (1997))

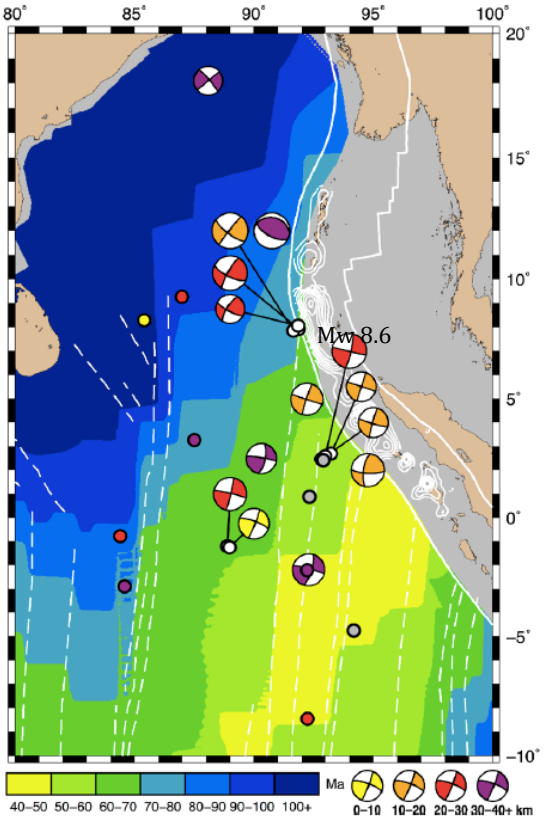

Figure 2.2 Solid white lines are plate boundaries (Bird, 2003)**. White dashed lines are fracture zones** (Matthews et al., 2011)**. White contours are 2 m slip of the 2004 Sumatra–Andaman earthquake** (Chlieh et al., 2007) **and the 2005 Nias earthquake** (Konca et al., 2007)**. Lithospheric age of the regions is taken from Muller et al. (2008). Color of double–couple moment tensors denotes the centroid depth. (Similar to Figure 1b of Aderhold and Abercrombie (2016))**

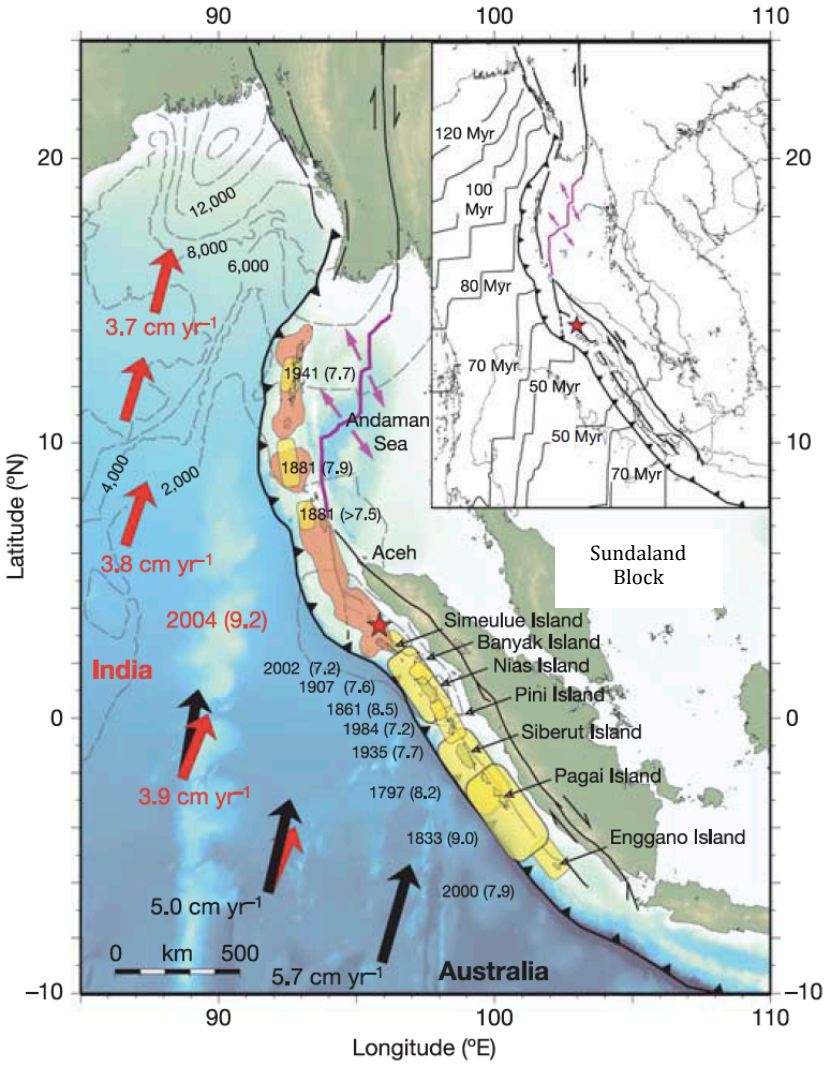

Figure 2.3 Plate velocities of Australia (black arrows) and India (red arrows) relative to Sundaland Block were computed from a regional kinematic model. The shaded yellow regions are estimated historical ruptures along the subduction region from 1797 to 2004. The shaded orange regions are slip patches from the 2004 Sumatra–Andaman earthquake. The inset shows the plate age. (Similar to Figure 1 of Subarya et al. (2006))

3 Global Navigation Satellite System (GNSS) Observation Data

Space geodesy is a multi-purpose concept and tool to observe various phenomena in a wide field of Earth science. Global Navigation Satellite System (GNSS) is one of the enormous space geodesy techniques that made a great progress in the last decades (Kreemer et al., 2014; Rummel, 2010). The number of GNSS stations around the world increase significantly and the precision of the measurement become as tight as the millimeter level (Dach et al., 2007).

In the last decade, discussion on the ground deformation due to an earthquake cycle such as interseismic phase (e.g. Hanifa et al., 2014; Loveless & Meade, 2016), coseismic phase (Hamling et al., 2017; Hill et al., 2015; Ito et al., 2011; Rhie et al., 2007) and postseismic phase (Freed et al., 2017; Gunawan et al., 2014; Moore et al., 2017) based on GNSS data has been more intense than ever.

Nowadays, the GNSS data can capture precise time-dependent signal including the effect from heterogeneities of the earth geometrically and parametrically (Freed et al., 2017; Shibazaki et al., 2016). The 2012 Indian Ocean earthquake also

provides a rare opportunity to investigate heterogeneity and complexity of the Earth's structure. However, since the earthquake occurred in the middle of the ocean and all available GNSS stations surrounding the rupture are located on land, the GNSS stations are very far from the source. Also, the postseismic signal would be affected by complex subduction region. The large distance between the rupture and GNSS stations and the effect of complex subduction regions are challenging but also an opportunity for rheology studies. In addition, there is a chance to test the reliability of the complex three-dimensional numerical model and confirm which data are sensitive to the complex structure of the Earth.

Here, in Chapter 3, we used GNSS data to model postseismic deformation due to the 2012 Indian Ocean earthquake in order to obtain a rheology picture under the Indian Ocean. Following sub-chapters will describe issues related to GNSS network in these regions. First, we describe the GNSS network available in these regions based on previous studies. Second, we showed the importance of the mid-field GNSS data since the last studies failed to explain them (Hu et al. 2016). Third, we elaborate on the GNSS data processing to obtain the surface displacement. Fourth, we showed the original observation data and the characteristics of the time series. Fifth, we did time series de-trending using analytical function fitting to isolate postseismic signal due to the 2012 Indian Ocean earthquake. Sixth, we summarized the coseismic and two-years postseismic displacement of our GNSS data.

3.1 GNSS Observation Around The Indian Ocean

There are several GNSS networks surrounding the Indian Ocean that capture clear coseismic offset signals due to the 2012 Indian Ocean earthquake. Although most of the GNSS sites are on the continent around hundreds of km away from the source, the great sequence of the 2012 Indian Ocean earthquake still made the GNSS move during the coseismic period in the Sumatra, Andaman-Nicobar Islands, and several IGS sites (Yadav et al., 2013, Feng et al., 2015, Ito et al., 2016, Gunawan et al., 2016).

The Andaman-Nicobar Islands observed southward coseismic offsets while IGS sites in the southern rupture area such as COCO and XMIS sites moved northward (Yadav et al., 2013). In Sumatra, there are SuGAr (Figure 3.1) and AGNeSS (Figure 3.2) networks that record significant coseismic changes with horizontal landward motion (Ito et al., 2016, Feng et al., 2015, Hill et al., 2015, Gunawan et al., 2016).

Although the coseismic offset was very clear in the most of the network with a radius of 2000 km from the source region, only a part of stations recorded clear postseismic signal. All AGNeSS sites recorded significant postseismic signal for horizontal landward motion (Ito et al., 2016) (Figure 3.2). Also, a few SuGAr sites observed clear postseismic landward motion (Feng et al., 2015). However, clear postseismic uplift only saw within 500 km from the earthquake source region (Feng et al., 2015). One of the deformation feature observed in the GNSS data is the vertical component of the SuGAr and AGNeSS network recorded coseismic subsidence but postseismic uplift. We will describe the detailed GNSS motion in the next sub-chapter.

3.2 Importance of GNSS data in the Northern Sumatra

GNSS dataset with different source distances was used to analyze postseismic deformation. In the case of the 1992 Landers, postseismic deformation based on near-field (within 10-20 km) was explained by a combination of poroelastic rebound and lower crustal flow or afterslip but failed to explain far-field deformation (Freed and Bürgmann, 2004; Freed et al., 2007). In the case of the 2002 Denali, the near-field data required localized and shallow lower crust viscoelastic relaxation while the far-field data required broad and deep upper mantle viscoelastic relaxation (Biggs et al., 2009; Freed, et al., 2006; Johnson et al., 2009). In the case of the 2004 Sumatra-Andaman megathrust earthquake, the near-field GNSS data in northern Sumatra were explained by dominant afterslip and short-term viscoelastic relaxation while in the far field such as in the Thailand region network could be explained by only long-term viscoelastic relaxation process (Gunawan et al., 2014; Hu and Wang, 2012a; Panet et al., 2010; Paul et al., 2007; Paul et al., 2012). Also, a dataset with different source distances could reveal the complexity of postseismic processes caused by the 2011 Tohoku-oki earthquake (Freed et al., 2017; Shibazaki et al., 2016; Sun et al., 2014). One of our study purposes is to investigate the rheology structure under the oceanic lithosphere. Therefore, the rapid change of the postseismic transient signal is essential to strongly constrain the rheology structure.

GNSS data in the northern Sumatra exhibited clear postseismic transients due to the 2012 Indian Ocean earthquake. However, the SuGAr network in the far-field shows a very small postseismic displacement, which is difficult to detect in a shorter period (< 2 years) (Feng et al., 2015). Thus, we need a longer time-series data to see if there is a longer relaxation process due to the 2012 Indian Ocean earthquake.

Previous studies have modeled the postseismic deformation in this region based on different spatial and temporal scales of GNSS data. Hu et al. (2016) used 3-years displacement of mid-field and far-field GNSS data. Mid-field station consists of two stations from AGNeSS (ACEH and TANG stations) and far-field stations covered most SuGAr networks. The model could explain the general character of the postseismic displacement such as horizontal landward motion and uplift. However, their model failed to explain the azimuth of the postseismic displacement in the mid-field and difficult to explain the far-field data. Masuti et al. (2016) used 1-year mid-field of SuGAr networks. The model succeeded to explain the GNSS time series in the fore-arc but overestimate those in the northern Sumatra (Masuti et al., 2016) (The complete description will be found on Chapter 6). In this study, we analyzed a longer mid-field data to investigate transient rheology to explain the postseismic signal.

We utilized the postseismic motion based on daily solutions from the Aceh GNSS Network for the Sumatran fault system (AGNeSS) and the Sumatran GPS Array (SuGAr). This network is very near to the 2012 Indian Ocean earthquake rupture area and recorded both horizontal and vertical postseismic transient clearly.

3.2.1 The AGNeSS Network

The Aceh GNSS Network for Sumatran fault System (AGNeSS) was deployed by Nagoya University, Kochi University, Tohoku University, Bandung Institute of Technology, and Syiah Kuala University, during a couple of months after the 2004 Sumatra–Andaman Earthquake (Ito et al., 2012). This network has recorded more than one decades of deformation in northern Sumatra. It recorded creep motion along the northern part of the Great Sumatran Fault (Ito et al., 2012), postseismic decay signal due to the 2004 Sumatra Andaman earthquake (Gunawan et al., 2014), co- and

post-seismic signal due to the 2012 Indian Ocean earthquake, coseismic offset due to the two 2013 Mw 6.1 earthquakes (Ito et al., 2016). The AGNeSS consists of continuous permanent and yearly campaign GNSS sites. In this study, we restrict our dataset to the continuous GNSS sites in order to capture the transitional features just after the earthquake rupture. Figure 3.3 shows the AGNeSS site locations used in this study. Details of GNSS stations are described in Table 3.1.

3.2.2 The SuGar Network

The Earth Observatory of Singapore (EOS) and Indonesian Institute of Sciences (LIPI) operate the Sumatran GPS Array network (SuGAr). A few SuGAr sites were deployed before the 2004 Sumatra-Andaman earthquake but mostly after that. The daily Receiver Independent Exchange (RINEX) data of SuGAr can be obtained from the Scripps Orbit and Permanent Array Center website (http://garner.ucsd.edu) and ftp://eos.ntu.edu.sg/SugarData with a latency of 3 months (Feng et al. 2015). Different from the AGNeSS network that concentrated in the Aceh province, the SuGar network extends from the northern Sumatra to the south along the fore arc of the western part of Sumatra Island (Figure 3.3). Those SuGAr site locations are complementary to the AGNeSS sites to have a wide spatial coverage in the 2012 Indian Ocean postseismic modeling. A detailed description of the SuGAr sites is on the Table 3.2

3.3 GNSS Data Processing

We utilized 2 years of the postseismic signal obtained with GNSS to constraint rheology of the oceanic asthenosphere. The total 9 permanent continuous GNSS sites

in the mid-field (<500 km) are used to constrain to transient viscosity. To obtain the transient surface displacement, we processed each RINEX format dataset to yield the daily coordinate time series of each GNSS site. The data were processed with the permanent International GNSS Service (IGS) sites as a realization in the International Terrestrial Reference Frame 2008 (ITRF2008) (Altamimi et al., 2011). The IGS sites that we used for our processing are BAKO (West Java), XMIS (Christmas Island), COCO (Cocos Island), NTUS (Singapore), HYDE (India), IISC (India), DGAR (British Indian Ocean Territory), KUNM (Mainland China) and CUSV (Thailand) (Figure 3.4).

We attempt to estimate precise daily positions using final product and model parameter from Center for Orbit Determination in Europe (CODE) (Dach et al. 2007). We prepared precise satellites orbits, earth rotation parameters, ionosphere model and differential code biases for satellites and receivers based on the downloaded file from the University of Bern (ftp://ftp.unibe.ch/aiub/). Corrections of ocean tide were done based on the ocean tide model coefficients calculated using Finite Element Solutions 2004 (FES2004) (Lyard et al. 2006). I use BERNESE 5.0 software (Dach et al., 2007) for our analysis. I first obtained an initial coordinate using PPP (Point Precise Positioning) strategy followed by a double difference of baseline based method to obtain integrated daily solutions with a millimeter-level accuracy.

In order to make the time series represent the actual postseismic deformation, the resulting daily positions were transformed to the Sundaland block reference frame. The Sundaland block is considered to be a rigid block moving relative to the Eurasian plate (Altamimi et al., 2012; Simons et al., 2007). Altamimi et al. (2012) provided transformation parameters from ITRF2008 to the Sundaland block reference frame. However, the reported ITRF2008-Sundaland transformation has a relatively large

uncertainty (Altamimi et al. 2012) because it was derived from only two stations. Instead of applying the direct transformation, we used the transformation parameter reported by Simons et al. (2007) with respect to the ITRF2000. First, we transform the coordinates from ITRF2008 to ITRF2000 (Altamimi et al., 2007) using the following equation

$$\begin{pmatrix} X \\ Y \\ Z \end{pmatrix}_{i00} = \begin{pmatrix} x \\ y \\ z \end{pmatrix}_{i08} + \begin{pmatrix} T_x \\ T_y \\ T_z \end{pmatrix} + \begin{pmatrix} D & -R_z & R_y \\ R_z & D & -R_x \\ -R_y & R_x & D \end{pmatrix} \begin{pmatrix} x \\ y \\ z \end{pmatrix}_{i08} \quad (1)$$

where x, y, and z are the coordinates/velocity in the ITRF2008 frame while X, Y, and Z are the coordinates/velocity in the ITRF2000 frame. Other parameters are corresponding to the transformation parameters in Table 3.3.

Once we get the time series transformed to the ITRF2000, we calculate the velocity at a specific location due to Sundaland block motion based on Simon et al.'s (2007) parameters using the following equation

$$v = \bar{\omega} R \sin a \quad (2)$$

$$\beta = 90 + \sin^{-1}\left(\frac{\cos\lambda_P \sin(\phi_P - \phi_X)}{\sin a}\right) \quad (3)$$

where

$$a = \cos^{-1}[\sin\lambda_X \sin\lambda_P + \cos\lambda_X \cos\lambda_P \cos(\phi_P - \phi_X)] \quad (4)$$

v and β are magnitude and azimuth (with respect to north N) at GNSS site (point X) relative to Sundaland block (P), respectively. λ and ϕ are latitude and longitude while

R and $\overline{\omega}$ are the radius of the Earth and angular velocity of rotation pole. Simons et al. (2007) estimated the pole position and the angular velocity of the Sundaland block from 28 GNSS site. The estimated parameter λ_P, ϕ_P, and $\overline{\omega}$ are 49.0^{o}N, -94.2^{o}E, and 0.336^o/Myr, respectively. Based on the calculated velocity at each GNSS site due to Sundaland block motion, we transform the time series into the Sundaland block reference frame. All GNSS motion shown or stated hereinafter is processed to Sundaland block.

3.4 Time Evolution of Crustal Deformation at GNSS Site

We plotted the GNSS time series in Figure 3.4 for North-South, East-West, and Up-Down components, respectively. The 2004 Sumatra-Andaman earthquake affected all of the sites. We can see the postseismic movements at ACEH and UMLH sites have been decaying since the M9 class megathrust earthquake. Although time evolution of the vertical component looks more linear than horizontal GNSS components, both of them recorded the postseismic deformation following the 2004 Sumatra-Andaman earthquake well as has been reported by several studies (e.g. Gunawan et al. 2014, Hu & Wang, 2012a). Most of the SuGAr sites at the fore arc may also be affected with the postseismic deformation due to the 2005 Nias earthquake (Feng et al. 2015). We showed the coseismic slip distribution of the 2004 Sumatra-Andaman and the 2005 Nias earthquakes in Figure 2.2 and Figure 2.3.

On April 2012, the time series of GNSS sites showed clear horizontal and vertical offsets due to the 2012 Indian Ocean earthquake (Figure 3.5, 3.6 and 3.7). Most of the sites were moving toward northeast coseismically. Meanwhile, we observed slightly coseismic subsidence in the fore arc (LEWK, BSIM, BNON) but difficult to decide in the mainland (ACEH, UMLH, UGDN, TANG, MANE) of the

Northern Sumatra. Although coseismic subsidence is not clear in the mainland, slower vertical rates slightly exhibited than those prior to the 2012 Indian Ocean earthquake on UMLH and ACEH sites.

3.5 Modeling pre-earthquake trend based on GNSS time series

As we mentioned in the previous section, all site in the northern Sumatra continued to record postseismic deformation after the 2004 Sumatra–Andaman earthquake. Also, the SuGAr sites in the fore arc may be affected by postseismic deformation due to the 2005 Nias earthquake. Additionally, these GNSS data also record both tectonic long-term motion and various seasonal motions. In order to extract the postseismic deformation due to the 2012 Indian Ocean earthquake, other signals should be removed using model.

We intend to de-trend the GNSS daily solutions by constructing a model of pre-earthquake deformation. We assume that tectonic long-term motion can be modeled as a linear trend, and the annual and semi-annual seasonal effects can be represented by sinusoidal functions (Nikolaidis and Bock, 2002). Meanwhile, the postseismic deformation can be described by a combination of logarithmic and exponential functions, with τ_{as} and τ_{ve} representing afterslip and viscoelastic decay time, respectively (Kreemer et al., 2006; Marone et al., 1991; Tobita, 2016). The temporal change of daily coordinate time series can be modeled as follows

$$u(t) = At + B\ln\left(1 + {}^{t}/_{\tau_{as}}\right) + C\left(1 - e^{-\left({}^{t}/_{\tau_{ve}}\right)}\right) + D\sin(2\pi t) + E\cos(2\pi t) + F\sin(4\pi t) + G\cos(4\pi t) \quad (5)$$

where *t* is time (years). We modeled other signals of pre-earthquake deformation by equation (5). We estimate the afterslip and viscoelastic decay time independently for each site. However, for SuGAr sites, we exclude the linear trend function and replace it with the estimated linear trend reported from Bradley et al. (2016) which is consider the effect of the diffuse deforming zone of the Indian Ocean lithosphere and consider more longer observation period from 2005. They reported the linear trend of SuGAr sites with a more rigorous approach and longer time series since the GNSS site was deployed. Since the linear trends are velocities based on ITRF2008, we transform the velocities to ITRF2000 using equation (1) and parameters in Table 3.3. Then, we subtracted the pre-earthquake model result from the original observation data (Figure 3.5). Finally, we obtained the actual postseismic deformation associated with the 2012 Indian Ocean earthquake (Figure 3.6).

3.6 Displacement and error estimation

For the displacement, we model the de-trended time series with equation (5) in which the decay time estimated by grid search. We used matrix covariance to represent the error propagation from data covariance C_u to parameter covariance C_s. Given the linear model in matrix form

$$u = Gs \tag{6}$$

with data covariance C_u, a least squares solution is given by

$$\hat{s} = (G^T C_u^{-1} G)^{-1} G^T C_u^{-1} u \tag{7}$$

the covariance of the estimated parameters C_s is given by

$$C_s = (G^T C_u^{-1} G)^{-1} \tag{8}$$

The detailed coseismic and postseismic displacements are shown in Table 3.4 and Table 3.5, respectively. Vector displacements of each GNSS sites due to the coseismic and postseismic are shown in Figure 3.8.

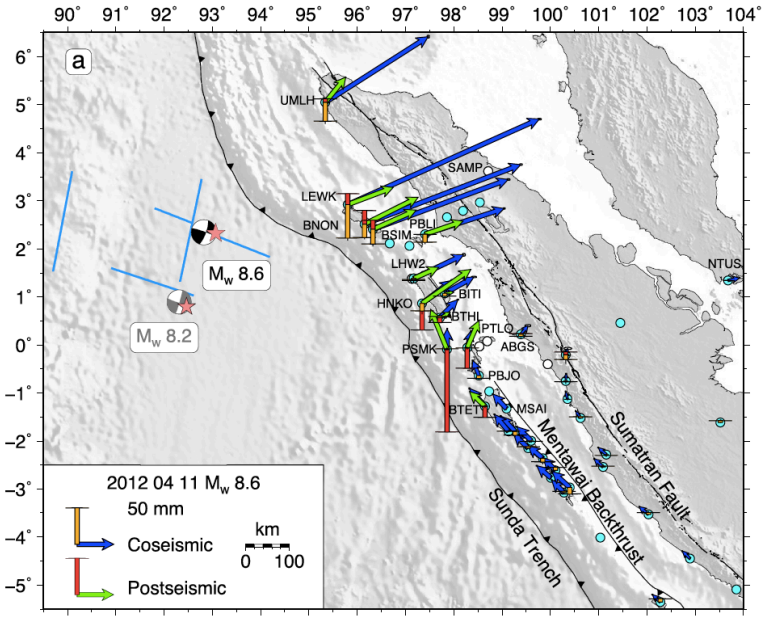

Figure 3.1 SuGAr Network recorded coseismic and postseismic displacement. Blue arrow and orange bar denotes horizontal and vertical component of coseismic deformation. Green arrow and red bar denotes horizontal and vertical component of postseismic deformation. (Same as Figure 10a of Feng et al. (2015))

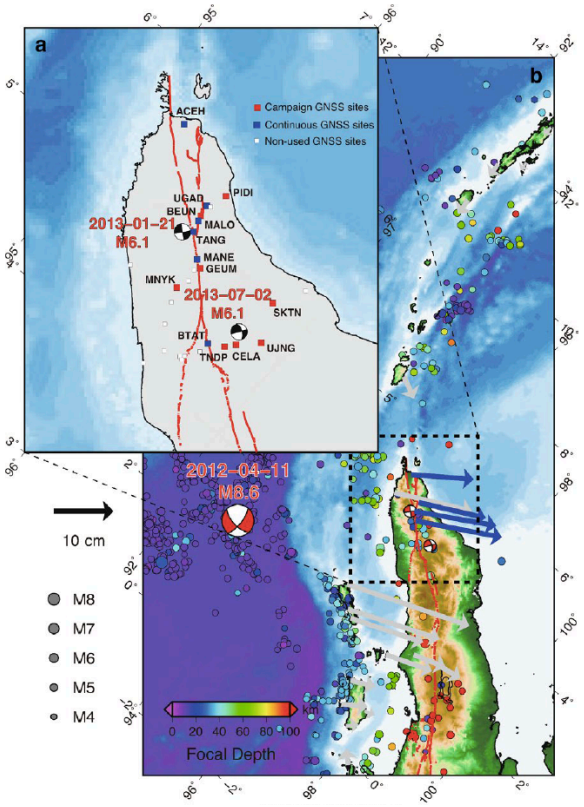

Figure 3.2 (a) AGNeSS network for both campaign and continuous GNSS sites. (b) Blue and gray denotes coseismic offset due to the 2012 Indian Ocean earthquake from AGNeSS and Others (SuGAr and The Andaman-Nicobar) network, respectively. (Same as Figure 1 of Ito et al. (2016))

Table 3.1 Continuous AGNeSS site that used in this study

No.	Site Name	Longitude (^{o} E)	Latitude (^{o} N)	Pre-Earthquake Period (yr)	Postseismic Period (yr)	Distance from Epicenter (Km)
1	ACEH	95.368398	5.569303	2005.17-2012.27	2012.27-2014.3	466.31
2	UGDN	95.872015	5.223171	2008.14-2012.27	2012.27-2014.15	481.10
3	MANE	96.067718	4.881502	2008.61-2012.27	2012.27-2013.5	476.13
4	TANG	95.917671	5.017032	2007.89-2012.27	2012.27-2014.3	471.14

Table 3.2 Continuous SuGAr site that used in this study

No.	Site Name	Longitude (^{o} E)	Latitude (^{o} N)	Pre-Earthquake Period (yr)	Postseismic Period (yr)	Distance from Epicenter (Km)
1	UMLH	95.338986	5.053118	2005.11-2012.27	2012.27-2014.3	423.81
2	LEWK	95.804056	2.923590	2011.00-2012.27	2012.27-2014.3	369.75
3	BNON	96.150824	2.520807	2011.00-2012.27	2012.27-2014.23	405.24
4	BSIM	96.326162	2.409248	2011.00-2012.27	2012.27-2014.1	424.82
5	PBLI	97.405277	2.308522	2011.00-2012.27	2012.27-2014.3	544.90

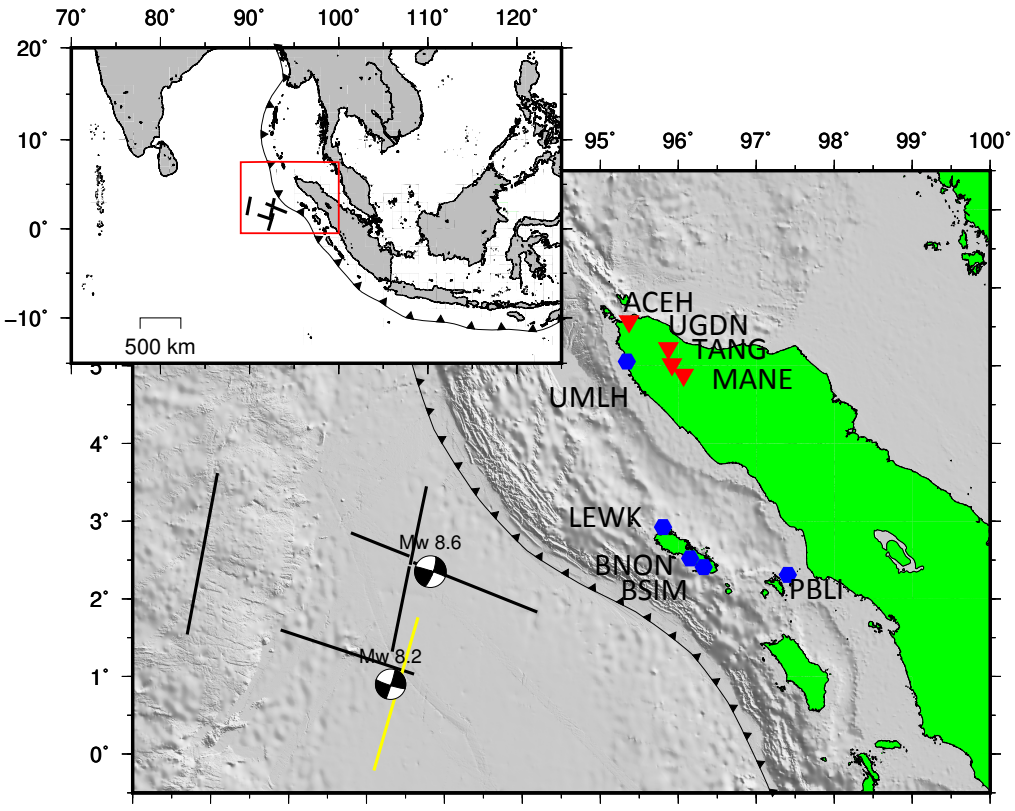

Figure 3.3 Site locations that used in this study. Black and yellow lines indicates finite fault model due to the Mw 8.6 and Mw 8.2 2012 Indian Ocean earthquake (Hill et al., 2015; Wei et al., 2013). Red inverted triangle and blue diamond denotes AGNeSS and SuGAr sites, respectively.

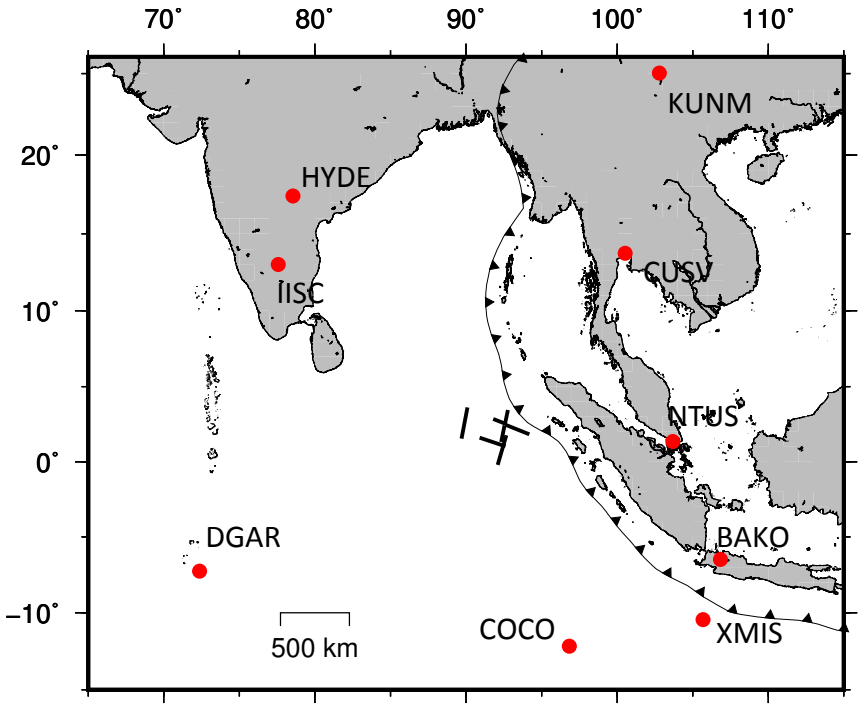

Figure 3.4 IGS site that used in the GNSS data processing. Thin black line with triangle is plate boundary. Thick black lines indicate the fault trace of the 2012 Indian Ocean earthquake.

Table 3.3 Transformation parameters from ITRF2008 to ITRF2000

Parameter	Tx (mm) (mm/yr)	Ty (mm) (mm/yr)	Tz (mm) (mm/yr)	D (pbb) (ppb/yr)	Rx (0.001") (0.001"/yr)	Ry (0.001") (0.001"/yr)	Rz (0.001") (0.001"/yr)
Solution	-1.9 0.1	-1.7 0.1	-10.5 -1.8	1.34 0.08	0 0	0 0	0 0

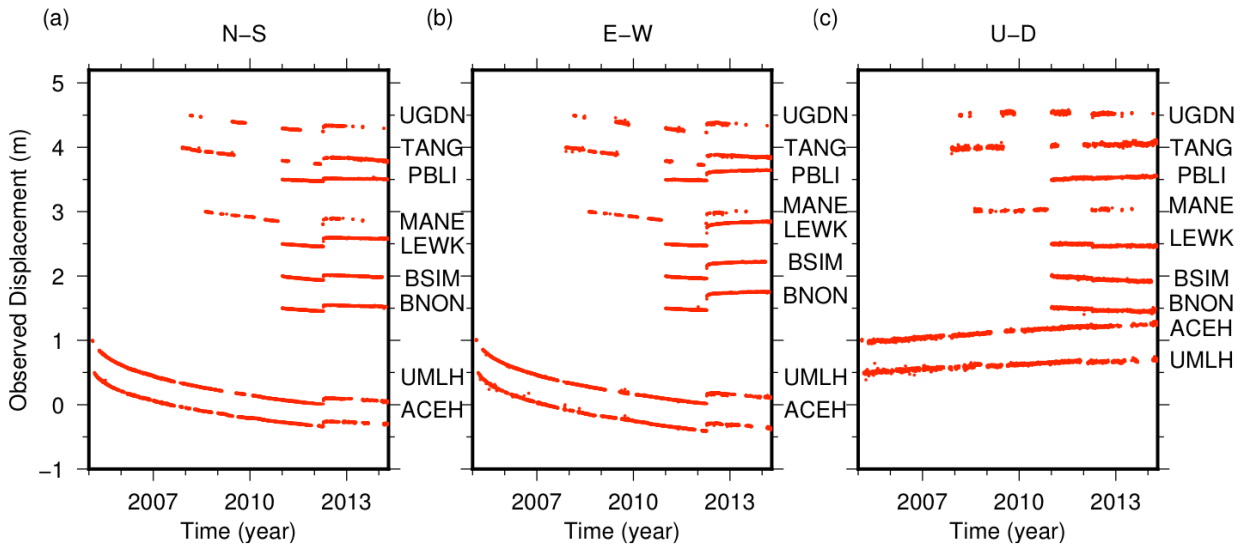

Figure 3.5 Original observation with Sundablock reference frame for all site that used in this study.

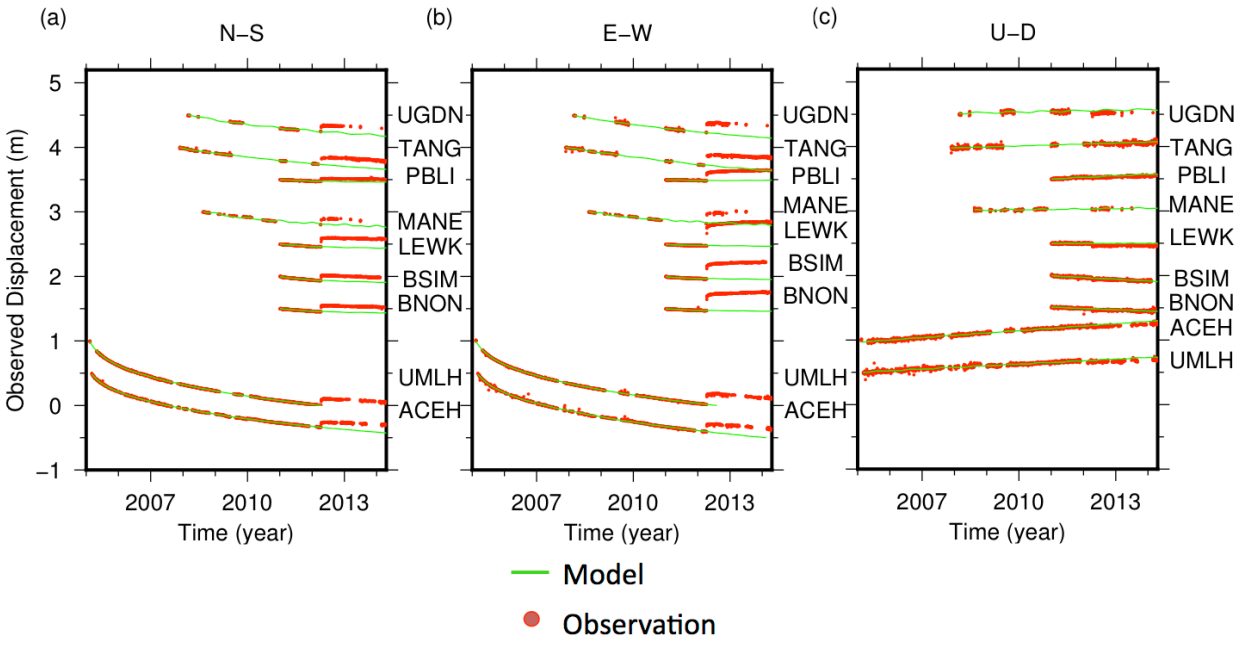

Figure 3.6 Model fitting to the time series before the 2012 Indian Ocean earthquake. Green line and red dot represents the model and observation data, respectively.

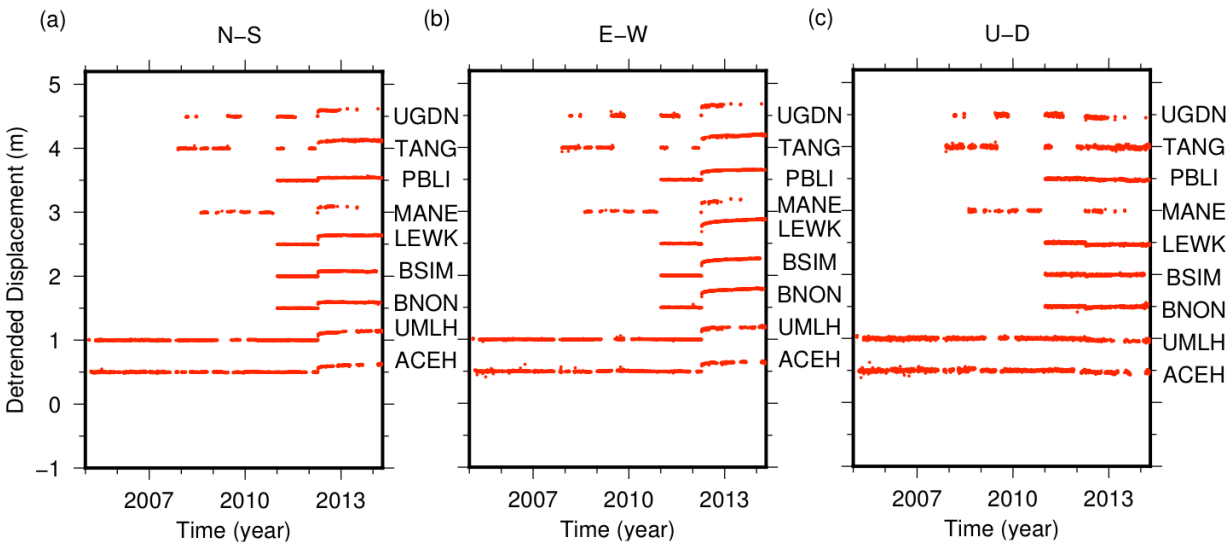

Figure 3.7 The de-trended time series using equation (5)

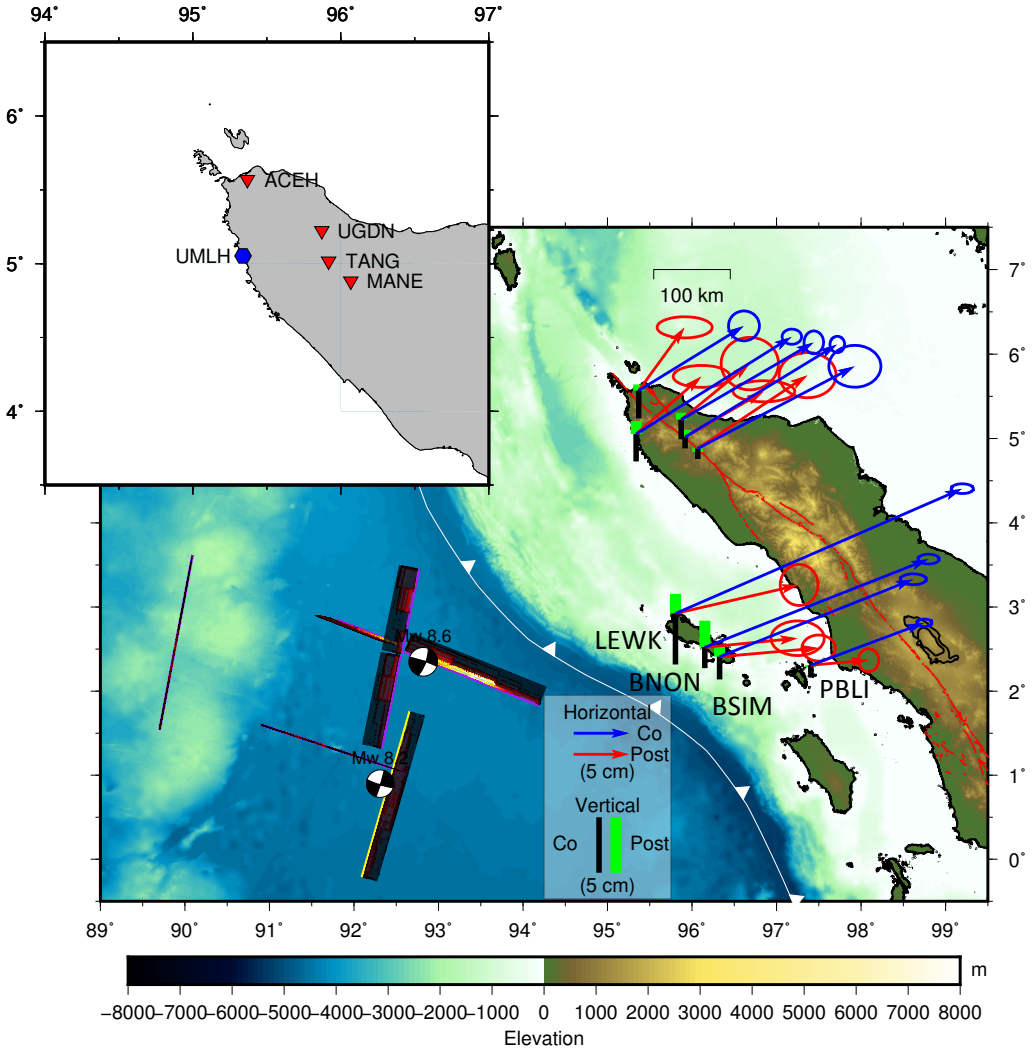

Figure 3.8 Blue arrow and black bar denotes horizontal and vertical coseismic offsets, respectively. Red arrow and green bar denotes horizontal and vertical component of postseismic displacement, respectively. Co and Post in the map legend denotes coseismic and postseismic, respectively.

Table 3.4 Coseismic displacement

No	Site Name	Coseismic displacement (mm)						Remark
		NS	σ NS	EW	σ EW	UD	σ UD	
1	ACEH	58.2	5.5	94.9	5.7	-25.1	8.6	
2	UGDN	69.7	4.2	119.5	3.6	-17.7	10.5	
3	MANE	74.1	7.7	141.6	9.6	-9.5	7.1	
4	TANG	83.5	3.1	137.2	2.7	-10.1	3.2	
5	UMLH	87.7	2.8	140.3	3.6	-24.6	2.1	
6	LEWK	112.4	1.8	258.5	4.1	-45.9	1.2	
7	BNON	79.5	1.8	201.7	3.9	-18.7	1.1	
8	BSIM	69.8	2.1	174.6	4.8	-20.4	1.2	
9	PBLI	38.2	1.4	102.3	2.8	-11.1	1.3	

σ : Standard deviation

Table 3.5 2-years postseismic displacement

No	Site Name	Postseismic Displacement (mm)						Remark
		NS	σ NS	EW	σ EW	UD	σ UD	
1	ACEH	56.9	3.8	41.4	10.1	5.4	11.1	
2	UGDN	50.5	9.6	61.7	10.5	6.2	9.9	
3	MANE	66.1	8.3	98.9	10.4	-2.9	7.4	1.5 year
4	TANG	41.2	3.8	71.1	11.3	6.4	13.6	
5	UMLH	51.9	4.1	58.9	10.4	11.7	17.2	
6	LEWK	25.7	7.5	111.4	6.9	17.6	7.2	
7	BNON	9.8	6.3	83.6	9.8	24.1	9.2	
8	BSIM	7.8	4.7	89.2	6.1	10.6	7.6	
9	PBLI	4.5	4.2	51.9	3.7	-1.8	7.1	

σ : Standard deviation

4 Finite Element Method

One of the widely used methods, which is engineering-oriented, to solve problems numerically in continuum mechanics is a finite element method. The method has significantly improved how we look at a complex problem in various geophysical studies (e.g. Braun, 2003; Lechmann et al., 2011; Stadler et al., 2010). In crustal deformation studies, static surface deformation has been represented by a fault dislocation (e.g. Sato, 1971). Moreover, since a precise and reliable method for introducing fault dislocations (e.g. Aagaard et al., 2013b; Melosh and Raefsky, 1981) had been demonstrated, the study of coseismic and postseismic deformation that incorporates complexity as natural phenomena has increased. Several studies did finite element analysis with heterogeneity such as stress of faulting (e.g. Zhao et al., 2004), coseismic rupture considering 3-D elastic structure (e.g. Hashima et al., 2016), depth-dependent viscosity (e.g. Freed et al., 2017), and spherical model of viscous relaxation studies (e.g. Hu & Wang, 2012b).

The finite element method gives an ability to combine various heterogeneity models to study coseismic and postseismic process. A few advantages of utilizing the finite element method are able to combine the complex geometry such as slab, topography, as well as the spherical surface that represent earth curvature with spatial

variation of a parameter in any model dimension. Additionally, the finite element method is able to modify almost all condition that makes the FE a great multi-purpose analysis tools.

In this study, we aim to investigate the rheology structure under the Indian Ocean based on postseismic deformation following the 2012 Indian Ocean earthquake sequence inferred from GNSS data. As mentioned in chapter 3, the GNSS sites that recorded clear postseismic transients are limited at mid-field GNSS sites in the Northern Sumatra. The rupture location is offside the trench through the Sunda trench. Previous studies found the indispensable effect due to slab in megathrust cases (Pollitz et al., 2008; Wang et al., 2018; Yoshioka & Suzuki, 1999). In the case of the megathrust 2004 Sumatra-Andaman earthquake, the effect of the slab is vigorous in the near field and reduced 20% displacement in the far-field (Pollitz et al., 2008). Furthermore, the site-to-source distance is more than 300 km as described in chapter 3. Based on previous studies (Nostro et al., 1999; Pollitz, 1997), the effect of earth curvature is essential in the calculation of surface displacement for more than 300 km.

Here, in Chapter 4, we used the Finite Element (FE) method to model coseismic and postseismic deformation due to the 2012 Indian Ocean earthquake in order to obtain a rheology picture under the Indian Ocean. Following sub-chapters will describe related with the FE method that applied in this studies. First, we showed how we build the geometrical domain of the finite element mesh based on the geological setting derived from various observations in previous studies. Second, we described the boundary conditions and material implemented on the designated FE codes PyLith (Aagaard et al., 2015; Aagaard et al., 2013; B. Aagaard et al., 2015). Also, we describe our attempt to optimize the computation process. Third, we assess the response of the model parameter in our constructed model.

4.1 Finite Element Mesh

In the finite element method, we need to construct a finite element mesh as a processing domain. Before making a finite element mesh, we create a solid model that represents the target region. Following description is about the geometry configuration for my solid model, mesh form, sizing and testing for the effect of different mesh size, a spherical mode in the finite element mesh, and buried finite fault plane implementation for the intraplate earthquake in three-dimensional heterogeneous structure.

4.1.1 Geometry Configuration

We compiled previously published geometry structures to create the finite-element solid model (Figure 4.1). We used Cubit 13.0 Software (https://cubit.sandia.gov/) to make a solid model and mesh it with tetrahedral mesh. The geometry of the model strongly depends on the how we construct the solid model, while the spatial database such as velocity structure or viscosity will be defined separately on PyLith configuration file.

We intend to construct the model that retains the Earth's curvature. The model that retains the Earth's curvature is based on a spherical geometry using a local geographically referenced Cartesian system that reflects Earth-Centered Earth-Fixed (ECEF) coordinates (Aagaard et al., 2013a). Hereinafter, all surfaces to construct the solid model has the spherical characteristic.

Firstly, we model the first surface of the solid model taken from surface topography and bathymetry based on Becker et al. (2009). Secondly, we model the

second surface as the subducting slab interface along the Sunda trench based on the seismic model of Gudmundsson and Sambridge (1998) extrapolated down to our model depth.

We made the whole geometry as a block based on the first surface using "sweep" command of Cubit package. Then, we divide the block using the second surface with a specified thickness to form oceanic lithosphere and down going subducting slab. So that oceanic lithosphere represents a three-dimensional subducting slab and the thickness of oceanic lithosphere can be easily modified. To form a continental lithosphere with a specified thickness, we divide the block on the continental side (eastern part of the slab) using the first surface. Finally, we have a 3-D model of solid geometry that incorporate subducting elastic slab, the sphericity of the earth as well as heterogeneous topography and bathymetry (Figure 4.1)

Our model space extended between longitudes 70°E to 115°E (~4500 km) and latitudes 20°S to 20°N (~4000 km). Also, we fixed the base of asthenosphere at 220 km and depth of our model at 670 km (Dziewonski and Anderson, 1981). We tested the influence of model size by changing the model size by half (~2250 km × 2000 km) and found no effect in the model displacement at the GNSS sites. Compared to the model size in several previous studies (Freed et al., 2017; Hu et al., 2016; Hu & Wang, 2012b), they fixed the model size around 1000 km from the epicenter that claimed to have negligible deformation at their far-field GNSS site. Our geographical extent of the model is larger than previous studies.

4.1.2 The Mesh Model and Effects of Mesh size

The finite-element mesh consists of more than 5 million tetrahedral elements and contained almost 1 million nodal points (Figure 4.2). We put the finest element

along the fault plane of the 2012 Indian Ocean earthquake. Also, along the plate interface between the Indo-Australian plate and the Eurasian plate. The finest element should be set at the region that potentially has high strain. The finest element size was 2.5 km near the source area and the subduction region while the roughest element size was 100 km at the edge of the model boundary. In order to evaluate the effect of mesh size, we tested with several numbers of mesh size (Figure 4.3) and concluded negligible effect on our GNSS site within two-years (Figure 4.4).

4.1.3 Buried Fault Plane Implementation

In the finite element method, we need a surface to represent a fault where faulting is applied. We can define the surface produced by an intersection between oceanic and continental blocks in the megathrust case along the trench. However, in the case of intraplate faulting, we need an additional surface that buried in the middle of the oceanic block. In Cubit software, is not possible to put additional small surface within a huge oceanic block. In order to divide a block with a surface, the edge of the surface should reach each edge of the block. Therefore, to apply buried fault planes in that circumstance, we make additional small block within oceanic block based on surface fault plane. Thus, we can put a surface in the buried volume as a buried fault plane.

4.2 PyLith for Crustal Deformation Studies

We conducted a finite-element analysis using PyLith code from the Computational Infrastructure for Geodynamics (CIG) website (https://geodynamics.org/cig/software/pylith/) with a fault interface based on the

domain decomposition method (Aagaard et al., 2013b). The PyLith code has been widely used for crustal deformation modeling such as elasto-viscoelastic modeling (Hines and Hetland, 2016), to study viscoelastic responses (Diao et al., 2013), stressing rates and deformation (Ali and Freed, 2010), gravity study (Gómez et al., 2017) and also source-inversion modeling using a derived finite-element Green's function (Hsu et al., 2014).

4.2.1 Boundary Condition

For simplicity, we follow default roller conditions at each boundary except for the surface: the surface boundary condition was a free displacement. The roller condition means that displacements are fixed in the normal direction but free in tangential directions. Some postseismic studies (e.g. Freed et al., 2017) utilized finite element method that used zero displacements for boundary condition. However, since our model size is quite large, changing to zero displacement boundaries has no effect on our GNSS site that used in this study. We used the roller condition as a default of PyLith configuration. In previous studies (Hu et al., 2016; Freed et al., 2017), the effect of roller condition is negligible, which the model size is smaller than our model.

4.2.2 Elastic Material

We set up a 3D elastic isotropic material model in this study. The generalized form of Hooke's law relating stress and strain for linear elastic materials could be illustrated as a spring as shown in Figure 4.5. The physical properties of the elastic model can be characterized by Lame's constant (μ, λ) and density (ρ). In PyLith, to describe the physical property of elasticity, we need an elastic input based on shear

wave speed (v_s), compressional wave speed (v_p) and density (ρ) to follow the equations below

$$\mu = \rho v_s^2 \tag{9}$$

$$\lambda = \rho v_p^2 - 2\mu \tag{10}$$

The 2012 Indian Ocean earthquake occurred off the western Sunda trench, but the GNSS stations are on the eastern part of the Sunda trench across the complex subduction region, we incorporated the subducted slab as an elastic overlying plate. Instead of using homogeneous rigidity, we adopted heterogeneous rigidity based on the three-dimensional velocity structure. Inhomogeneity, either of the stratified layered earth or the heterogeneous earth, has a slight effect on coseismic deformation considering the model difference (Hashima et al., 2016), but is an indispensable factor for near-field postseismic deformation (Pratama et al., 2017, AGU Fall Meeting). Hashima et al. (2016) investigate the effect of homogeneous and heterogeneous elastic structure models during the Tohoku-Oki earthquake. They found maximum slip during inversion is slightly changes from 38.5 m in the homogeneous to 39.6 in the layered model and 37.3 m in the model that slab is included. On the other hand, Pratama et al. (2017, AGU Fall Meeting) investigate the effect of spatial variation on elastic properties and found that the effect is significant in the mid-field.

We assumed shear wave speed and compressional wave speed based on a three-dimensional velocity structure from seismic studies following Widiyantoro and Hilst (1997). For the outside area of this study, our model is based on the AK135 global seismic velocity model (Kennett et al., 1995). We defined the density

following the Gardner relationship (Gardner et al., 1974), in which density is calculated from P-wave velocity as follows

$$\rho = aV_p^{(1/4)} \tag{11}$$

where density ρ is in g/cm^3, a is 0.31 since the V_p is in m/s. Constant a is an empirically derived factor that relates V_p to the density of rock.

4.2.3 Viscoelastic Material

There are several viscoelastic models supported in PyLith. However, in this study, we used only uni-viscous (Maxwell) and bi-viscous (Burgers) viscoelastic models. The first viscoelastic model is linear Maxwell, which is represented by a combination of linear elastic spring and linear viscous dashpot in series (Figure 4.5). When a Maxwell material is subjected to constant stress, there is an immediate elastic strain corresponding to the response of the spring and a viscous strain that increases linearly in time. In our finite element model, the elastic parameters are defined as described in the previous section. We assign Maxwell viscosities by simply put the viscosity value in the unit of Pascal-second (Pa s).

The second viscoelastic model is bi-viscous (Burgers) model derived from the Generalized Maxwell model following Hines and Hetland (2016). The Generalized Maxwell viscoelastic model consists of a number of Maxwell linear viscoelastic models in parallel with a spring (Figure 4.5). A number of common material models may be obtained from this model by setting the shear moduli of various springs to zero and infinity (or a large number), such as the Maxwell model, the Kelvin model, and the standard linear solid (Aagaard et al., 2015). Hetland (personal communication, 2015) compared analytically the equivalence of parameters in

General Maxwell and the General Kelvin representations of a Burgers rheology. A Burgers rheology is represented by a four-element general Maxwell configuration, which consists of two Maxwell elements in parallel with normalized shear modulus (total shear $\mu_{tot} = \mu_1 + \mu_2$, then normalized shear modulus $\lambda_i = {}^{\mu_i}/_{\mu_{tot}}$ where $\lambda_1 + \lambda_2 = 1$) and two viscosity. Meanwhile, a Burgers rheology is represented by a six element general Kelvin configuration, which consists of three Kelvin elements in series, with shear and viscosity, where one of the shear modulus and one of the viscosity is zero. Hetland (personal communication, 2015) calculate the creep and relaxation function of each model then produce the same curve when assigns the same rheology parameter. Hence, in order to implement the burgers model, we give equal shear moduli and assign the first viscosity as linear Kelvin viscosity and second viscosity as linear Maxwell viscosity.

4.2.4 Optimum Computation Speed

Although the finite element method can deal with various problems in a flexible manner, one big challenge is its computation cost. The problem becomes very big easily, requiring a large number of memories, and computation time take a very long time. In that sense, we search for an optimum parallel processing with multiple thread/processor environments. The specification of the computer in this study is using 88 processor Intel® Xeon® CPU E5-2699 with clock speed of 2.2 GHz. Since our machine is limited below 100 threads, we need an optimum number of threads that give the most efficient calculation. We tested the similar Finite Element calculation with a different combination of multiple threads. The tested calculation is to estimate two-year surface displacement due to viscoelastic relaxation in our model. We fixed all parameter except that we change the combination of threads, repeatedly.

Then, we found that after five threads, the computation time is almost similar even for 40 threads (Figure 4.6). Hence, we decided to use only five threads for a single set of parameter. In case of 100 threads available, a combination of five threads give us 20 sets of parameter to process instead of a combination of 40 threads that only give us 2-3 set of parameter to process.

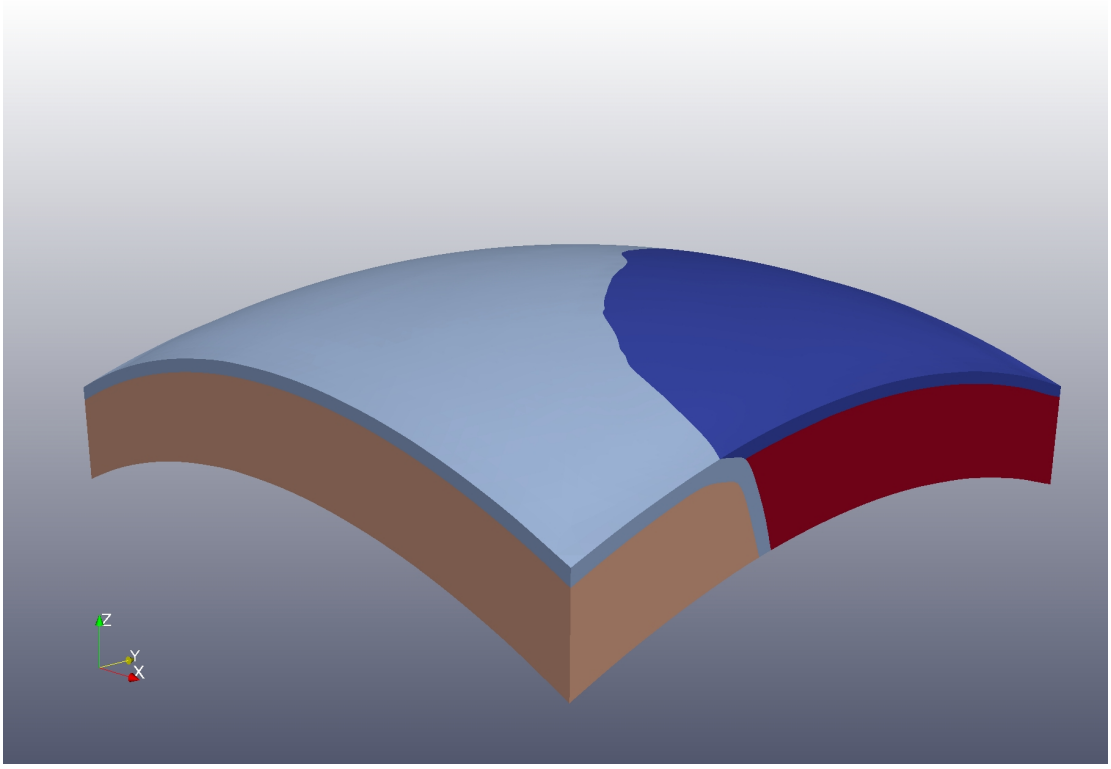

Figure 4.1 Solid Model for Finite Element Analysis. Dark blue and light blue represent continental and oceanic lithosphere, respectively. Red and light orange represent continental and oceanic asthenosphere, respectively. X, y and z axes denotes E-W, N-S and U-D direction.

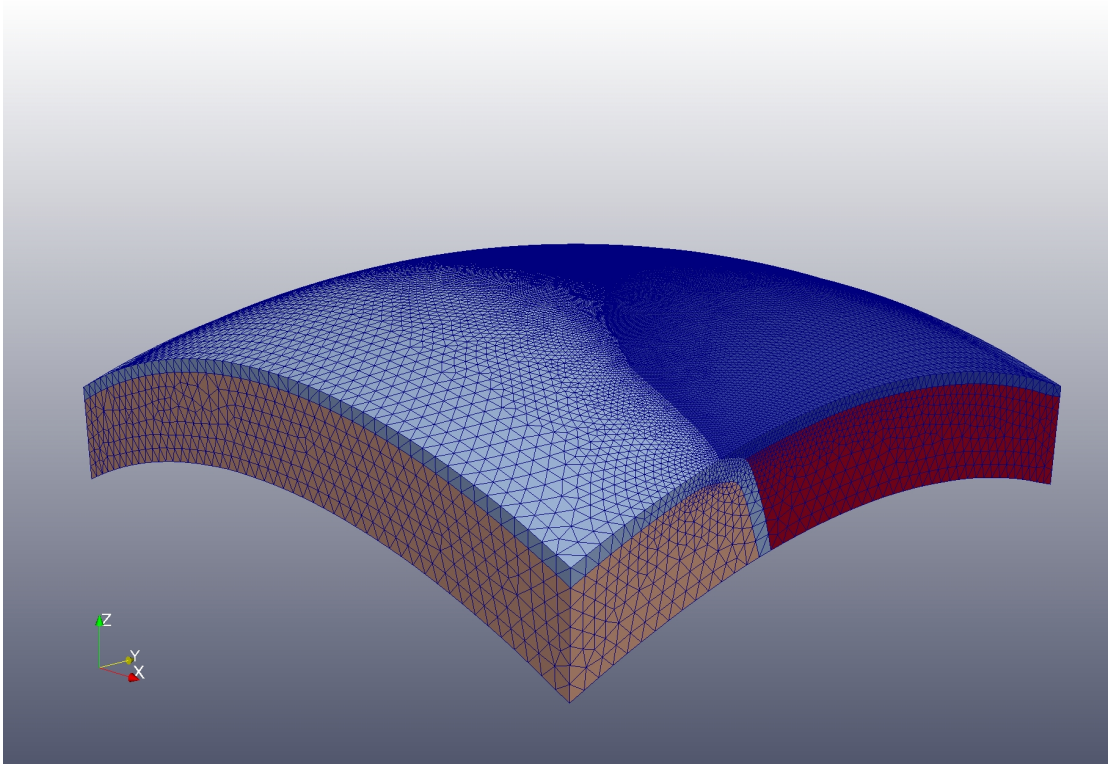

Figure 4.2 Meshed geometry for Finite Element model. Color solid model and axes representation same as Figure 4.1.

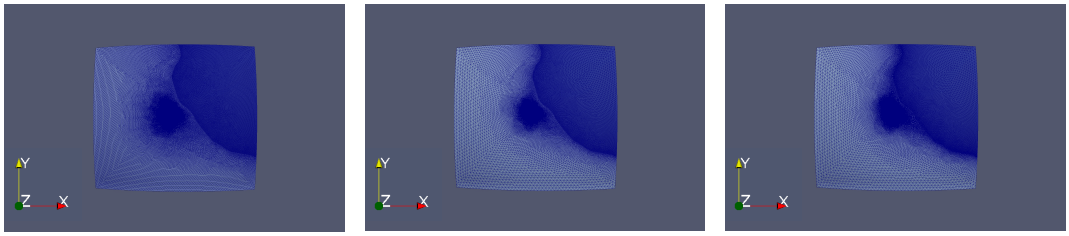

(a) (b) (c)

Figure 4.3 X, y, and z axes represent E-W, N-S and U-D direction, respectively. (a) Mesh size with the finest 2.5 km to rough size 50 km, (b) Mesh size with the finest 2.5 km to rough size 100 km that used in this study, (c) Mesh size with the finest 1.5 km to rough size 100 km.

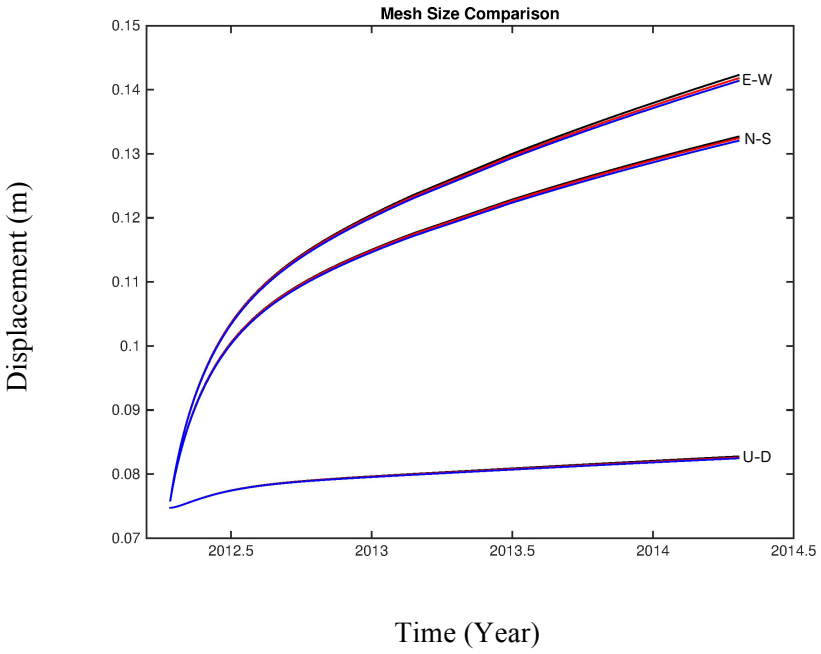

Figure 4.4 Mesh size effect comparison at the UMLH site. Each line represents mesh size from the finest size on fault to rough mesh on model space boundary. Black, red and blue lines indicate 2.5 km to 50 km, 2.5 km to 100 km, and 1.5 to 100 km that used for modeling, respectively.

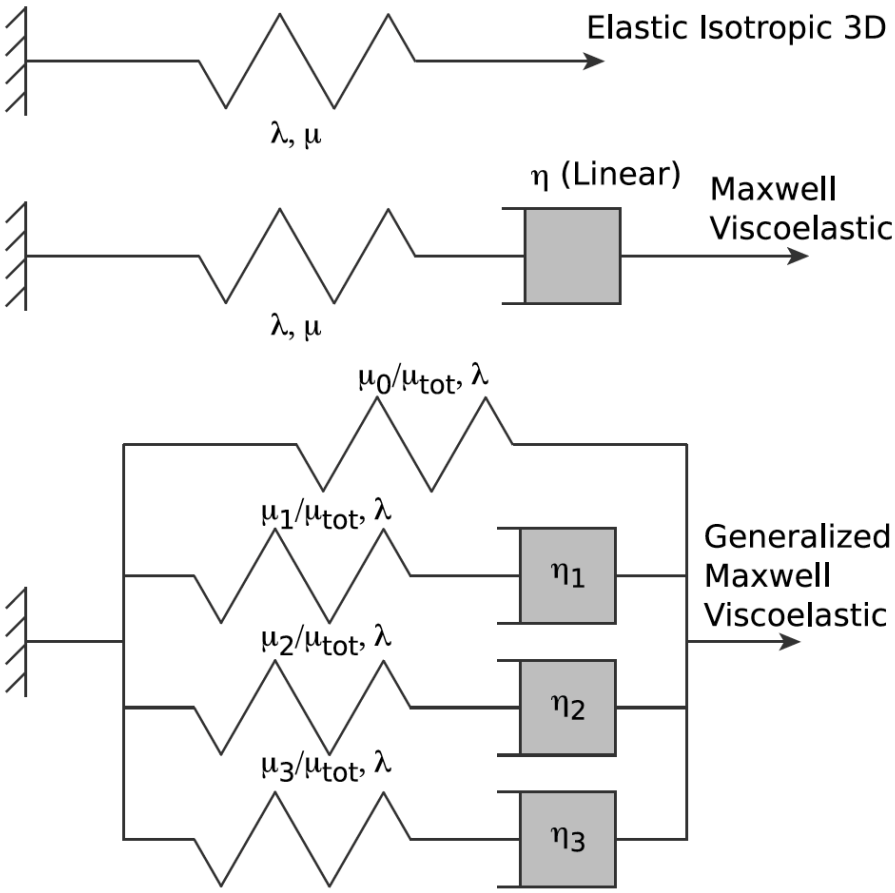

Figure 4.5 Spring representation of elastic isotropic model and spring-dashpot representation of viscoelastic material models for PyLith. The top model is a linear elastic model, the middle model is a Maxwell model, and the bottom model is a Generalized Maxwell model. For the power-law model, the linear dashpot in the Maxwell model is replaced by a non-linear dashpot following a power-law. (Same as Figure 5.1 of Aagaard et al., (2013a)).

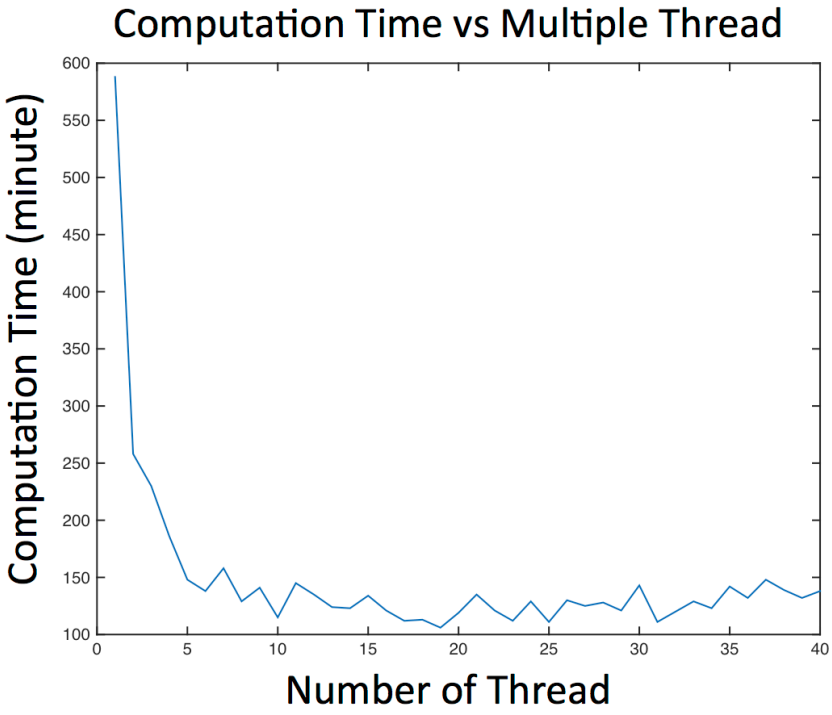

Figure 4.6 Several test case using simple viscoelastic relaxation process with same parameter but different multiple thread.

5 Analysis of Coseismic Deformation

Coseismic faulting re-distributes stress built-up over the interseismic period. Coseismic stress change drives viscoelastic relaxation in the mantle and afterslip on faults. Postseismic deformation has been modeled with a linear viscoelastic model and afterslip (e.g. Gunawan et al. 2014, Sun et al. 2014, Freed et al. 2006).

Freed et al. (2017) pointed out the coseismic model error may propagate into postseismic modeling results. Different coseismic fault models would produce different patterns of coseismic stress change (Gunawan et al., 2016). Hence, we attempt to evaluate and verify the best coseismic fault model based on the coseismic offsets. Later, we will use the preferred coseismic fault model for postseismic modeling.

Here, in Chapter 5, we evaluate and compare previously published coseismic fault models. Following sub-chapters will describe analyses of coseismic deformation due to the 2012 Indian Ocean earthquake. First, we describe the 2012 Indian Ocean earthquake sequence. Second, we elaborate several coseismic fault models based on previous studies. Third, we evaluate the available coseismic fault models as a coseismic fault model for postseismic deformation modeling.

5.1 The 2012 Indian Ocean earthquake

The 2012 Indian Ocean Earthquake sequence first occurred as the Mw 8.6 mainshock, followed by the Mw 8.2 aftershock (Figure 5.1a). These largest oceanic intraplate earthquakes had a long duration of rupture about 160 s and 60 s for two events, respectively. It ruptured a complex conjugate fault system at diffuse plate boundary with a very large amount of slip up to 48 m and deep slip at 60 km depth (Hill et al., 2015; Ishii et al., 2013; Wei et al., 2013).

5.2 Coseismic Fault Model based on Previous Studies

The two great earthquakes occurred within two hours at extremely complex conjugate faults, that consist of at least three major faults for Mw 8.6 main shock (Hill et al., 2015; Wei et al., 2013; Yue et al., 2012) and one fault for the Mw 8.2 aftershock (Wei et al., 2013). Several finite fault models were proposed to explain the observed crustal deformation and seismic waveforms. Yue et al. (2012), Satriano et al. (2012) and Wei et al. (2013) used seismic data to estimate the fault model. Meanwhile, Hill et al. (2015) not only used the seismic data but also include high rate GPS data to estimate the fault model. However, these fault models have several essential differences. These fault models suggest difference on fault orientation and the largest slip. Initially, previous analyses estimated the largest slip in NNE left lateral with dominant deep slip (Satriano et al. 2012; Wei et al. 2013). On the other hand, other analyses suggest the largest slip in WNW right-lateral faults structure with dominant shallow slip (Yue et al. 2012; Hill et al. 2015).

We focus on evaluation and comparison of the latest two-fault models by Wei et al. (2013) and Hill et al. (2015). These fault models are referred hereafter as Wei model (Wei et al. 2013) (Figure 5.1d) and Hill model (Hill et al. 2015) (Figure 5.1c).

These two models are the latest studies that show different fault orientation and the largest slip. These differences may arise due to the different assumption on fault location and different data sets.

5.2.1 Wei Model

Wei et al. (2013) reported a fault model for the mainshock Mw 8.6 and the largest aftershock Mw 8.2 by joint inversion of regional and teleseismic waveform data. They obtained the complex fault system consists of three fault planes for Mw 8.6 that intersecting each other with a fault width down to the depth of 50 km. The rupture starts from the WNW plane ($89^o/289^o$ for dip/strike) (No. 1 in Figure 5.2), smoothly propagated to the NNE plane ($74^o/20^o$) (No. 2 in Figure 5.2) and lasted about 200 s in the third plane ($60^o/310^o$) (No. 3 in Figure 5.2). For Mw 8.2, they inferred a single plane ($74^o/16^o$) (No. 4 in Figure 5.2) with a short 60-second duration ruptured to 50 km deep extent. They calculate the seismic moment due to the mainshock Mw 8.6 about 1.3 x 10^{22} N m. We imaged the 3D view of the Wei model in our 3D Finite Element model (Figure 5.2).

5.2.2 Hill Model

Hill et al. (2015) inferred a fault model for the mainshock Mw 8.6 only. The basic fault geometry was based on the locations of aftershocks and previously published backprojection results (Yue et al., 2012). They optimize the fault strike and dip to fit the data. Based on a joint inversion of high-rate GPS data from SuGAr network, source time functions from broadband surface waves, teleseismic observations and static GPS displacements, they found the optimum slip distribution

for Mw 8.6 that consists of six fault planes (Figure 5.3) with the greatest slip 48 m at WNW orientation. They obtained the total seismic moment about 1.2 x 10^{22} N m.

Since the provided horizontal and vertical GNSS data in this study is a daily solution, we modified fault model from Hill et al. (2015) with additional fault plane for Mw 8.2 based on Wei et al. (2013). We found that the offset based on the largest aftershock Mw 8.2 is significant in our GNSS data. We summarized the main differences between both fault models as shown in Table 5.1

5.3 Evaluation of the Coseismic fault models

Maulida et al. (2016) and Gunawan et al. (2016) investigate the best-fit coseismic model of the 2012 Indian Ocean earthquake using horizontal component of GNSS data with the assumption of homogeneous half-space and layered spherical-earth model, respectively. However, those studies reached different conclusions of the best-fit coseismic model. Pratama et al. (2017) reported the systematic effects of model simplification such as half-space model or homogeneous earth structure. Here, we further investigate the simplification effect by using a 3-D heterogeneous earth model based on horizontal and vertical GNSS data, which was not included in the previous analysis.

5.3.1 Coseismic GNSS Observation Data

We compiled the coseismic offset of GNSS site based on daily solution taken from previous studies (Feng et al., 2015; Gunawan et al., 2016; Hill et al., 2015; Maulida et al., 2016; Yadav et al., 2013) including our AGNeSS dataset in this study. The total number of observation sites is 100 in mid-field and far-field. There are 200

horizontal offsets and 34 vertical offsets. Clear vertical offsets are found for mid-field sites of AGNeSS (Aceh GNSS Network for the Sumatran fault system), SuGAr (Sumatran GPS Array), and InaCORS (Indonesian Continuously Operating Reference Stations).

We obtained clear landward displacement and subsidence in northern Sumatra as shown in Figure 5.1a. In the northern part, GPS sites in the Nicobar-Andaman Island network moved southward. Meanwhile, in the southern part, the SuGAr and InaCORS sites moved northward. These displacements exhibited a strike-slip fault mechanism of the earthquake.

5.3.2 The Preferred Coseismic Fault Model

The elastic properties on fault give a significant contribution to the surface displacement (Hashima et al., 2016; Pollitz, 1997; Pratama et al., 2017). To compare both model properly, we calculate the fault model that reflects the original seismic moment, that is the estimated seismic moment from the model is taken. Original seismic moment of Wei model and Hill model are taken from Wei et al. (2013) and Hill et al. (2015), respectively. In our model, we tried to match the original moment with scaling slip. Wei model and Hill model need to scale up to 1.33 and 1.09 times from the original slip, respectively. The original slip of Wei model and Hill model are taken from Wei et al. (2013) and Hill et al. (2015), respectively.

We used separate root mean square for each component to accommodate the different size of data. So, for every GNSS station, we used horizontal i and vertical n to evaluate the calculation offset Cal and observation offset Obs as following

$$Misfit = \sqrt{\frac{1}{I}\sum_{i=1}^{I}\left(Obs_{hor,i} - Cal_{hor,i}\right)^2} + \sqrt{\frac{1}{N}\sum_{n=1}^{N}\left(Obs_{ver,n} - Cal_{ver,n}\right)^2} \quad (12)$$

We obtained misfit for Wei and Hill models are 41.07 and 37.37, respectively. For both models, scale up the coseismic slip cause horizontal misfits decrease slightly but the vertical misfits are increased. The misfit suggests the Hill model predict the observation better than Wei model for both horizontal and vertical observations. Coseismic offset based on Hill model slightly underestimates horizontal observation but overestimates vertical observation (Figure 5.4a). However, the Wei model overestimates coseismic offset for both horizontal and vertical components (Figure 5.4b).

Gunawan et al. (2016) investigated numerous coseismic models with a layered spherical earth model (Pollitz, 1997). They showed that the Hill model is the best model. They also tested using the half-space model (Okada, 1992) and found the Hill model had a larger misfit compared with the layered spherical earth. Maulida et al. (2016) used a half-space model and found the Hill model the largest misfit among the tested model. Since we cannot find the estimated magnitude in Maulida et al. (2016) and Gunawan et al. (2016), one problem of these studies is the evaluation was conducted without verification of the total moment magnitude. Another problem is that those studies examined the horizontal component only whereas the vertical component also provides a significant contribution in the mid-field. By using all the three GNSS components and a similar total seismic moment in Wei et al. (2013) (for

Wei model) and Hill et al. (2015) (for Hill model), we found the Hill model misfit (37.37) is smaller than Wei model misfit (41.07).

Based on above analysis of coseismic fault model, we used the prescribed slip distribution from Hill et al. (2015) for the Mw 8.6 mainshock and that of Wei et al. (2013) for the Mw 8.2 aftershock to accommodate our daily solution. Compared with other studies such as Yue et al. (2012) and Wei et al. (2013), the coseismic offset calculated based on Hill et al. (2015) showed a better agreement as reported in Gunawan et al. (2016). Forward modeling was used to obtain the surface displacement at each site. Based on this model and two years of GNSS data from northern Sumatra, we obtained estimates of asthenosphere viscosity and lithosphere thickness.

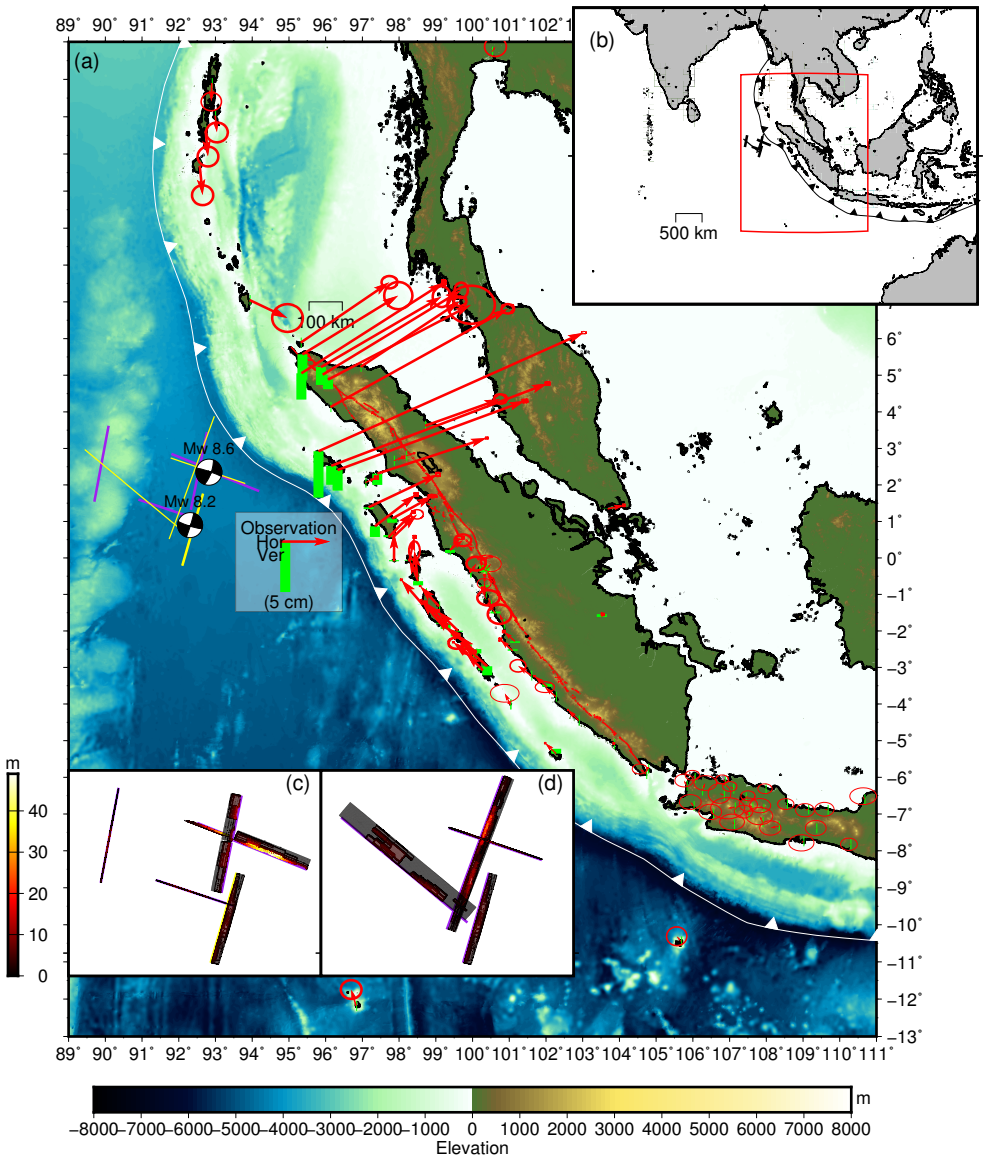

Figure 5.1 (a) Red arrows and green bar indicate observed horizontal and vertical GNSS data, respectively. Purple line and yellow line shows different fault trace of Wei Model and Hill Model, respectively. Red lines in Sumatra Island are Great Sumatra Fault while white line with triangle represents Sunda Trench. Surface topography and bathymetry are based on Becker et al. 2009, (b) Wider area; red rectangle is selected area of (a) in Figure 5.1. (c) Fault slip distribution of Hill Model and (d) Fault slip distribution of Wei Model, color denote slip amount in meter (m).

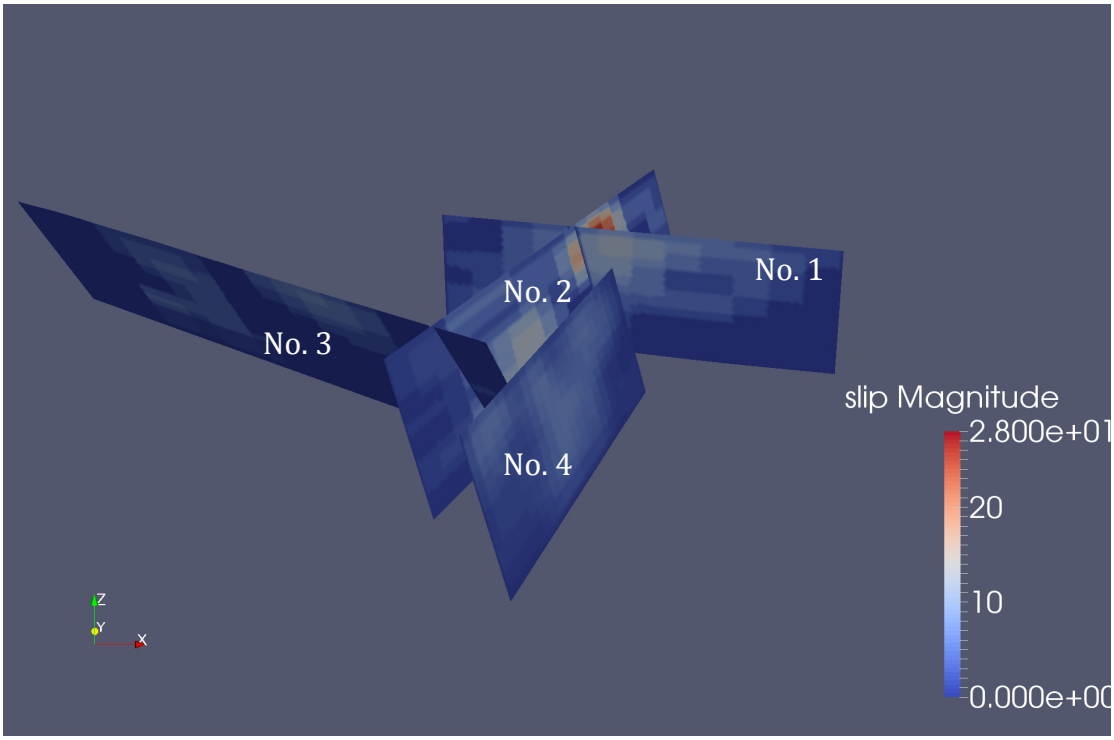

Figure 5.2 The 3D view of coseismic slip distribution of Wei model. Slip magnitude in meter. Y-axis and x-axis denotes North and East directions, respectively.

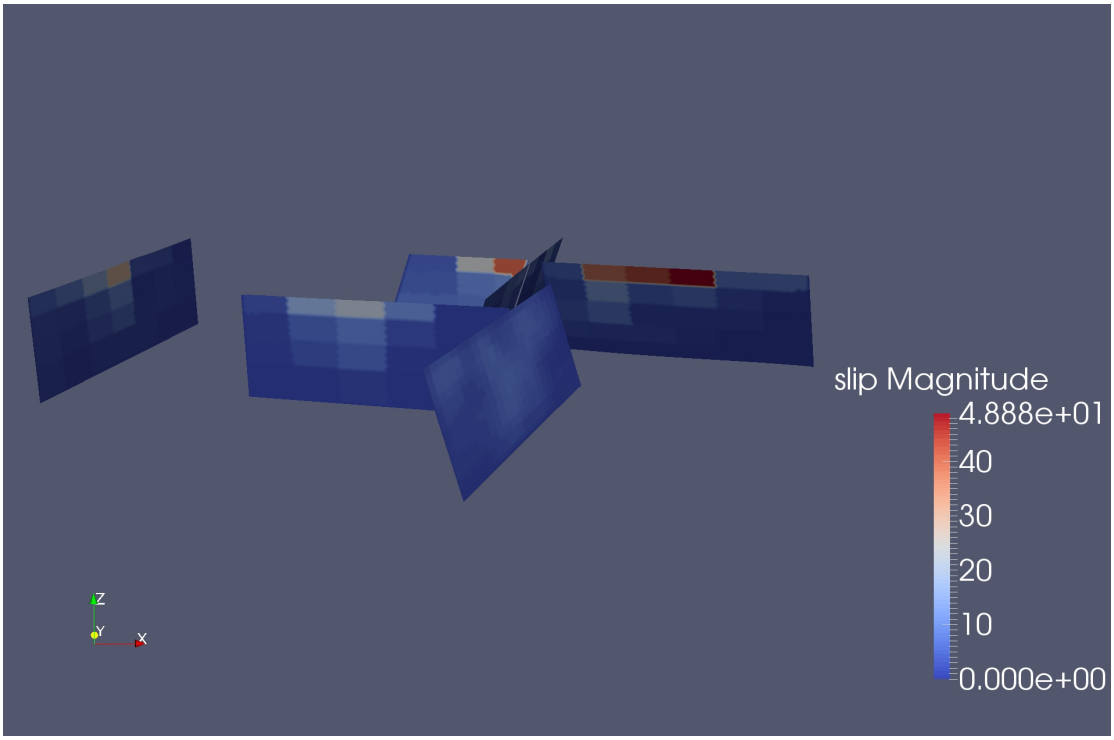

Figure 5.3 The 3D view of coseismic slip distribution of Hill model. Slip magnitude in meter. Y-axis and x-axis denote North and East directions, respectively.

Table 5.1 Coseismic fault model characteristic for Wei and Hill models

Parameter	Wei Model	Hill Model
Main Orientation	NNE	WNW
Number of Fault Plane (Mw8.6)	3	6
Maximum Coseismic Slip Amount	28 m	48 m
Dominant Depth Slip	Deep	Shallow
Original Seismic Moment	13×10^{21} N m	12×10^{21} N m
Original Data Constraint	Regional, teleseismic	Regional, teleseismic, 1 Hz GPS data

Table 5.2 Coseismic offset that used to evaluate coseismic fault model

No	Site	Coseismic displacement (unit in mm)						Network
		NS	σ NS	EW	σ EW	UD	σ UD	
1	ACEH	58.2	5.5	94.9	5.7	-25.1	8.6	AGNeSS
2	UGDN	69.7	4.2	119.5	3.6	-17.7	10.5	AGNeSS
3	MANE	74.1	7.7	141.6	9.6	-9.5	7.1	AGNeSS
4	TANG	83.5	3.1	137.2	2.7	-10.1	3.2	AGNeSS
5	LEWK	117.4	0.5	262.8	1	-45.9	1.2	SuGAr
6	BNON	81.6	0.5	214.4	0.8	-18.7	1.1	SuGAr
7	BSIM	68.4	0.5	185.6	0.9	-20.4	1.2	SuGAr
8	PBLI	35.3	0.4	108.5	0.6	-11.1	1.3	SuGAr

Table 5.2 (continuation)

No	Site	Coseismic displacement (unit in mm)						Network
		NS	σ NS	EW	σ EW	UD	σ UD	
9	UMLH	90	0.8	141.1	0.7	-24.6	2	SuGAr
10	ABGS	12	0.7	9.8	1.6	-3	1.3	SuGAr
11	BITI	22.3	0.4	40	1.5	-4.1	1.6	SuGAr
12	BSAT	17.1	0.3	-16.9	0.4	2.2	1.1	SuGAr
13	BTET	24.7	0.4	-21.3	0.4	0.2	0.9	SuGAr
14	BTHL	24.8	0.3	24.7	0.5	2.1	0.9	SuGAr
15	BUKT	8.6	0.6	2.7	2.2	-6.9	2.2	SuGAr
16	HNKO	31.5	0.5	40.9	0.6	-10.6	1.8	SuGAr
17	JMBI	2.5	0.2	0.9	0.3	2.7	0.7	SuGAr
18	KTET	17.1	0.4	-20.3	0.4	-5.2	1.1	SuGAr
19	LAIS	10.6	0.2	-12.6	0.3	2.6	0.7	SuGAr
20	LHW2	32.5	0.8	68.6	0.9	-1.8	1.8	SuGAr
21	LNNG	9.7	0.2	-11	0.3	-1.4	0.8	SuGAr
22	MKMK	11.1	0.3	-12.2	0.3	1.5	0.9	SuGAr
23	MLKN	10.3	0.3	-10.9	0.3	4.7	1	SuGAr
24	MNNA	10.6	0.2	-10.6	0.2	0	0.7	SuGAr
25	MSAI	20	0.2	-18.8	0.3	0	0.7	SuGAr
26	NGNG	20.9	0.3	-19.9	0.4	-5.3	1.2	SuGAr
27	NTUS	3.4	0.2	16	0.2	0.3	0.5	IGS
28	PARY	10	0.3	0.5	0.4	-1.4	1	SuGAr
29	PBJO	20.7	0.3	-8.4	0.4	-4.2	0.9	SuGAr

Table 5.2 (continuation)

No	Site	Coseismic displacement (unit in mm)						Network
		NS	σ NS	EW	σ EW	UD	σ UD	
30	PKRT	19.6	0.3	-20	0.3	2.5	0.9	SuGAr
31	PPNJ	19.3	0.3	-19.7	0.3	-1	0.8	SuGAr
32	PRKB	21.8	0.4	-24.1	0.4	-9	1.2	SuGAr
33	PSKI	10.3	0.3	-2.6	0.3	-0.2	0.9	SuGAr
34	PSMK	28.1	0.3	0.1	0.3	1	0.9	SuGAr
35	PTLO	22.8	0.3	5.1	0.3	-0.7	0.7	SuGAr
36	SLBU	16.5	0.3	-19.2	0.4	0	1	SuGAr
37	SMGY	17.6	0.3	-17	0.4	4.3	1	SuGAr
38	TLLU	23.2	0.3	-19.3	0.3	0.8	0.8	SuGAr
39	TRTK	9.5	0.3	-6.6	0.3	1.9	0.8	SuGAr
40	KRUI	0.54	0.23	-0.25	0.29	-	-	SuGAr
41	MEGO	1.31	0.17	-1.35	0.28	-	-	SuGAr
42	PBKR	4.88	0.34	10.9	0.57	-	-	SuGAr
43	PTBN	0.49	0.22	-0.61	0.33	-	-	SuGAr
44	RNDG	3.28	0.19	9.13	0.33	-	-	SuGAr
45	SDKL	2.69	0.29	8.05	0.23	-	-	SuGAr
46	SLBU	1.64	0.13	-1.37	0.27	-	-	SuGAr
47	SMGY	1.9	0.24	-1.37	0.23	-	-	SuGAr
48	TIKU	1.2	0.21	-0.1	0.23	-	-	SuGAr
49	TNTI	2.25	0.32	-0.75	0.35	-	-	SuGAr
50	CBAY	-17.8	5.6	37.5	6.2	-	-	N-A*

Table 5.2 (continuation)

No	Site	Coseismic displacement (unit in mm)						Network
		NS	σ NS	EW	σ EW	UD	σ UD	
51	HBAY	-29.4	4	2.9	4.3	-	-	N-A*
52	PORT	-25.7	4	2.4	4.2	-	-	N-A*
53	HAVE	-16.6	4	1.8	4.4	-	-	N-A*
54	MBDR	-18.3	3.7	-0.5	4.1	-	-	N-A*
55	PALK	-4.9	3.6	-0.5	4	-	-	IGS
56	COCO	16.1	3.8	-4.9	4.2	-	-	IGS
57	BAKO	1.8	4	-4.2	4.6	-	-	IGS
58	XMIS	5.1	3.8	-4.36	4.1	-	-	IGS
59	CUSV	5	4	3.4	4.4	-	-	IGS
60	DGAR	-5.3	4.1	-10.3	4.7	-	-	IGS
61	MLBU	9.7	3.9	-4.1	4.8	-	-	InaCORS
62	SAMP	26.5	1.9	74.4	2.5	-	-	InaCORS
63	SEBL	9.6	2.5	-13.2	3.2	-	-	InaCORS
64	SLBU	15.8	2.3	-16.4	3.2	-	-	InaCORS
65	TDAL	23.3	1.9	24.4	2.5	-	-	InaCORS
66	TIKU	8.8	2.8	5.7	3.9	-	-	InaCORS
67	TLOK	7.5	3.1	-2.5	4.5	-	-	InaCORS
68	TNBL	26.3	3.8	-3	2.2	-	-	InaCORS
69	CANG	3.1	2.6	-5	3.7	-	-	InaCORS
70	CBTU	2.2	2	-3.5	2.9	-	-	InaCORS
71	CCIR	-0.3	2.2	-1.1	3.3	-	-	InaCORS

Table 5.2 (continuation)

No	Site	Coseismic displacement (unit in mm)						Network
		NS	σ NS	EW	σ EW	UD	σ UD	
72	CCLP	-1.6	3.3	-2	5.1	-	-	InaCORS
73	CGON	2.7	2	-2.3	2.9	-	-	InaCORS
74	CJKT	1.9	1.8	-3	2.6	-	-	InaCORS
75	CJPR	3.1	3.4	-1.2	5.4	-	-	InaCORS
76	CJUR	-0.8	4.3	-7.1	6.9	-	-	InaCORS
77	CLBG	2.7	2.7	-4	3.7	-	-	InaCORS
78	CMIS	-1.8	2.9	-8.4	4.3	-	-	InaCORS
79	CMLP	3.9	3	-3.3	4.4	-	-	InaCORS
80	CPBL	0.3	3.1	-0.5	4.2	-	-	InaCORS
81	CPKL	0.7	2.8	-3.2	3.9	-	-	InaCORS
82	CPSR	5.2	2.6	-2.6	3.7	-	-	InaCORS
83	CAIR	9.9	2.4	12.6	3.4	-	-	InaCORS
84	CBKL	9.5	2.2	-10.9	3.9	-	-	InaCORS
85	CBKT	5.2	3.1	4.9	4.1	-	-	InaCORS
86	CPDG	8.9	2.1	-1.6	2.8	-	-	InaCORS
87	CSAB	59.8	2.5	87.9	3.2	-	-	InaCORS
88	CTCN	4.9	2	-6.5	3	-	-	InaCORS
89	LHMI	64.9	1.9	98.5	2.6	-	-	InaCORS
90	MEGO	11	3.6	-5.6	5.8	-	-	InaCORS
91	MEUL	97.3	1.9	175.6	2.5	-	-	InaCORS
92	CPTU	1.7	3.1	-2.8	4.6	-	-	InaCORS

Table 5.2 (continuation)

No	Site	Coseismic displacement (unit in mm)						Network
		NS	σ NS	EW	σ EW	UD	σ UD	
93	CPWK	1.7	2	2.2	2.9	-	-	InaCORS
94	CRKS	7.4	3	3.2	4.6	-	-	InaCORS
95	CROL	-0.1	2	-0.6	2.9	-	-	InaCORS
96	CRUT	6	3.5	-3.2	5.4	-	-	InaCORS
97	CSUM	3.2	2.9	-3.3	4.3	-	-	InaCORS
98	CTAN	1.9	3.2	-1.9	5	-	-	InaCORS
99	CTGL	-1	2.7	-3.2	3.8	-	-	InaCORS
100	JOGS	-0.1	2.5	-1.5	3.4	-	-	InaCORS

*N-A : Nicobar-Andaman Island

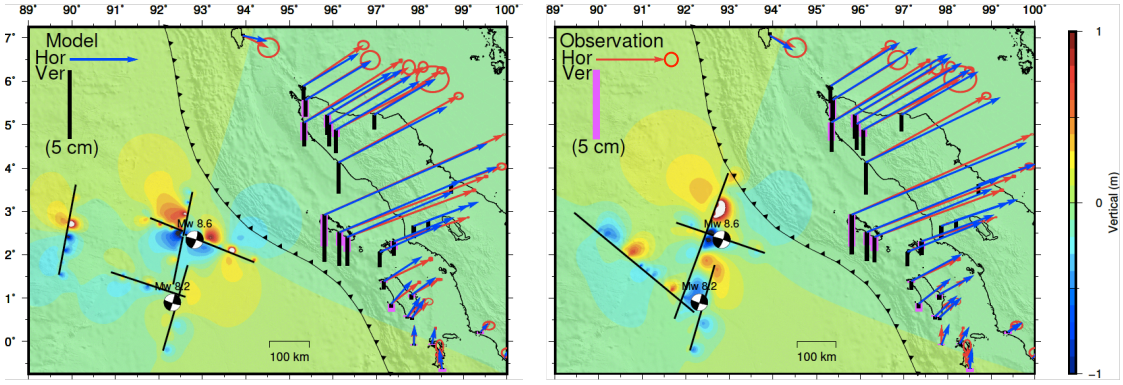

(a) (b)

Figure 5.4 Coseismic offsets comparison between calculation and observation in the mid-field region based on (a) Hill model and (b) Wei model.

6 Analysis of Postseismic Deformation

Great earthquakes cause extensive and long-lasting postseismic deformation. Postseismic motion, which can be detected by geodetic observation, may reflect a large contribution of viscoelastic relaxation in the upper mantle (Wang et al., 2012). In the case of the 2012 Indian Ocean earthquake, viscoelastic relaxation under the ocean may reflect the rheological properties in the oceanic asthenosphere, which is fundamental to understand plate tectonics.

Here, in Chapter 6, we will outline our analysis of postseismic deformation to obtain rheology model under the Indian Ocean. Following sub-chapters will describe analyses of postseismic deformation due to the 2012 Indian Ocean earthquake. First, an introduction, we elaborate the rheology model based on postseismic deformation due to the 2012 Indian Ocean earthquake from several previous studies. Second, based on previous studies, we develop the model and find several phenomena that could determine the unresolved problem in previous published postseismic deformation analysis.

6.1 Introduction

After the 2012 Indian Ocean earthquake, several studies tried to explain postseismic deformation with the assumption of rheology model of oceanic asthenosphere in a priori. The exploration of asthenospheric viscosity layer using the postseismic deformation of the Indian Ocean earthquake has been done by Han et al. (2015), Hu et al. (2016) and Masuti et al. (2016). These previous analyses obtained different values for the viscosity of the asthenosphere that may have arisen from the complex geometries and different modeling assumptions. Following are the brief summary of postseismic analysis based on previous studies.

6.1.1 Han et al. (2015)

Han et al. (2015) used Gravity Recovery and Climate Experiment (GRACE) data to estimate viscosity structure in the oceanic asthenosphere. Monthly time series of GRACE solutions documented the gravity change before, during and after the 2012 Indian Ocean earthquake. Similar to GNSS data, in order to obtain postseismic deformation due to the 2012 Indian Ocean earthquake, they removed the signal that is not associated with the 2012 Indian Ocean earthquake by fitting sinusoidal function due to seasonal variation of climate and ocean tide, and logarithmic function due to postseismic deformation of the 2004 Sumatra-Andaman earthquake. In Figure 6.1, black and gray lines are gravity change and model fitting, respectively. Meanwhile, the red line represents gravity change after the 2012 Indian Ocean earthquake. Based on the red line component, the uplift and subsidence are observed clearly after the 2012 Indian Ocean earthquake, respectively (Figure 6.1). The postseismic uplift at the compressional regions consistent with the observed GNSS data in the northern Sumatra.

To calculate the displacement and gravity changes at the surface due to the viscoelastic relaxation response, Han et al. (2015) used a spherical viscoelastic model from VISCO1D (Pollitz, 1997). VISCO1D are widely used for analyzing viscoelastic relaxation due to a megathrust or inland earthquake (Panet et al., 2010; Pollitz et al., 2001; Pollitz et al., 2017). VISCO1D assumed a spherically stratified viscoelastic Earth layer that neglects the effect of the subducted elastic slab.

Coseismic fault model of Wei et al. (2013) was applied to calculate coseismic stress change. They assumed the lithosphere and asthenosphere layers are 60 km and 160 km, respectively. The rest of the model is upper mantle and lower mantle, which assumed to be Maxwell 1×10^{20} Pa s and 1×10^{21} Pa s, respectively. Han et al. (2015) tested only five different oceanic asthenosphere viscosities, that is the Maxwell viscosity of 5×10^{17} Pa s, 1×10^{18} Pa s, 5×10^{18} Pa s, 1×10^{19} Pa s and Burgers rheology with the Kelvin viscosity of 1×10^{18} Pa s and the Maxwell viscosity of 1×10^{19} Pa s. The afterslip was assumed to cause a minor deformation that could be omitted. Han et al. (2015) preferred Burgers rheology to explain two-years gravity change due to the 2012 Indian Ocean postseismic deformation.

6.1.2 Hu et al. (2016)

One year after Han et al.'s (2015) study, Hu et al. (2016) and Masuti et al. (2016) published rheology models based on the postseismic deformation of the 2012 Indian Ocean earthquake.

Hu et al. (2016) constrained their rheology model under the Indian Ocean based on three years of mid- and far-field GNSS data using the finite-element method. Wei et al.'s (2013) fault model was used to calculate coseismic stress change. The model incorporates spherical earth and 3-D elastic slab. The geometry of the oceanic

asthenosphere layer is assumed to subduct with oceanic lithosphere. Also, they assumed in a priori that viscoelastic relaxation in the oceanic asthenosphere follows Maxwell rheology model. On the other hand, the viscoelastic upper mantle is assumed to follow the burgers rheology model in which the Kelvin viscosity was assumed to be one order of magnitude lower than the Maxwell viscosity. The schematic representation of the finite-element model is shown in Figure 6.2.

Exploration of the model space has been done in Hu et al. (2016) study. For example, if the oceanic asthenosphere has the same viscosity as oceanic upper mantle, a viscosity of 1×10^{20} Pa s or 1×10^{19} Pa s (homogeneous oceanic upper mantle) could produce landward horizontal component but produce postseismic subsidence in the fore-arc GNSS site implying that a weak oceanic asthenosphere is needed to generate the observed uplift. Afterslip also has been tested using a weak shear zone approach (Hearn et al., 2002) in which they put additional viscous material within fault plane using very low viscosity. However, the tested afterslip model has failed to decrease the model misfits. As a result, they excluded the afterslip in further analysis.

The model of Hu et al. (2016) tried to estimate viscosity of the oceanic upper mantle, viscosity and thickness of the oceanic asthenosphere. Several parameters such as the homogeneous layered rigidity, the viscosity of the continental upper mantle and the thickness of the oceanic and the continental lithosphere are fixed (Figure 6.2). Based on a grid search method, they found a preferred model that consists of the Maxwell viscosity of 2×10^{18} Pa s for the oceanic asthenosphere, Kelvin viscosity of 1×10^{19} Pa s with the Maxwell viscosity of 1×10^{20} Pa s of oceanic upper mantle, and 80 km thickness of the subducted asthenosphere layer (Figure 6.2).

The preferred model predicted a general trend of deformation, which is postseismic landward motion and uplift in the fore-arc region (Figure 6.3). However,

the calculated direction of horizontal velocities of middle field GNSS data in the fore-arc region tends to be rotated clockwise from the observation by 10-20 degrees. Also, the vertical component of the model could not fit the observed uplift very well.

6.1.3 Masuti et al. (2016)

Another model of the postseismic deformation due to the 2012 Indian Ocean earthquake was proposed by Masuti et al. (2016). This model explored the sensitivity of water content (it is not a normal liquid water under high pressure/temperature condition but the water act as impurities in the mineral) on the strength of mantle olivine. They assumed a priori that the oceanic asthenosphere follows power-law viscosity reflecting thermally activated flow law of rock investigated by laboratory experiments (Bürgmann and Dresen, 2008; Karato and Wu, 1993; Karato and Jung, 2003). Unlike the linear Maxwell or Burgers rheology, power law viscosity is non-linear. The range of each parameter in power-law rheology remains poorly understood. Hence, Masuti et al. (2016) investigated the effect of the water content and mantle temperatures of the oceanic asthenosphere.

The model of Masuti et al. (2016) also assumed coseismic stress change calculated from the mainshock Mw 8.6 and largest aftershock Mw 8.2 based on Wei et al. (2013) to produce the viscous flow of the oceanic asthenosphere and triggered afterslip around the fault. The model also assumed the thickness of the purely elastic oceanic lithosphere of 80 km (Figure 6.4). Semi-analytic code known as Relax from CIG (https://geodynamics.org/cig/software/relax/) was used to simulate viscoelastic relaxation and afterslip.

Masuti et al. (2016) analyzed the postseismic deformation based on one-year GNSS postseismic motion mostly in the fore-arc area (Figure 6.5). The model

estimated the water content of 0.01 percent by weight or 1600 H/Si ppm in the oceanic asthenosphere implying weak asthenosphere in which the water content drastically reduces the strength of the olivine. Based on power-law viscoelastic relaxation and afterslip processes, the model could satisfactorily fit the rapid transient of the horizontal component within one-year GNSS postseismic motion in the fore-arc region (Figure 6.5) but was poorly explained the rapid transient motion in the vertical component. Although the model underestimates the vertical observation, the horizontal components nearly fit the azimuth of the observation in the fore arc (Figure 6.6). However, the GNSS site in the northern Sumatra is clearly overestimated (Figure 6.5). The model parameters would be sensitive if we include additional data in the most northern Sumatra.

6.2 Afterslip model

Afterslip distribution is widely inferred for postseismic deformation using geodetic inversion (e.g Gunawan et al., 2014; Yamagiwa et al., 2015). However, our geodetic network was limited, sparse, and far from the source; thus, we refrained from inferring the afterslip distribution using geodetic inversion. As our aim is to calculate the surface displacement resulting from afterslip at each GNSS station, we simulated the afterslip based on coseismic stress change. The simulation uses the static stress changes associated with the given coseismic model in a simulation of afterslip governed by a static friction law (Aagaard et al., 2013a). Fault surface static stress change due to the calculated afterslip cancels static stress increment due to the coseismic slip. In that sense, the afterslip occurs where the coseismic slip increases the shear tractions. Since this calculation is based on static force balance in order to estimate spatial variation of the afterslip, we additionally need to estimate afterslip

time variation. Therefore, we modeled the afterslip time evolution by an analytical temporal decay function fitting as demonstrated in previous studies (Hu and Wang, 2012; Ohta et al., 2008; Suito and Freymueller, 2009).

There are two main alternatives to modeled time evolution of afterslip, which is widely considered: logarithmic and exponential form (e.g. Anugrah et al., 2015; Kreemer et al., 2006). However, as suggested by previous studies (e.g. Ardika et al., 2015; Kreemer et al., 2006), postseismic motion with dominant afterslip was well explained by a logarithmic function than an exponential function. Hence, we modeled the time evolution of afterslip using a logarithmic function as follows

$$u(t)_n = A_n \, ln\left(1 + {}^{t}/_{\tau_{as}}\right) \tag{13}$$

where *u(t)* and τ_{as} are the surface displacement with spatial-temporal variation and the decay time of afterslip, respectively. Index *n* represents each GNSS site. The constant *A* is the normalized calculated static surface displacement (depends on the position) with normalization factor e by multiply *A* with $1/e$, where e is the Euler's number. The normalization factor is to ensure that the total afterslip represents slips from the event until fully relaxed.

The calculated stress-driven afterslip produced subsidence at the GNSS sites in northern Sumatra (shown in Figure 6.12). This subsidence has a similar sense to those of the observed coseismic offsets of the GNSS sites. As we fitted the time evolution of afterslip with a logarithmic function (2), we obtained a decay time due to the afterslip at approximately 9.83 days. The estimated decay time indicated that aseismic slip duration due to the afterslip was short. This value is plausible compared to various earthquake case studies (Ardika et al., 2015; Freed, 2007; Kreemer et al.,

2006), which obtained the decay time after earthquake occurrences less than ten days. Most of those previous studies are for continental region because we cannot find any afterslip example of an oceanic intraplate earthquake in previous studies.

The coseismic fault model indicates that the largest seismic moment was released at the shallow portion of the fault (Figure 6.7a). Since we calculate the afterslip spatial distribution based on the coseismic shear stress change, the afterslip is calculated to occur on the surrounding region of the coseismic slip (Figure 6.7b). In order to evaluate the deeper afterslip distribution, we tested several oceanic lithosphere thicknesses and obtained negligible afterslip effect at our GNSS site for the thickness over 60 km. In that sense, in the rest of the study, we fix this estimated surface displacement resulting from afterslip.

6.3 Transient Rheology of the Oceanic Asthenosphere

6.3.1 Introduction

In this study, the main purpose is to reveal transient rheology structure under the Indian Ocean due to the 2012 Indian Ocean earthquake. Our model geometry is same as described in chapter 4 in which sphericity of the earth, slab and heterogeneous rigidity included. Based on our analysis in chapter 5, the coseismic fault model from Hill et al. (2015) is used to calculate coseismic stress change.

We reduce the unknown parameters in our model due to computation limit. Therefore, we assumed several parameters based on previous studies. First, we fixed the elastic thickness of the continental side at 65 km as suggested by geodetic (Gunawan et al., 2014) and seismic studies (Wu et al., 2004). Second, we assumed the continental asthenosphere rheology as Maxwell body with a viscosity of 9×10^{18} Pa s,

a common value for various subduction zones (Gunawan et al., 2014; Wang, 2007). Also, we fix 10^{20} Pa s for both oceanic and continental upper mantle viscosity below the asthenosphere (King, 1995). The summary of the fixed parameters shown in Figure 6.8.

In order to estimate the rheology model, we used a grid search algorithm. To obtain a more efficient grid search algorithm, we initially searched within a wide, coarse grid for model parameters, subsequently using a finer grid after obtaining the minimum residual. We examined three parameters, the thickness of the oceanic lithosphere layer and the oceanic asthenosphere viscosity with both Kelvin and Maxwell viscosities, to obtain the minimum chi-squared χ^2. The chi-squared misfit between the observations and the combined rheology model is as follows:

$$\chi^2 = \sum_{n=1}^{N} \sum_{i=1}^{3} \sum_{t=1}^{T} \frac{\left(Obs_{n,i,t} - Cal_{vis\,n,i,t} - Cal_{afs\,n,i,t}\right)^2}{{\sigma_{n,i,t}}^2} \tag{14}$$

where *Obs*, Cal_{vis}, and Cal_{afs} are the observed GNSS displacement, calculated viscoelastic model, and calculated afterslip model, respectively. The indices *n*, *i*, and *t* represent the GNSS site, the directional component of crustal deformation, and the time step, respectively. N and T are the total GNSS sites and total time steps, respectively, and σ^2 denotes the variance of the GNSS observation for each time step. In order to obtain the same contribution both horizontally and vertically, we calculated the misfit value using equal combinations of horizontal and vertical component misfits.

6.3.2 Model 1: Maxwell Rheology

First, we start the model using uni-viscous Maxwell rheology (Figure 6.9). Due to computation limit, we assume the lower and upper bound Maxwell viscosity for the grid search based on previous studies (Hu et al., 2016; Pollitz et al., 1998). On the other hand, we assume the lower and upper bound thickness for the oceanic lithosphere from the thinner assumption of 50 km (Hu et al., 2016) to the thicker assumption of 80 km (Masuti et al., 2016). We calculate viscoelastic models based on grid search method from 1×10^{17} Pa s to 1×10^{20} Pa s combined with the oceanic lithosphere thickness from 50 km to 80 km. The grid interval for the thickness in all cases is 5 km. We obtained the minimum misfit 340.26. The minimum misfit has the optimum viscosity and oceanic lithosphere thickness are 5×10^{17} Pa s and 70 km, respectively. Based on the optimum model, we show the observation and model deformation for two years (Figure 6.10). We show six sites only in Figure 6.10 and show the other GNSS sites in Appendix B.

Maxwell rheology on oceanic asthenosphere could produce a general trend that is horizontal landward motion and uplift. However, the model failed to explain the rapid transient deformation in our GNSS site from two to six months after the mainshocks. Thus, we point out the necessity of transient rheology model to reproduce transient deformation.

6.3.3 Model 2: Burgers Rheology

As the second model, we use Burgers rheology to represent transient rheology (Figure 6.11). We assume the lower and upper bound Maxwell viscosity and thickness for the grid search same as the previous model. Meanwhile, we assume the lower and upper bound for the Kelvin viscosity one order lower of the Maxwell viscosity (Wang

et al., 2012). We calculate viscoelastic model based on grid search for Oceanic asthenosphere viscosity consist of Kelvin from 1×10^{16} Pa s to 1×10^{19} Pa s, Maxwell from 1×10^{17} Pa s to 1×10^{20} Pa s and oceanic lithosphere thickness from 50 km to 80 km. We obtained the minimum misfit 206.61. We obtained the optimum model that consists of Kelvin viscosity of 5×10^{16} Pa s, Maxwell viscosity of 1×10^{18} Pa s and 75 km for the oceanic lithosphere thickness (Figure 6.12). Figure 6.13 shows the observation and model deformation for two years using the optimum model. We show six sites only in Figure 6.13 and show the other GNSS site in Appendix B.

Our results using Burgers rheology model could explain the transient deformation during the first six months after the earthquake. The optimized model also explains the uplift, but we still have too large uplift for ACEH and LEWK sites after one year from the mainshock, which corresponds to Maxwell viscosity. A higher Maxwell viscosity would lead to underestimating horizontal landward motion. Since the afterslip deformation caused landward horizontal surface deformation and slightly vertical subsidence, we speculate that afterslip is responsible to decrease vertical uplift at ACEH and LEWK sites. Hence, we need additional afterslip to expect lower uplift.

6.3.4 Model 3: Burgers Rheology and afterslip

The Third model, we use Burgers rheology model as Model 2 in the previous explanation and afterslip model that has been modeled in the previous sub-chapter. The minimum misfit for the combined viscoelastic model and afterslip model are 129.32 shown in Figure 6.14. Based on the grid search results, we obtained an optimum rheology model of 75 km thickness for the oceanic lithosphere, asthenosphere Kelvin viscosity of 1×10^{17} Pa s, and Maxwell viscosity of 3×10^{18} Pa

s (Figure 6.14). Although the afterslip model exhibited slight subsidence in the vertical component, which is the opposite sense to the observed postseismic uplift, the misfit value was 37% smaller when including the afterslip model compared to excluding the afterslip model. Figure 6.15 shows the six sites of observation and model deformation for two years using the optimum model, and the other GNSS sites are shown in Appendix B.

We evaluate the robustness of our result. For this purpose, we calculate optimum model by applying grid search to minimize chi-square misfit value for six different cases. Each case has one site to be removed from the misfit calculation. Therefore, we obtained the optimum model based on each case in Table 6.1. The Kelvin and Maxwell viscosity has a maximum difference about 1×10^{17} Pa s and 1×10^{18} Pa s., respectively. Meanwhile, the oceanic lithosphere thickness has a maximum difference of about 5 km. We concluded that our rheology result is robust.

Our third model, which is a combined model of viscoelastic relaxation and afterslip model, could explain horizontal and vertical components of GNSS data in Northern Sumatra (Figure 6.15, Figure 6.16). The afterslip affects in a way that the Kelvin viscosity gets higher by a half order, slightly changes the Maxwell viscosity, and increase oceanic lithosphere thickness than model 2. We also obtained that the smallest misfit is the model 3 (129.32) between model 2 (206.61) and model 1 (340.26). Hence, the last model is the best model among the tested model.

6.3.5 The Goodness of Fit

The obtained best-fit model for model 1, model 2 and model 3 has chi-square misfit 340.26, 206.61 and 129.32, respectively. We perform a chi-square statistical test using a probability value assumption within the chi-square distribution table

(Appendix C). The chi-squared test gives the reason that the fit is a likely to be achieved. We assume a 5% probability of value with the degree of freedom *(dof)* based on the number of data minus the number of estimated parameter in the model. The number of data is 216 obtained from 9 sites with equally time step for each 3 months during two years postseismic period (start from the first month). Therefore, the degree of freedom of model 1, model 2, and model 3 are 214, 213, 212, respectively. Based on the chi-square distribution table (Appendix C) and its degree of freedom, model 1, model 2 and model 3 has critical value 249.128, 248.048, 246.968, respectively. Since the chi-square misfit of the best-fit model 2 and 3 is less than the critical value, we can conclude that the best-fit model 2 and 3 is acceptable. This test indicated that bi-viscous transient and steady-state rheology (model 2 and 3) is better than uni-viscous steady state rheology to explain the postseismic deformation following the 2012 Indian Ocean earthquake.

6.3.6 Conclusion

We obtained the optimum model of oceanic mantle rheology consisting of the oceanic asthenosphere with the Kelvin viscosity and the Maxwell viscosity of 1×10^{17} Pa s and 3×10^{18} Pa s, respectively. Also, we obtained the oceanic thickness lithosphere of 75 km, which is thicker than previous studies assumption (Han et al. 2015, Hu et al. 2016) and thinner than other studies (Masuti et al. 2016). We demonstrated that large temporal change of viscosity is required to explain transient deformation in the first six months of the early postseismic deformation.

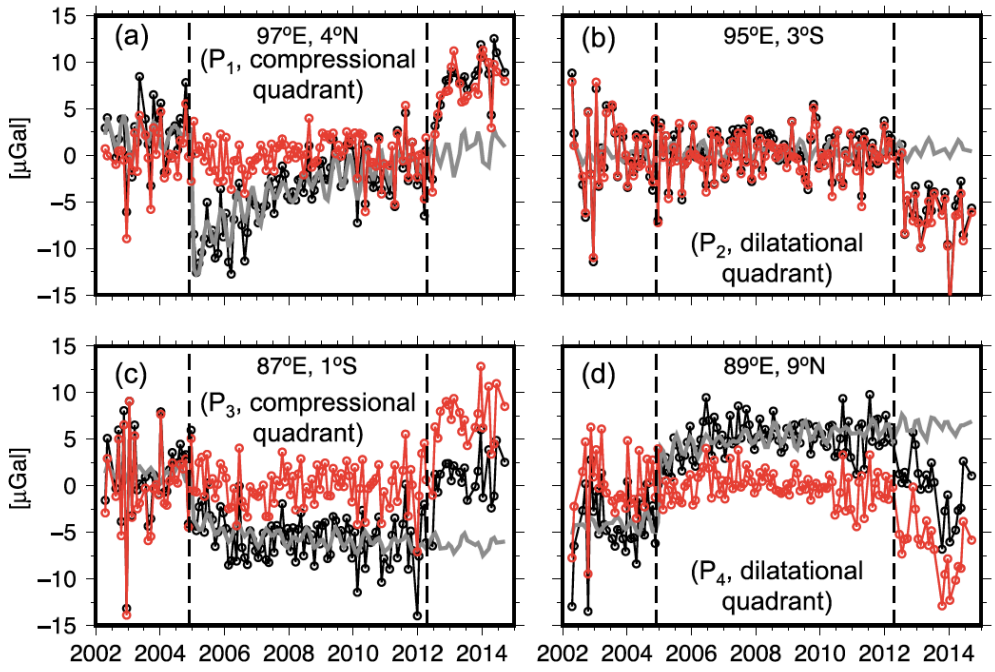

Figure 6.1 Time series of GRAVITY change from 2002 until 2014 at the center of compressional and dilatational region (Same as Figure 2 of Han et al. (2015)).

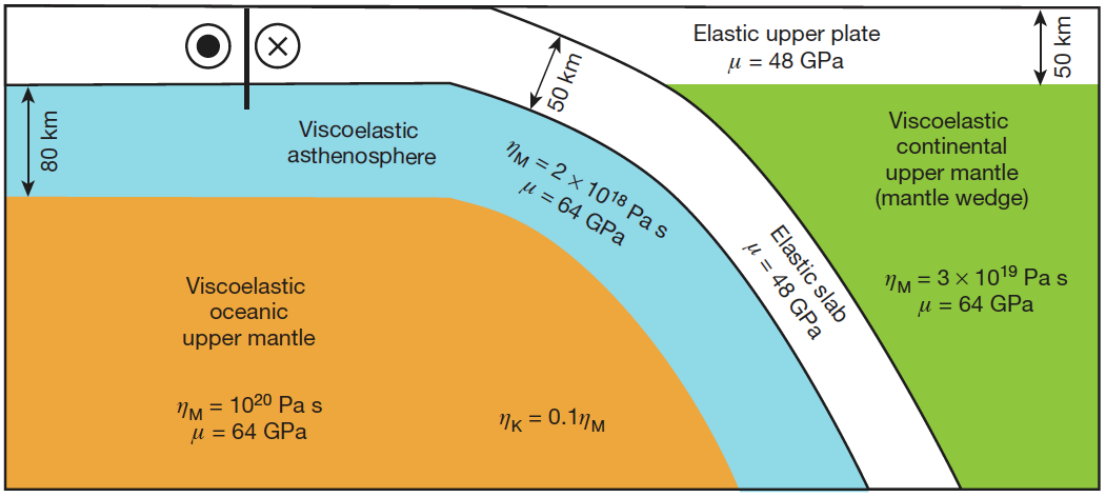

Figure 6.2 Schematic representation of Hu et al. (2016) rheology model. (Same as Figure 2 of Hu et al. (2016))

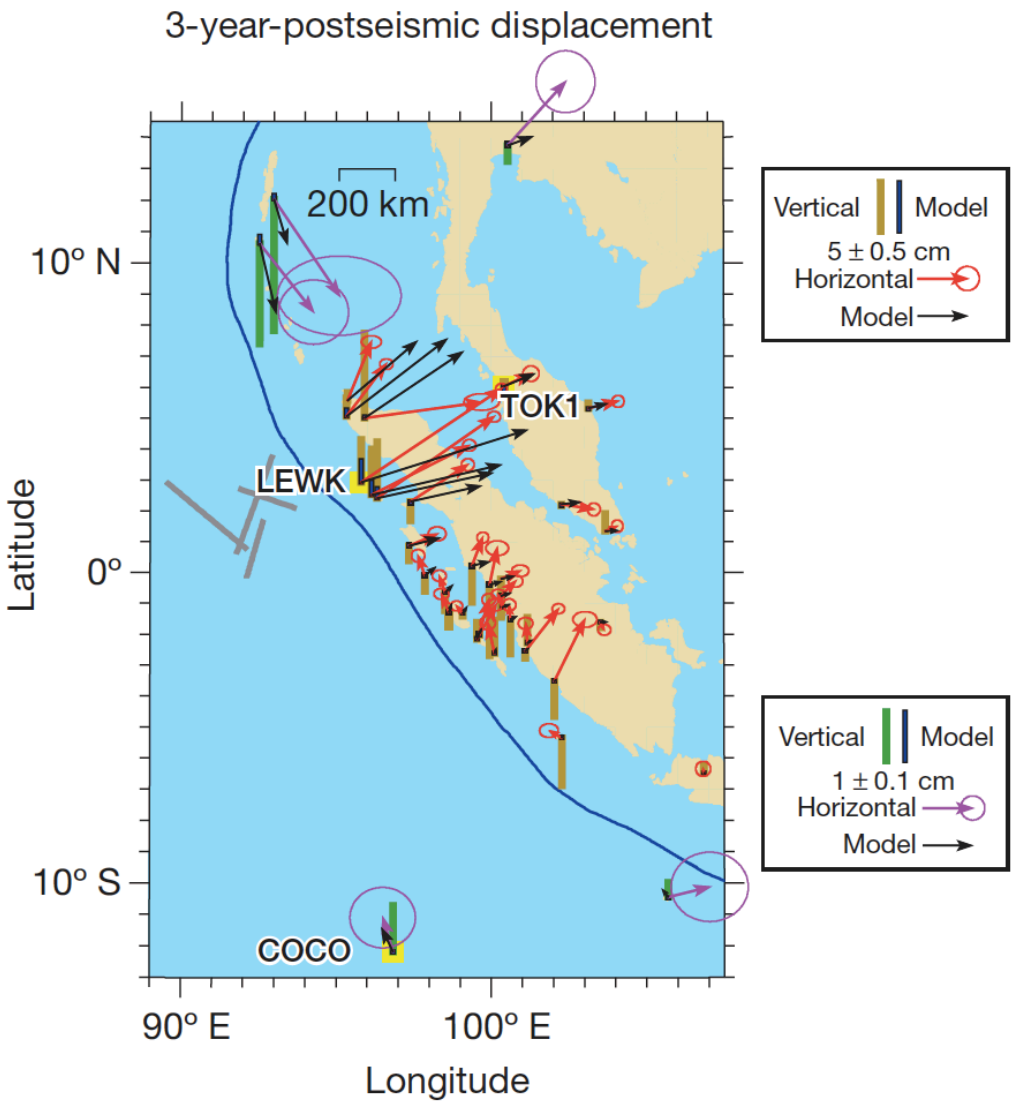

Figure 6.3 Preferred model and three-years postseismic displacement of Hu et al. (2016) study. (Same as Figure 5 of Hu et al. (2016))

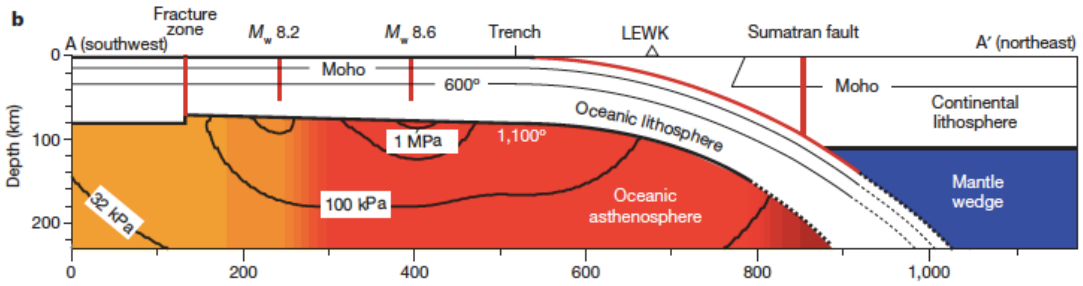

Figure 6.4 Conceptual representation of Masuti et al. (2016) model. (Same as Figure 1b of Masuti et al. (2016))

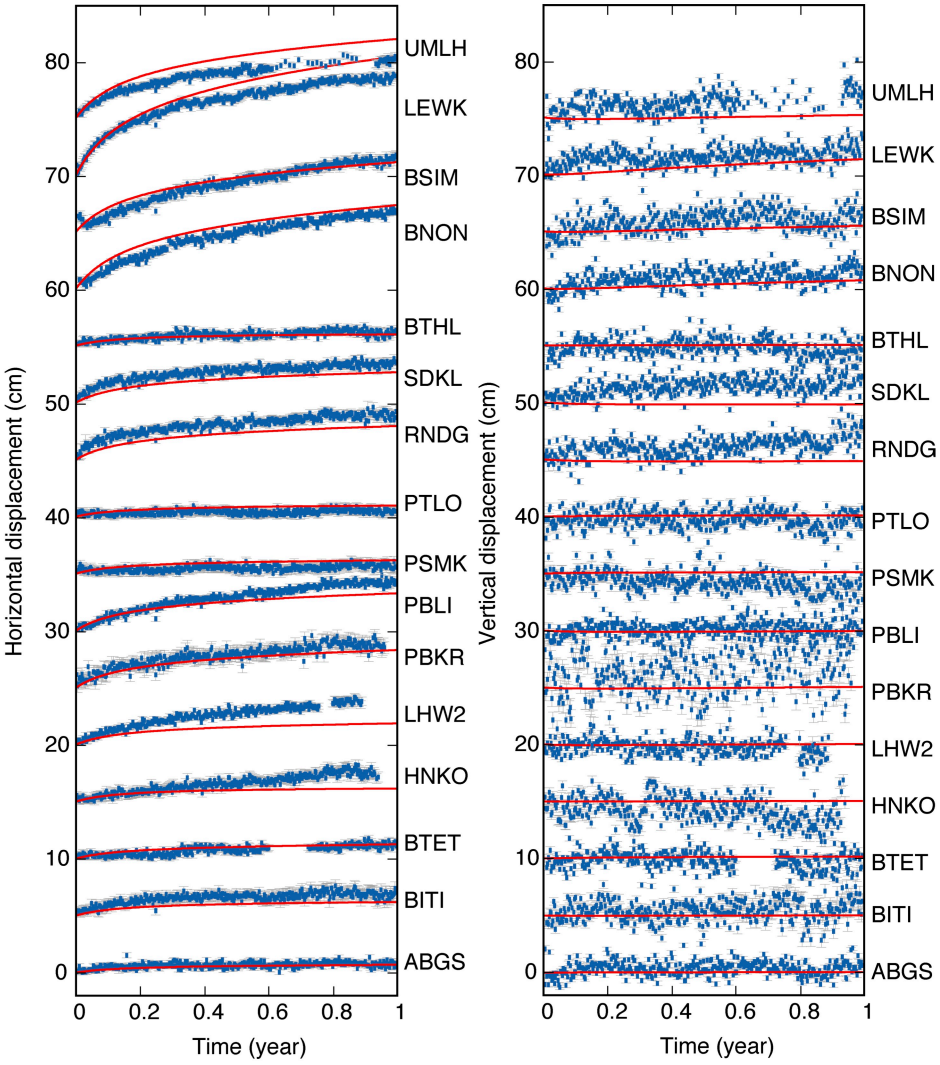

Figure 6.5 Observed (blue squares with uncertainty) and modeled (red profiles) temporal variation of deformation during one year postseismic deformation. (Same as Extended Data Figure 7 of Masuti et al. (2016))

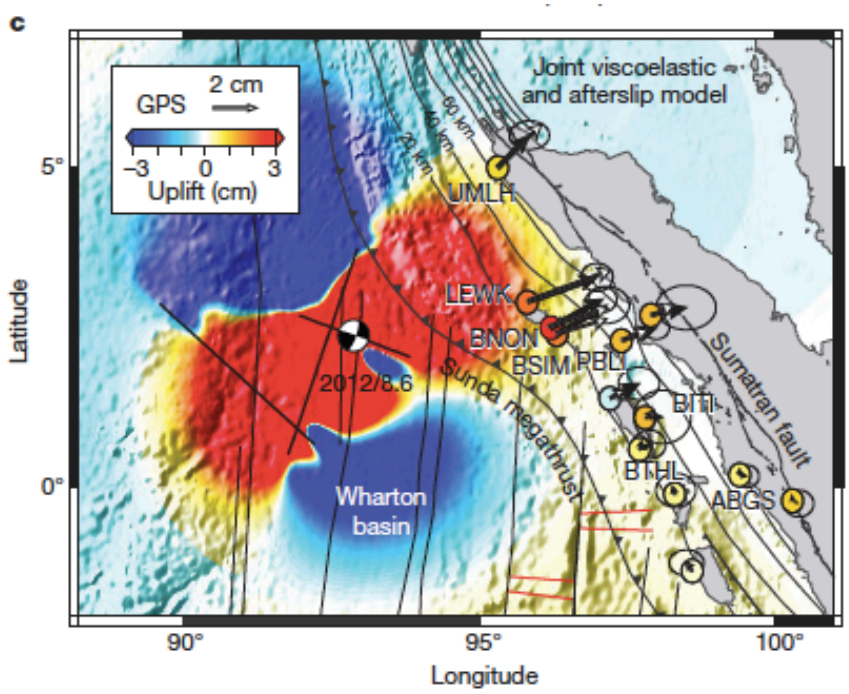

Figure 6.6 Observed and modeled spatial variation of deformation during one year postseismic deformation. (Same as Figure 2c of Masuti et al. (2016))

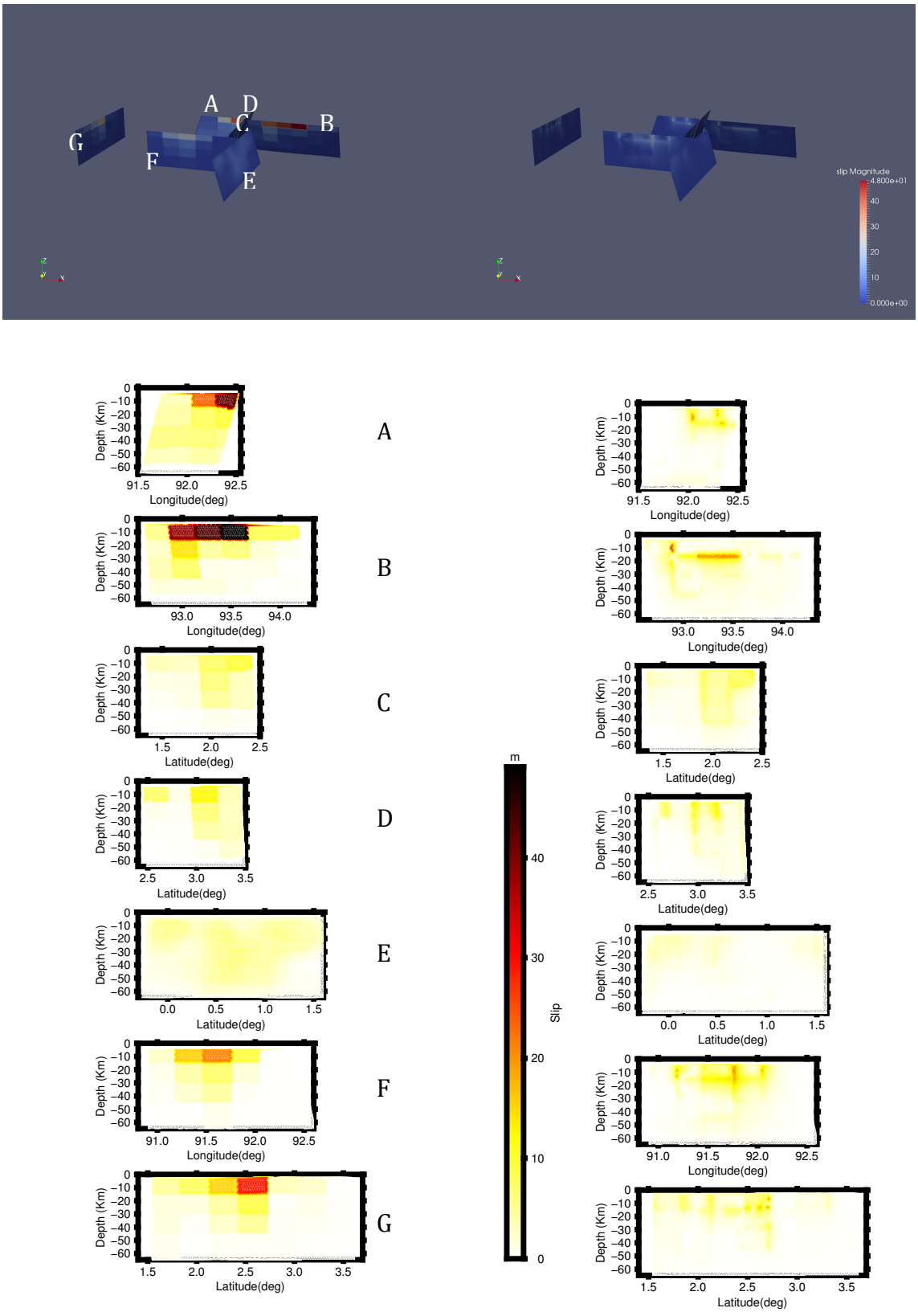

Figure 6.7 X, y, and z axes represent E-W, N-S and U-D direction, respectively. Slip scaled from 0 – 48 meter for both coseismic and afterslip. The 3-D and 2-D view of (a) coseismic slip and (b) afterslip distribution that utilized in this study.

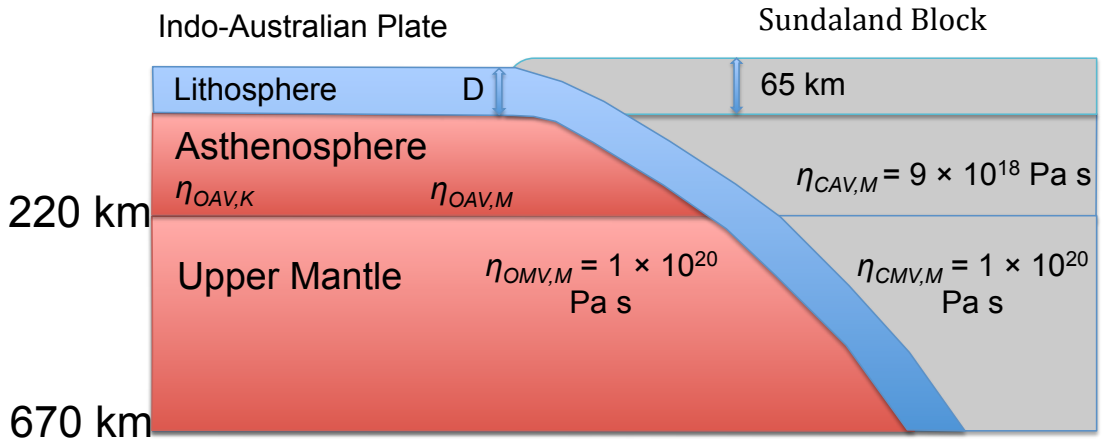

Figure 6.8 Model configuration in this study. Blue color indicates oceanic lithosphere with thickness D. Meanwhile, red colors indicates oceanic upper mantle including asthenosphere layer. Grey color indicates continental side with 65 km lithosphere thickness and 155 km asthenosphere thickness. The depth of our model is 670 km. We abbreviated the estimated viscosity parameter $\eta_{OAV,K}$ and $\eta_{OAV,M}$ as oceanic asthenosphere Kelvin and Maxwell viscosity, respectively. Meanwhile $\eta_{OMV,M}$, $\eta_{CMV,M}$and $\eta_{CAV,M}$ indicate oceanic upper mantle, continental upper mantle and continental asthenosphere viscosity with Maxwell model.

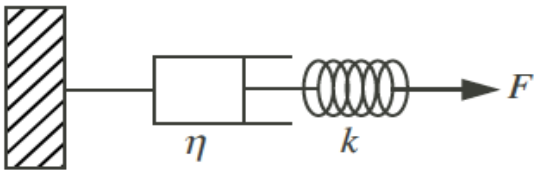

Figure 6.9 Maxwell model representation of dashpot and spring combination where *F, k,* and η are force, elastic constant and viscosity.

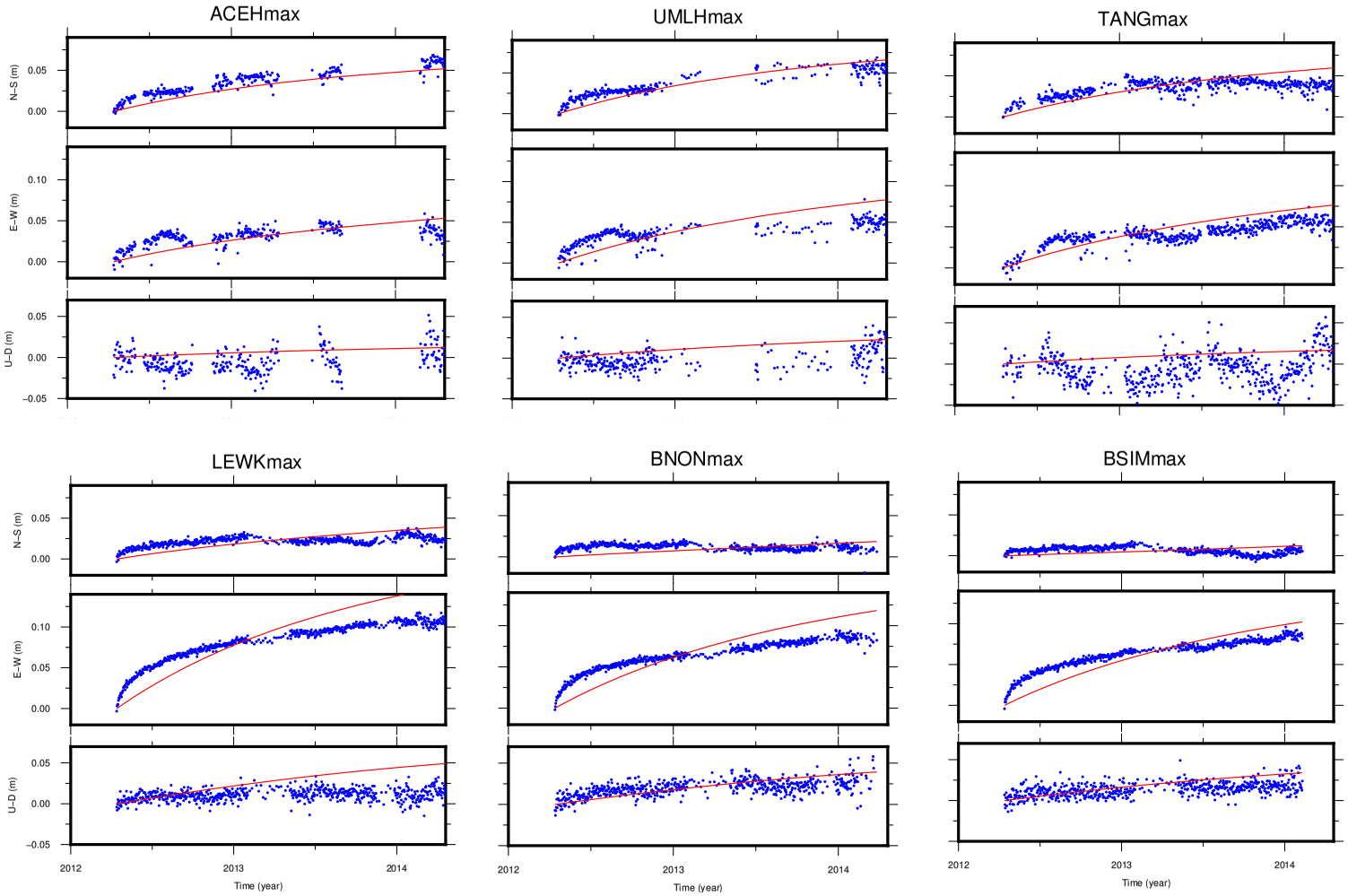

Figure 6.10 Observation and model deformation for two-years. Blue dot and red line denotes observation and model, respectively.

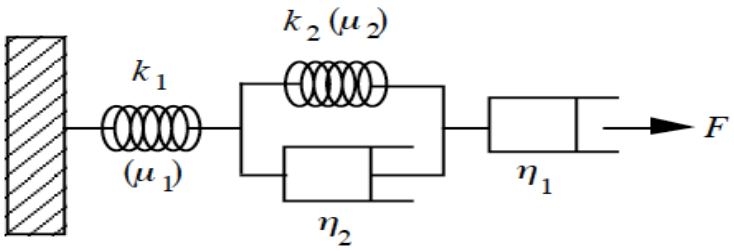

Figure 6.11 Burgers model representation of dashpot and spring combination where *F*, *k*, and η are force, elastic constant and viscosity.

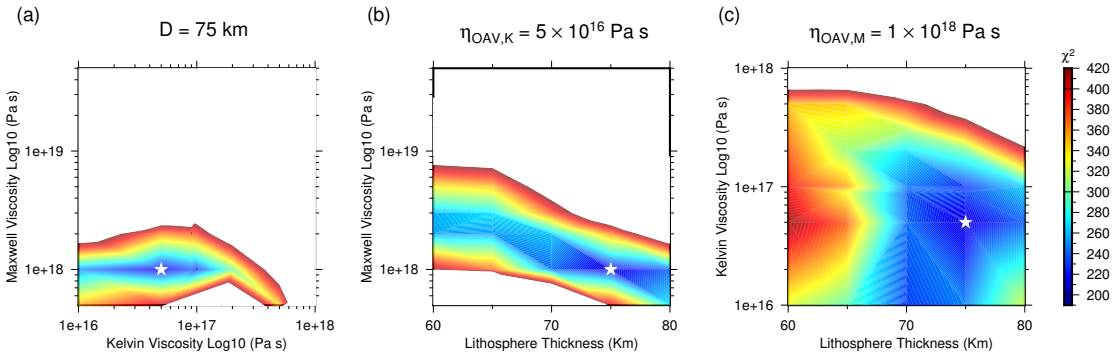

Figure 6.12 χ^2 distribution for each parameter. (a) Trade off between Kelvin viscosity and Maxwell viscosity at D = 75 km, (b) Maxwell viscosity and lithosphere thickness at $\eta_{OAV,K}$ = 5 × 10¹⁶ Pa s, (c) Kelvin viscosity and lithosphere thickness at $\eta_{OAV,M}$ = 1 × 10¹⁸ Pa s. White star indicates optimum rheology model.

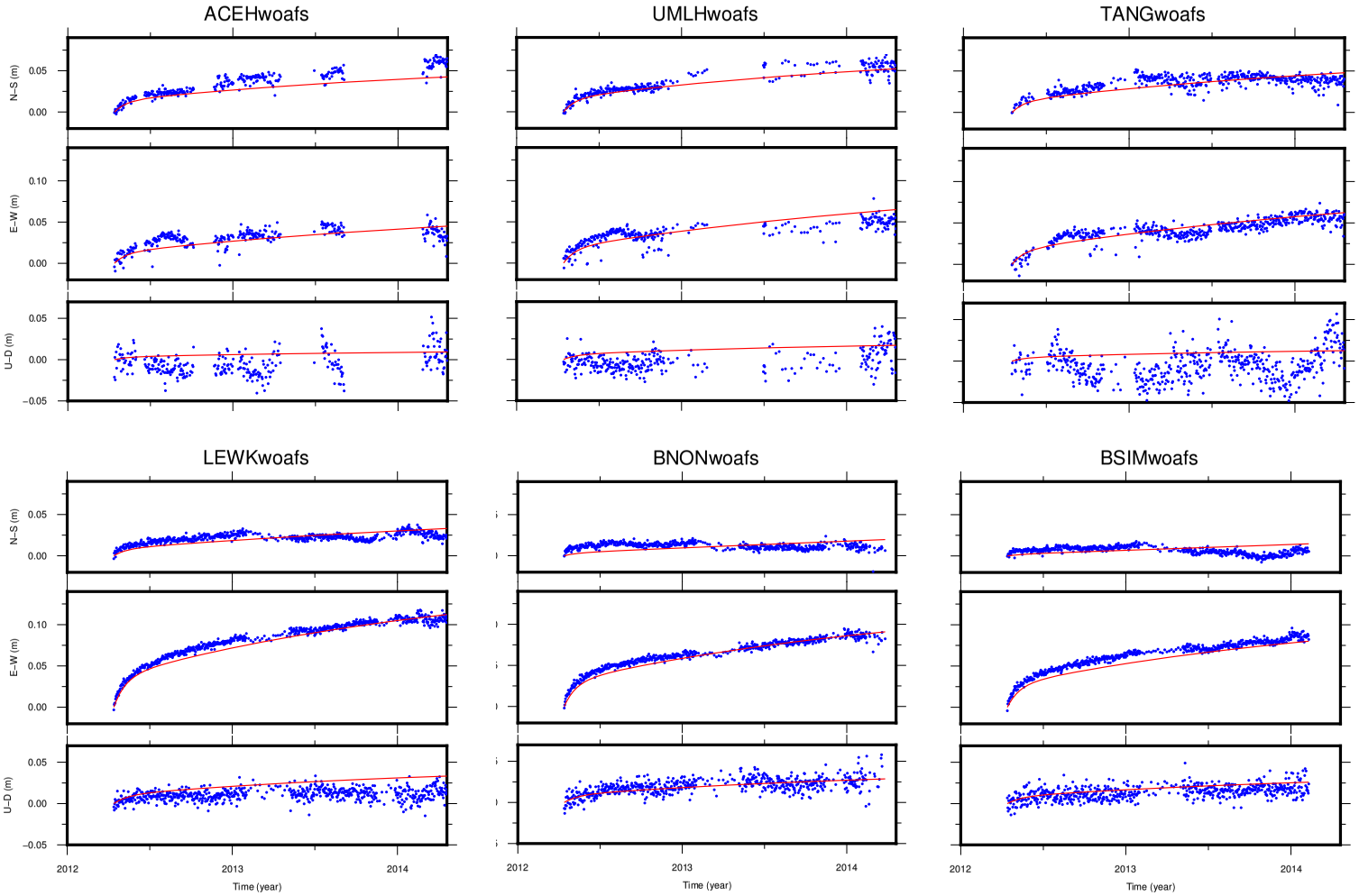

Figure 6.13 Observation and model deformation for two-years. Blue dot and red line denotes observation and model, respectively

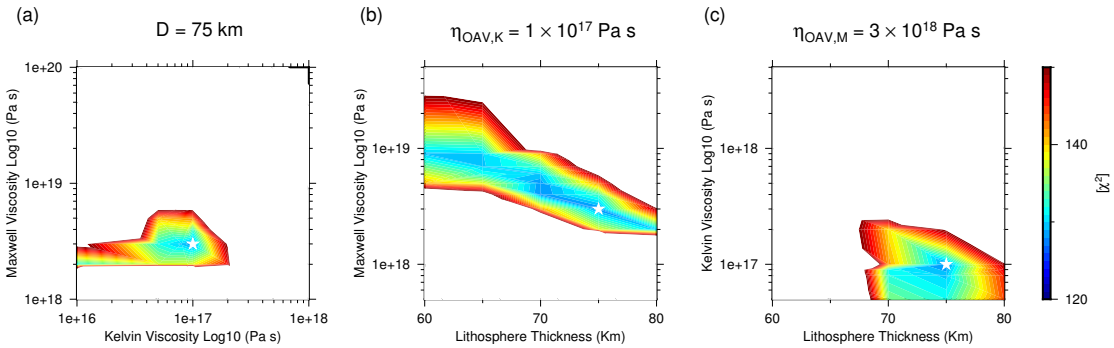

Figure 6.14 χ^2 distribution for each parameter. (a) Trade off between Maxwell viscosity and Kelvin viscosity at D = 75 km, (b) Maxwell viscosity and lithosphere thickness at $\eta_{OAV,K}$ = 1 × 10¹⁷ Pa s, (c) Kelvin viscosity and lithosphere thickness at $\eta_{OAV,M}$ = 3 × 10¹⁸ Pa s. White star indicates optimum rheology model.

\

Table 6.1 Robustness test based on our GNSS data

Removed site	Optimum Model		
	Kelvin Viscosity (Pa s)	Maxwell Viscosity (Pa s)	Oceanic Lithosphere Thickness (km)
None	1×10^{17}	3×10^{18}	75
Fore-arc* + ACEH	1×10^{17}	3×10^{18}	70
Fore-arc* + UMLH	9×10^{16}	2×10^{18}	70
Fore-arc*+ TANG	1×10^{17}	3×10^{18}	70
Fore-arc* + UGDN	1×10^{17}	3×10^{18}	65
Fore-arc* + MANE	2×10^{17}	2×10^{18}	70
Fore-arc*	1×10^{17}	2×10^{18}	75

*Fore-arc sites: LEWK, BSIM, BNON, PBLI

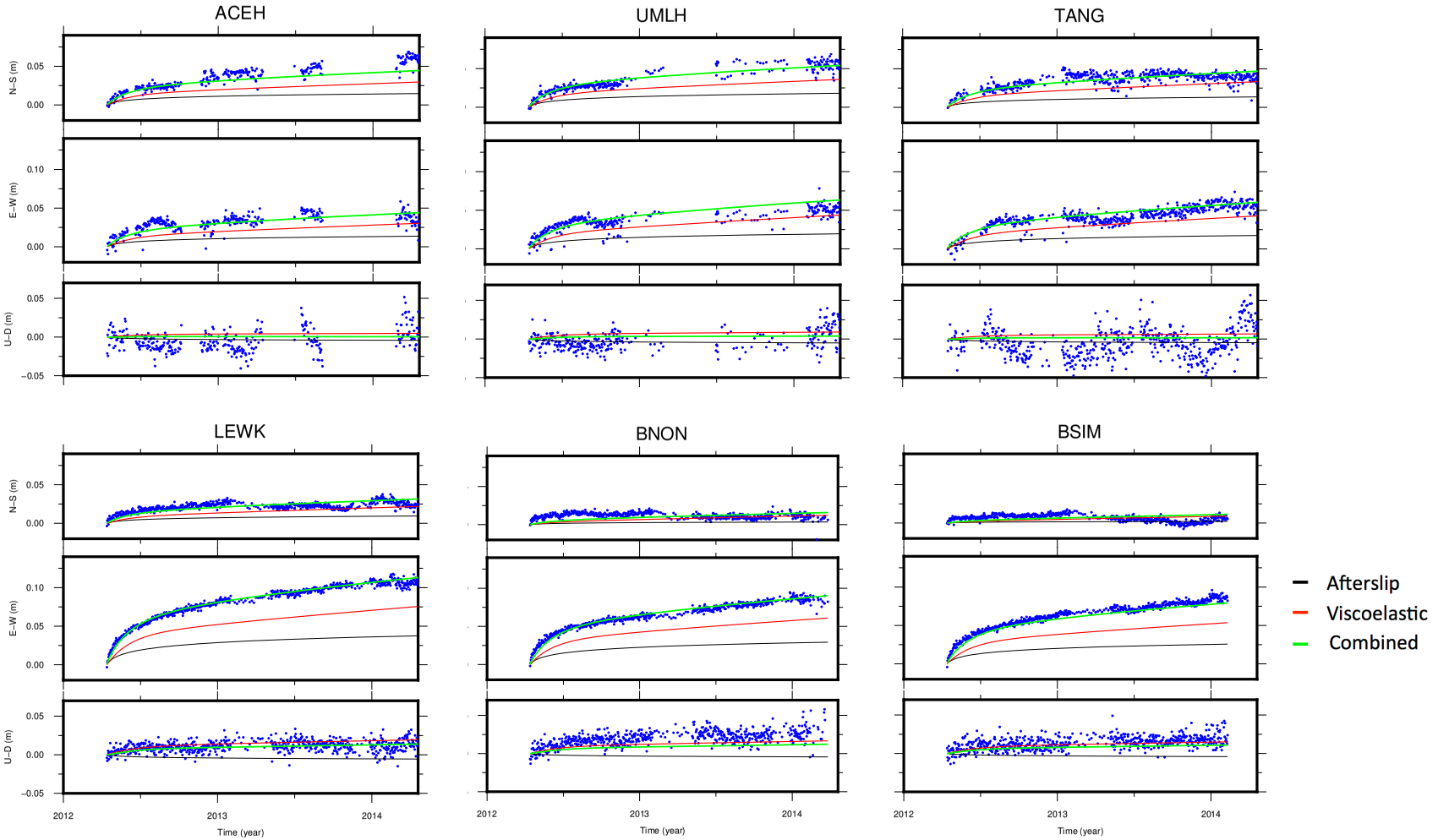

Figure 6.15 Observation and model deformation for two-years. Blue dot, red, black and green line denotes observation, viscoelastic, afterslip and combined model, respectively.

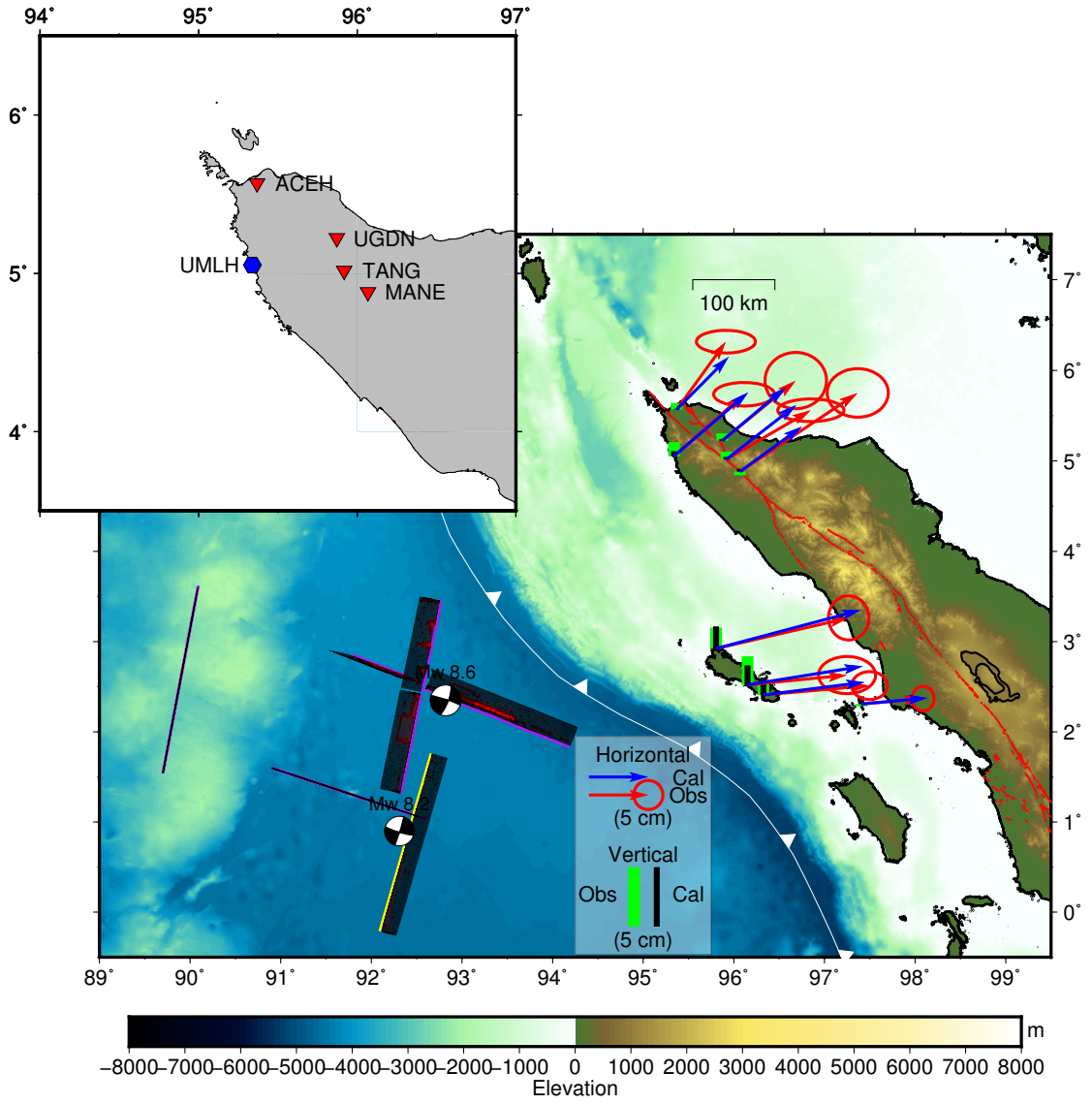

Figure 6.16 Combined viscoelastic relaxation and afterslip model compare with two-years GNSS displacement in the Northern Sumatra. Red and blue arrows indicate horizontal surface displacement for postseismic observation and model, respectively. While green and black bars denotes vertical surface displacement for observation and model, respectively.

7 Discussion and Conclusion

7.1 Discussion

7.1.1 The Best-fit model

The estimated viscosity results are almost one order of magnitude lower than those of Han et al. (2015), who obtained values of 1×10^{19} Pa s for steady-state Maxwell viscosity and 1×10^{18} Pa s for transient Kelvin viscosity. This discrepancy may have arisen from different assumptions of the structural model. The model of Han et al. (2015) used spherical layered earth (Pollitz, 1997), neglecting the effects of the subducted slab, whereas previous studies (Yoshioka and Suzuki, 1999; Pollitz et al., 2008) pointed out that the slab could significantly affect viscoelastic relaxation. We concluded that the effect of the slab significantly reduced the deformation in the fore-arc and back-arc regions (We examine the effect of the elastic slab in chapter 7.1.2). Thus, a lower viscosity value of asthenosphere is required on the model incorporating an elastic slab.

The model of Hu et al. (2016) used a similar finite-element method as the present study; however, several assumptions of that study were completely different, and the aim of the previous studies was to estimate Maxwell viscosity in the oceanic

asthenosphere utilizing middle-field and far-field GNSS data. The main aim of the present study was to estimate the transient viscosity. Since the far-field GNSS dataset does not reflect rapid changes in motion during the early stage of postseismic deformation (Feng et al., 2015; Hu et al., 2016), we focused on constraining the Kelvin viscosity only using the middle-field GNSS dataset for northern Sumatra (Figure 6.11), which exhibits transient motion in the first two months (Figure 6.12). Another different assumption is associated with the asthenosphere layer. The Hu et al.'s (2016) model assumed that the asthenosphere layer subducts with the oceanic lithosphere layer. Based on rock experiments, mantle flow is mainly controlled by pressure- and temperature-dependent viscosity (Karato, 2010). Therefore, a special mechanism is required to explain the low viscosity values below a depth of 300 km in the Hu et al. (2016) model. Thus, instead of a subducted asthenosphere layer, we adopted layered viscosity with the asthenosphere layer terminating at the trench, as assumed by previous studies (Diao et al., 2013, Pollitz et al., 2008). The Hu et al.'s (2016) model yielded a low viscosity of approximately 2×10^{18} Pa s with a thin (80 km) asthenosphere layer. In the present study, the estimated asthenosphere viscosity is 3×10^{18} Pa s, slightly higher than Hu et al. (2016), but with a greater asthenosphere thickness (145 km). This discrepancy probably results from the difference of oceanic asthenosphere geometry and rheology assumptions.

We try to discriminate only the Maxwell body model from the Burgers model; however, the Maxwell model cannot explain the rapid postseismic motion change (Figure 6.8). Consideration of a less complex viscoelastic model with a straight univiscous rheology demonstrates that it reliably underestimates the amplitude of the signal for the first two months. Therefore, the rapid changes in postseismic motion are explained by transient and steady-state rheology.

The model of Masuti et al. (2016) obtained the viscosity based on the assumption of power-law rheology in which the viscosity changes depending on the stress and depth. Assuming dislocation creep, the maximum viscosity is 5×10^{17} Pa s then gradually increase in time. The low viscosity of 5×10^{17} Pa s responsible for the early stage of the postseismic deformation. Our model estimated lower viscosity at the early stage associated with Kelvin viscosity of 1×10^{17} Pa s. Masuti et al.'s (2016) model geometry almost similar to our model except that Masuti et al. (2016) did not incorporate sphericity of the earth. Pratama et al. (2017, AGU) suggest that spherical earth inclusion could affect the viscosity inference to half order lower. Additionally, our model assumes the uniform viscosity for oceanic asthenosphere while Masuti et al.'s (2016) model assume stress and depth-dependent viscosity. Therefore, this discrepancy may arise from the difference of model geometry and rheology model assumptions.

The GNSS vertical component is important in this analysis. As we mentioned in the previous chapter, a higher viscosity of oceanic asthenosphere of 1×10^{20} Pa s produce horizontal landward motion and subsidence (Hu et al., 2016) but a weaker viscosity of oceanic asthenosphere of 1×10^{18} Pa s produce horizontal landward motion and uplift. In the case of GNSS sites in the uppermost of northern Sumatra (AGNeSS network and UMLH site), we only see a postseismic uplift in linear features. We speculate that the afterslip relaxation time is rather similar to Kelvin viscoelasticity. Therefore, during the early stage of postseismic deformation, these two mechanisms canceled each other out, resulting in the Maxwell viscoelasticity controlling the trend of the vertical component. Additionally, in the horizontal component, the afterslip and Kelvin viscoelasticity have a similar direction, which increases the displacement. Hence, coupled afterslip and Kelvin viscoelasticity are

essential to explain linear postseismic uplift in the uppermost of northern Sumatra and rapid change in the horizontal component.

7.1.2 Effect of 3-D elastic slab

As stated in the previous chapter, the estimated viscosity results are almost one order of magnitude lower than those of Han et al. (2015), who obtained values of 1×10^{19} Pa s for steady-state Maxwell viscosity and 1×10^{18} Pa s for transient Kelvin viscosity. That difference is considered as the elastic slab effect. Here, we examine the effect of the elastic slab in our model.

We construct a model that does not include the elastic slab named as Simple Spherical Earth. The model setting is the same as our best-fit model except that we exclude the elastic slab and the viscosity structures become layered structure. The second model is Spherical Earth with a slab. This model is simply attaching the 3-D elastic slab in the Simple Spherical Earth model. In that sense, the model difference is attributed to the existence of elastic slab.

The result of the model calculation shows that the optimum rheology model of Simple Spherical Earth has Kelvin and Maxwell viscosity is 1×10^{17} Pa s and 1×10^{19} Pa s, respectively (Figure 7.1a). However, the Spherical Earth with Slab model has Kelvin and Maxwell viscosity is 7×10^{16} Pa s and 3×10^{18} Pa s, respectively (Figure 7.1b). The Spherical Earth with Slab model has one order lower Maxwell viscosity than Simple Spherical Earth model. That indicates the elastic slab affect significant one order difference Maxwell viscosity, which is consistent with the difference between Han et al. (2015) and the best-fit model in this study.

7.1.3 Rheological structure

We estimated a rheology model consisting of oceanic lithosphere thickness and asthenosphere viscosity with bi-viscous Burgers body rheology. Lithosphere thickness has an important physical relation with rheology, which influences viscoelastic flow. High-temperature, high-pressure creep experiments have suggested that plastic deformation of olivine, which is the most abundant mineral in the mantle, will be satisfied by a thermally activated flow law if the temperature reaches 1100–1200 °C (Karato, 2010). As the isotherm is strongly dependent on the age of the oceanic lithosphere (McKenzie et al., 2005), and the 2012 Indian Ocean earthquake was located in an oceanic plate with an age of 40–60 Myr (Jacob et al., 2014; Müller et al., 2008), the rigid cold lithosphere is considered to be 70–80 km thick. Our results suggest that the average thickness of the oceanic lithosphere is 75 km, which is consistent with the value derived from thermal structure studies (McKenzie et al., 2005).

In the previous studies, Han et al. (2015), Hu et al. (2016) and Masuti et al. (2016) assumed thicknesses of the oceanic lithosphere are 60 km, 50 km and 80 km respectively. In this study, we estimate 75 km of the oceanic lithosphere thickness, which is consistent with the observed bottom of oceanic plates beneath Pacific and Philippine Sea plate inferred from seismic observation (Kawakatsu et al., 2009). If we assume the average plate age around the 2012 Indian Ocean earthquake rupture is 50 Myrs, we can put the Han et al.'s (2015), Hu et al.'s (2016) and Masuti et al.'s (2016) assumed thickness distribution and our estimated thickness in the study of Kawakatsu et al. (2009) (Figure 7.2). This indicated that oceanic lithosphere assumed in the Masuti et al. (2016) and our estimated plate thickness is reasonable.

Weak asthenosphere underlying oceanic plates has been inferred in different regions such as beneath the North American plate (James et al., 2009) from glacial isostatic adjustment and beneath the Pacific plate (Sun et al., 2014) based on postseismic deformation caused by the 2011 Tohoku-oki earthquake utilizing inland and seafloor GNSS data. These results suggest that the viscosity of the oceanic asthenosphere is lower than that of the mantle wedge. James et al. (2009) estimated the depth-dependent viscosity of the asthenosphere beneath the oceanic plate and the continental plate. Although the asthenosphere viscosity varied with depth, they determined that the steady-state viscosity is approximately 3×10^{18} Pa s within 140 km asthenosphere thickness and gradually increases below this layer. In addition, Sun et al. (2014) reported a thin layer at the lithosphere-asthenosphere boundary (at a depth of 45 km) with a viscosity of 2.5×10^{17} Pa s for both transient and steady-state viscosities. In the present study, we obtained transient and steady-state viscosities of approximately 1×10^{17} Pa s and 3×10^{18} Pa s, respectively. These values were estimated using thicknesses of 75 km for the lithosphere layer and 145 km for the asthenosphere layer. Our results are comparable with those of other studies of the asthenosphere (James et al., 2009; Sun et al., 2014).

7.1.4 Plate tectonic implication

The estimated asthenosphere viscosities in this study are 1×10^{17} Pa s for transient Kelvin viscosity and 3×10^{18} Pa s for steady-state Maxwell viscosity with thicknesses of 75 km of oceanic lithosphere and 145 km of the oceanic asthenosphere. This result indicates that a weak asthenosphere layer lies below the strong, cold, rigid oceanic lithosphere. Initially, we fixed the continental asthenosphere (mantle wedge) viscosity at 9×10^{18} Pa s following steady-state Maxwell as the average viscosity in

the subduction zone (Wang et al., 2012). Once we fixed the continental asthenosphere viscosity, our estimated oceanic rheology indicates that the viscosity of the oceanic asthenosphere is lower than that of the continental asthenosphere. This result is consistent with previous studies which suggest the lower oceanic asthenosphere viscosity is an important factor for driving plate motion (e.g. Becker, 2017; Forsyth and Uyeda, 1975). Considering plate movements, lower viscosity caused a relative weakness of the oceanic asthenosphere than the continental asthenosphere. A global mantle flow model from Becker et al. (2017) suggest the continent-ocean asthenosphere viscosity contrasts is necessary to governed the large-scale plate dynamics. In addition, to fit anisotropy and global plate motions, a relative viscosity reduction to 0.01 times with respect to the upper mantle viscosity is needed (Becker et al. 2017). Forsyth and Uyeda (1975), which was modeled the equilibrium of plate model and investigate the relative importance of driving and resistive forces of plate motion, found that oceanic viscosity needs to be eight times smaller than continental viscosity to maintain the computed drag force.

Transient rheology plays an essential element to accommodate transient stress due to coseismic stress change. Our best-fit rheology model consists of Kelvin and Maxwell viscosities. The obtained Maxwell viscosity is consistent with the viscosity derived from postglacial rebound data (Paulson and Richards, 2009) and geoid data (Schaber et al., 2009) that are not affected by the transient stress of coseismic stress change. Paulson and Richards (2009) and Schaber et al. (2009), which constrained by GRACE, relative sea level (RSL) and global geoid data, respectively, suggested the trade-off between asthenosphere viscosity η_A and its thickness H as follows

$$\eta_A = \eta_o \times \left(\frac{H}{H_o}\right)^3 \quad (15)$$

where η_o = 1 × 10^{21} Pa s and H_o = 1000 km follows Haskell constraint (Haskell, 1935; Mitrovica, 1996). Based on our asthenosphere thickness of 145 km, the Maxwell viscosity using equation (15) is 3 × 10^{18} Pa s (Table 7.1), which is consistent with our estimated Maxwell viscosity derived from postseismic deformation of the 2012 Indian Ocean earthquake. Hu et al. (2016) obtained 80 km and Han et al. (2015) assumed 160 km of oceanic asthenosphere thickness. Using equation (15) with respective asthenosphere thickness, we obtained 5 × 10^{17} and 4 × 10^{18} Pa s, respectively. However, the estimated Maxwell viscosities from postseismic deformation of Hu et al. (2016) and Han et al. (2015) are 2 × 10^{18} and 1 × 10^{19} Pa s, respectively (Table 7.1. The differences imply a bias of estimating steady-state viscosity due to a different assumption of rheology model for Hu et al. (2016) and structure simplicity of Han et al. (2015).

The viscosity and thickness of the asthenosphere under the ocean are important factors to control the shear stress induced by plate motion (basal shear stress). The plate velocity of the Indo–Australian plate in the reference frame of the Sundaland block is approximately 5 cm/year (Simon et al., 2007; Bock et al., 2003). Assuming that the asthenosphere layer is moving with the oceanic plate and reaches zero velocity at the bottom of the asthenosphere, the shear strain rate in the asthenosphere, $\dot{\varepsilon}_{xy}$, can be written as:

$$\dot{\varepsilon}_{xy} = \frac{v}{2H} \quad (16)$$

where v and H are the plate motion velocity and asthenosphere thickness, respectively. Therefore, the shear stress induced by the plate motion, τ_{xz}, is as follows:

$$\tau_{xz} = 2\eta\dot{\varepsilon}_{xy} = \frac{\eta v}{H} \tag{17}$$

where η is the Maxwell viscosity of the asthenosphere. From this, the total effect of the Hu et al. (2016) model yields shear stress in the asthenosphere layer induced by plate motion of approximately 0.04 MPa, whereas the result in this study is approximately 0.03 MPa (Table 7.2). However, based on Han et al. (2015) model, the estimated basal shear stress should be 0.1 MPa (Table 7.2). On the other hand, based on Masuti et al. (2016), if we assume that oceanic asthenosphere thickness and averaged viscosity of dislocation to diffusion creep are 140 km and 2.5×10^{19} Pa s, respectively, the estimated basal shear stress is 0.28 MPa (Tabel 7.2). The shear stress induced by the oceanic plate within 5 cm/year should be less than 0.1 MPa (Wiens and Stein, 1985). Additionally, observed gravity anomalies that constraints dynamic flow stress estimate the shear stress induced by the plate motion should be smaller than 0.26 MPa (Richter and McKenzie, 1978).

Considering that the shear stress on the asthenosphere is induced by plate motion, indeed, almost all models estimated the basal shear stress below the upper bound limit of previous studies except for the Masuti et al. (2016). But, if we assume thicker asthenosphere, the basal shear stress estimated by Masuti et al.'s (2016) model also below the upper bound limit. These studies (Richter and McKenzie, 1978; Wiens and Stein, 1985) do not have a sensitivity to constraint the lower bound of the basal shear stress. The no correlation of plate motion velocity and surface area can be explained by all of 0.5 MPa, 0.05 MPa and 0.005 MPa of basal shear stress (Forsyth

and Uyeda, 1975). Also, the compressional stress state in the middle to old oceanic lithosphere can be explained by all of 0.1 MPa, 0.01 MPa and 0.001 MPa of basal shear stress (Wiens and Stein, 1985). Postseismic deformation analysis has the advantage that it can also constraint the lower bound of the viscosity of the asthenosphere and basal shear stress that cannot be well-constrained by above studies. Our accepted model is model 2 and model 3. Based on these model, we can constrain the lower bound of the basal shear stress will be 0.01 MPa.

7.2 Conclusion

We studied the rheology of the asthenosphere based on postseismic deformation resulting from the 2012 Indian Ocean earthquake utilizing GNSS data in northern Sumatra obtained within two years from the Mw 8.6 and Mw 8.2 event. We found that coupled viscoelastic relaxation and afterslip were active after the earthquake sequence. To explain the short-term and long-term motion within two years after the earthquake, an oceanic lithosphere thickness of 75 km combined with a low transient viscosity of 1×10^{17} and a Maxwell viscosity of 3×10^{18} Pa s are required. In addition, the best-fit rheology in this study is able to explain the rapid changes of the horizontal component and postseismic uplift features in northern Sumatra within the first two months post-earthquake. The transient Kelvin viscosity and afterslip mainly explain the early stage of postseismic deformation in the first two months. These results reflect the importance of transient rheology of the asthenosphere to explain the observation that affected larger stress due to coseismic stress change. In terms of plate tectonics, these rheological structure results demonstrate the appropriate magnitude of weak asthenosphere as a lubricant layer to maintain the driving force of plate movement.

The rheology modeling in this study used several simplifying assumptions. We assumed sharp boundaries between the lithosphere, asthenosphere, and upper mantle with a uniform viscosity in each mantle layer. Also, we assumed uniform thickness for oceanic lithosphere while in nature may have spatial variation due to age dependency. Those heterogeneities should be considered in further research. The results of this study provide initial results to constrain the transient viscosity of the oceanic asthenosphere based on GNSS data obtained after the 2012 Indian Ocean earthquake.

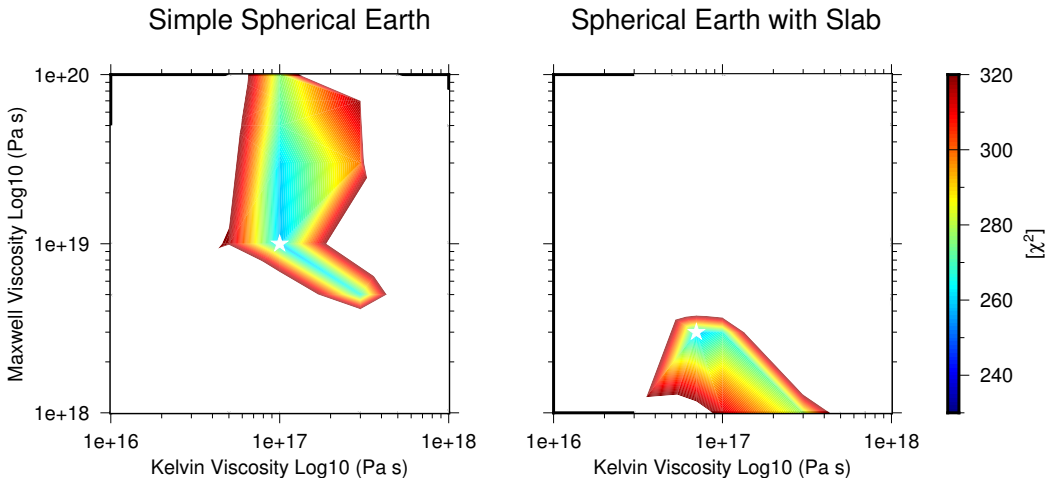

(a) (b)

Figure 7.1 χ^2 misfit distribution with trade off between Maxwell Viscosity and Kelvin Viscosity for model (a) that exclude the elastic slab and model (b) that include the elastic slab. White star indicates optimum model.

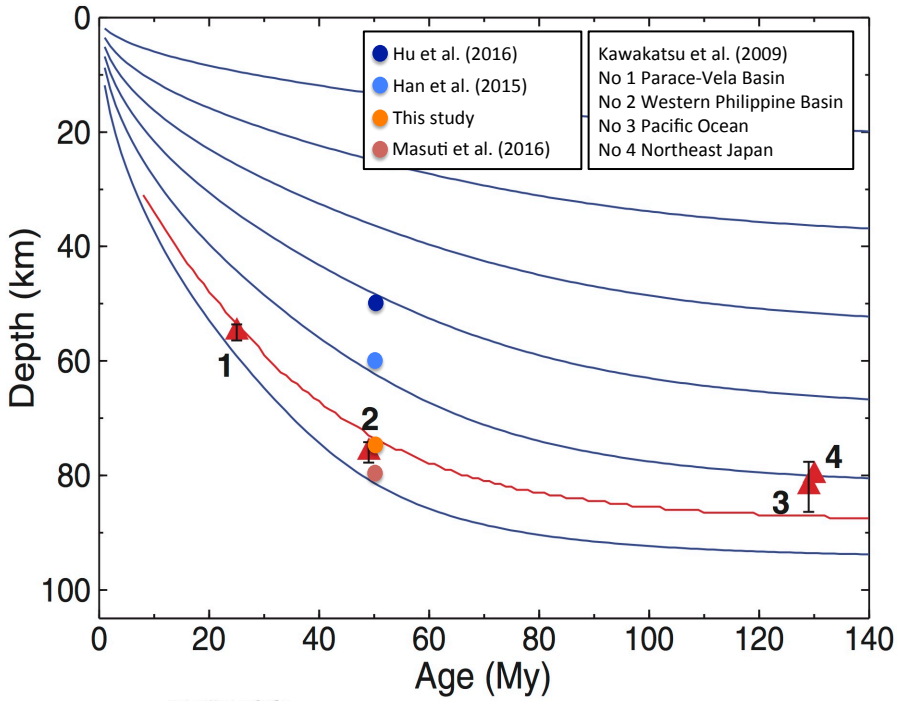

Figure 7.2 Observed lithosphere-asthenosphere boundary depths correspond with plate age. Red lines indicates the upper limit of the partial melting region based on the model of Mierdel et al. (2007)**. Blue lines denotes isotherms with a 200⁰ C intervals taken from** Stein and Stein (1992)**. (Similar as Figure 4a of Kawakatsu et al. (2009))**

Table 7.1 Comparison between estimated Maxwell viscosity of postseismic deformation and other studies

Model	Maxwell Viscosity (Pa s)	Asthenosphere Thickness (Km)	Estimated Maxwell viscosity based on equation (15)
Han et al. (2015)	1×10^{19}	160	4×10^{18}
Hu et al. (2016)	2×10^{18}	80	5×10^{17}
Model 3	3×10^{18}	145	3×10^{18}

Table 7.2 Estimated basal shear stress based on rheology model

Model	Maxwell Viscosity (Pa s)	Asthenosphere Thickness (Km)	Estimated Basal Shear Stress (MPa)
Han et al. (2015)	1×10^{19}	160	0.1
Hu et al. (2016)	2×10^{18}	80	0.04
Masuti et al. (2016)*	2.5×10^{19}	140	0.28
Model 1	5×10^{17}	150	0.005
Model 2	1×10^{18}	145	0.01
Model 3	3×10^{18}	145	0.03

*Parameter explanation for Masuti et al. (2016) model is on the text.

Bibliography

Aagaard, B.T.; Kientz, S; Knepley, M.G; Strand, L.;Williams, C. . (2015). *PyLith User Manual, Version 2.1.0*. Davis: Computational Infrastructure of Geodynamic, Davis, CA. Retrieved from geodynamics.org/cig/software/pylith/pylith_manual-2.1.0.pdf'

Aagaard, B. T., Knepley, M. G., & Williams, C. A. (2013). A domain decomposition approach to implementing fault slip in finite-element models of quasi-static and dynamic crustal deformation. *Journal of Geophysical Research: Solid Earth*, *118*(6), 3059–3079. http://doi.org/10.1002/jgrb.50217

Aagaard, B., Williams, C., & Knepley, M. (2015). *PyLith v2.1.0 [software]*. Computational Infrastructure for Geodynamics. http://doi.org/NoDOI

Abercrombie, R. E. (2003). 7.9 earthquakes south of Sumatra: Deformation in the India–Australia Plate. *Journal of Geophysical Research*, *108*(B1), 1–16. http://doi.org/10.1029/2001JB000674

Aderhold, K., & Abercrombie, R. E. (2016). Seismotectonics of a diffuse plate boundary: Observations off the Sumatra-Andaman trench. *Journal of*

Geophysical Research: Solid Earth, *121*(5), 3462–3478. http://doi.org/10.1002/2015JB012721

Ali, S. T., & Freed, A. M. (2010). Contemporary deformation and stressing rates in Southern Alaska. *Geophysical Journal International*, *183*(2), 557–571. http://doi.org/10.1111/j.1365-246X.2010.04784.x

Altamimi, Z., Collilieux, X., Legrand, J., Garayt, B., & Boucher, C. (2007). ITRF2005: A new release of the International Terrestrial Reference Frame based on time series of station positions and Earth Orientation Parameters. *Journal of Geophysical Research*, *112*(B9), B09401. http://doi.org/10.1029/2007JB004949

Altamimi, Z., Collilieux, X., & Métivier, L. (2011). ITRF2008: An improved solution of the international terrestrial reference frame. *Journal of Geodesy*, *85*(8), 457–473. http://doi.org/10.1007/s00190-011-0444-4

Altamimi, Z., Métivier, L., & Collilieux, X. (2012). ITRF2008 plate motion model. *Journal of Geophysical Research*. http://doi.org/10.1029/2011JB008930

Andrade, V., & Rajendran, K. (2014). The April 2012 Indian Ocean earthquakes: SEISMOTECTONIC context and implications for their mechanisms. *Tectonophysics*, *617*, 126–139. http://doi.org/10.1016/j.tecto.2014.01.024

Antolik, M., Abercrombie, R. E., Pan, J., & Ekström, G. (2006). Rupture characteristics of the 2003 Mw7.6 mid-Indian Ocean earthquake: Implications for seismic properties of young oceanic lithosphere. *Journal of Geophysical Research: Solid Earth*, *111*(4). http://doi.org/10.1029/2005JB003785

Anugrah, B., Meilano, I., Gunawan, E., & Efendi, J. (2015). Estimation of postseismic deformation parameters from continuous GPS data in northern Sumatra after the 2004 Sumatra-Andaman earthquake. *Earthquake Science*, *28*(5–6), 347–352. http://doi.org/10.1007/s11589-015-0136-x

Ardika, M., Meilano, I., & Gunawan, E. (2015). Postseismic deformation parameters of the 2010 M7.8 Mentawai, Indonesia, earthquake inferred from continuous GPS observations. *Asian Journal of Earth Sciences*, *8*(4), 127–133. http://doi.org/10.3923/ajes.2015.127.133

Becker, J. J., Sandwell, D. T., Smith, W. H. F., Braud, J., Binder, B., Depner, J., … Weatherall, P. (2009). Global Bathymetry and Elevation Data at 30 Arc Seconds Resolution: SRTM30_PLUS. *Marine Geodesy*, *32*(4), 355–371. http://doi.org/10.1080/01490410903297766

Becker, T. W. (2017). Superweak asthenosphere in light of upper mantle seismic anisotropy. *Geochemistry, Geophysics, Geosystems*, *18*(5), 1986–2003. http://doi.org/10.1002/2017GC006886

Bergman, E. A., & Solomon, S. C. (1985). Earthquake source mechanisms from body-waveform inversion and intraplate tectonics in the northern Indian Ocean. *Physics of the Earth and Planetary Interiors*, *40*(1), 1–23. http://doi.org/10.1016/0031-9201(85)90002-0

Biggs, J., Burgmann, R., Freymueller, J. T., Lu, Z., Parsons, B., Ryder, I., … Wright, T. (2009). The postseismic response to the 2002 M 7.9 Denali Fault earthquake: Constraints from InSAR 2003-2005. *Geophysical Journal International*, *176*(2), 353–367. http://doi.org/10.1111/j.1365-246X.2008.03932.x

Bird, P. (2003). An updated digital model of plate boundaries. *Geochemistry, Geophysics, Geosystems*, *4*(3). http://doi.org/10.1029/2001GC000252

Bradley, K. E., Feng, L., Hill, E. M., Natawidjaja, D. H., & Sieh, K. E. (2016). Implications of the diffuse deformation of the Indian Ocean lithosphere for slip partitioning of oblique plate convergence in Sumatra. *Journal of Geophysical Research*, *121*, 572–591. http://doi.org/10.1002/2016JB013549

Braun, J. (2003). Pecube: A new finite-element code to solve the 3D heat transport equation including the effects of a time-varying, finite amplitude surface topography. *Computers and Geosciences*, *29*(6), 787–794. http://doi.org/10.1016/S0098-3004(03)00052-9

Bürgmann, R., & Dresen, G. (2008). Rheology of the Lower Crust and Upper Mantle: Evidence from Rock Mechanics, Geodesy, and Field Observations. *Annual Review of Earth and Planetary Sciences*, *36*(1), 531–567. http://doi.org/10.1146/annurev.earth.36.031207.124326

Chlieh, M., Avouac, J. P., Hjorleifsdottir, V., Song, T. R. A., Ji, C., Sieh, K., … Galetzka, J. (2007). Coseismic slip and afterslip of the great Mw 9.15 Sumatra-Andaman earthquake of 2004. *Bulletin of the Seismological Society of America*, *97*(1 A SUPPL.). http://doi.org/10.1785/0120050631

Cloetingh, S., & Wortel, R. (1986). Stress in the Indo-Australian plate. *Tectonophysics*, *132*(1–3), 49–67. http://doi.org/10.1016/0040-1951(86)90024-7

Dach, R., Hugentobler, U., Fridez, P., & Meindl, M. (2007). Bernese GPS software version 5.0. User manual. *Astronomical Institute, University of Bern*, *640*(January), 640. http://doi.org/10.1016/S0376-7361(09)70018-4

Delescluse, M., & Chamot-Rooke, N. (2007). Instantaneous deformation and kinematics of the India-Australia Plate. *Geophysical Journal International*, *168*(2), 818–842. http://doi.org/10.1111/j.1365-246X.2006.03181.x

Delescluse, M., Chamot-Rooke, N., Cattin, R., Fleitout, L., Trubienko, O., & Vigny, C. (2012). April 2012 intra-oceanic seismicity off Sumatra boosted by the Banda-Aceh megathrust. *Nature*, *490*(7419), 240–244. http://doi.org/10.1038/nature11520

Demets, C., Gordon, R. G., & Argus, D. F. (1988). Intraplate deformation and closure

of the Australia-Antarctica-Africa plate circuit. *Journal of Geophysical Research*, *93*(B10), 11877–11897. http://doi.org/10.1029/JB093iB10p11877

DeMets, C., Gordon, R. G., Argus, D. F., & Stein, S. (1994). Effect of recent revisions to the geomagnetic reversal time scale on estimates of current plate motions. *Geophysical Research Letters*, *21*(20), 2191–2194. http://doi.org/10.1029/94GL02118

Diao, F., Xiong, X., Wang, R., Zheng, Y., Walter, T. R., Weng, H., & Li, J. (2013). Overlapping post-seismic deformation processes: Afterslip and viscoelastic relaxation following the 2011Mw 9.0 tohoku (Japan) earthquake. *Geophysical Journal International*, *196*(1), 218–229. http://doi.org/10.1093/gji/ggt376

Duputel, Z., Kanamori, H., Tsai, V. C., Rivera, L., Meng, L., Ampuero, J. P., & Stock, J. M. (2012). The 2012 Sumatra great earthquake sequence. *Earth and Planetary Science Letters*, *351–352*, 247–257. http://doi.org/10.1016/j.epsl.2012.07.017

Dziewonski, A. M., & Anderson, D. L. (1981). Preliminary reference Earth model. *Physics of the Earth and Planetary Interiors*, *25*(4), 297–356. http://doi.org/10.1016/0031-9201(81)90046-7

Feng, L., Hill, E. M., Banerjee, P., Hermawan, I., Tsang, L. L. H., Natawidjaja, D. H., … Sieh, K. (2015). A unified GPS-based earthquake catalog for the Sumatran plate boundary between 2002 and 2013. *Journal of Geophysical Research B: Solid Earth*. http://doi.org/10.1002/2014JB011661

Forsyth, D., & Uyedaf???, S. (1975). On the Relative Importance of the Driving Forces of Plate Motion. *Geophysical Journal of the Royal Astronomical Society*, *43*(1), 163–200. http://doi.org/10.1111/j.1365-246X.1975.tb00631.x

Freed, A. M. (2007). Afterslip (and only afterslip) following the 2004 Parkfield,

California, earthquake. *Geophysical Research Letters*, *34*(6). http://doi.org/10.1029/2006GL029155

Freed, A. M., & Bürgmann, R. (2004). Evidence of power-law flow in the Mojave desert mantle. *Nature*, *430*(6999), 548–551. http://doi.org/10.1038/nature02784

Freed, A. M., Bürgmann, R., Calais, E., Freymueller, J., & Hreinsdóttir, S. (2006). Implications of deformation following the 2002 Denali, Alaska, earthquake for postseismic relaxation processes and lithospheric rheology. *Journal of Geophysical Research: Solid Earth*, *111*(1). http://doi.org/10.1029/2005JB003894

Freed, A. M., Bürgmann, R., & Herring, T. (2007). Far-reaching transient motions after Mojave earthquakes require broad mantle flow beneath a strong crust. *Geophysical Research Letters*, *34*(19). http://doi.org/10.1029/2007GL030959

Freed, A. M., Hashima, A., Becker, T. W., Okaya, D. A., Sato, H., & Hatanaka, Y. (2017). Resolving depth-dependent subduction zone viscosity and afterslip from postseismic displacements following the 2011 Tohoku-oki, Japan earthquake. *Earth and Planetary Science Letters*, *459*, 279–290. http://doi.org/10.1016/j.epsl.2016.11.040

Frey, F. A., Pringle, M., Meleney, P., Huang, S., & Piotrowski, A. (2011). Diverse mantle sources for Ninetyeast Ridge magmatism: Geochemical constraints from basaltic glasses. *Earth and Planetary Science Letters*, *303*(3–4), 215–224. http://doi.org/10.1016/j.epsl.2010.12.051

Gardner, G. H. F., Gardner, L. W., & Gregory, A. R. (1974). FORMATION VELOCITY AND DENSITY—THE DIAGNOSTIC BASICS FOR STRATIGRAPHIC TRAPS. *GEOPHYSICS*, *39*(6), 770–780. http://doi.org/10.1190/1.1440465

Gómez, D. D., Bevis, M., Pan, E., & Smalley, R. (2017). The Influence of Gravity on the Displacement Field Produced by Fault Slip. *Geophysical Research Letters*, *44*(18), 9321–9329. http://doi.org/10.1002/2017GL074113

Gordon, R. G. (1998). THE PLATE TECTONIC APPROXIMATION: Plate Nonrigidity, Diffuse Plate Boundaries, and Global Plate Reconstructions. *Annual Review of Earth and Planetary Sciences*, *26*(1), 615–642. http://doi.org/10.1146/annurev.earth.26.1.615

Gordon, R. G., & Stein, S. (1992). Global tectonics and space geodesy. *Science (New York, N.Y.)*, *256*(5055), 333–342. http://doi.org/10.1126/science.256.5055.333

Gudmundsson, Ó., & Sambridge, M. (1998). A regionalized upper mantle (RUM) seismic model. *Journal of Geophysical Research*, *103*(B4), 7121–7136. http://doi.org/10.1029/97JB02488

Gunawan, E., Maulida, P., Meilano, I., Irsyam, M., & Efendi, J. (2016). Analysis of Coseismic Fault Slip Models of the 2012 Indian Ocean Earthquake: Importance of GPS Data for Crustal Deformation Studies. *Acta Geophysica*, *64*(6), 2136–2150. http://doi.org/10.1515/acgeo-2016-0106

Gunawan, E., Meilano, I., Abidin, H. Z., Hanifa, N. R., & Susilo. (2016). Investigation of the best coseismic fault model of the 2006 Java tsunami earthquake based on mechanisms of postseismic deformation. *Journal of Asian Earth Sciences*, *117*, 64–72. http://doi.org/10.1016/j.jseaes.2015.12.003

Gunawan, E., Sagiya, T., Ito, T., Kimata, F., Tabei, T., Ohta, Y., … Sugiyanto, D. (2014). A comprehensive model of postseismic deformation of the 2004 Sumatra-Andaman earthquake deduced from GPS observations in northern Sumatra. *Journal of Asian Earth Sciences*, *88*, 218–229. http://doi.org/10.1016/j.jseaes.2014.03.016

Hamilton, W. (1979). Tectonics of the Indonesian Region. *Geological Society of Malaysia, Bulletin*, *6*, 3–10. http://doi.org/10.1016/0003-6870(73)90259-7

Hamling, I. J., Hreinsdóttir, S., Clark, K., Elliott, J., Liang, C., Fielding, E., … Stirling, M. (2017). Complex multifault rupture during the 2016 Mw7.8 Kaikōura earthquake, New Zealand. *Science*, *356*(6334). http://doi.org/10.1126/science.aam7194

Han, S. C., Sauber, J., & Pollitz, F. (2015). Coseismic compression/dilatation and viscoelastic uplift/subsidence following the 2012 Indian Ocean earthquakes quantified from satellite gravity observations. *Geophysical Research Letters*, 3764–3772. http://doi.org/10.1002/2015GL063819

Hanifa, N. R., Sagiya, T., Kimata, F., Efendi, J., Abidin, H. Z., & Meilano, I. (2014). Interplate coupling model off the southwestern coast of Java, Indonesia, based on continuous GPS data in 2008-2010. *Earth and Planetary Science Letters*, *401*, 159–171. http://doi.org/10.1016/j.epsl.2014.06.010

Hashima, A., Becker, T. W., Freed, A. M., Sato, H., & Okaya, D. A. (2016). Coseismic deformation due to the 2011 Tohoku-oki earthquake: influence of 3-D elastic structure around Japan. *Earth, Planets and Space*, *68*(1), 159. http://doi.org/10.1186/s40623-016-0535-9

Haskell, N. A. (1935). The motion of a fluid under a surface load, 1. *Physics*, *6*(1935), 265–269. http://doi.org/10.1063/1.1745329

Hearn, E. H., Bürgmann, R., & Reilinger, R. E. (2002). Dynamics of İzmit earthquake postseismic deformation and loading of the Düzce earthquake hypocenter. *Bulletin of the Seismological Society of America*, *92*(1), 172–193. http://doi.org/10.1785/0120000832

Hill, E. M., Yue, H., Barbot, S., Lay, T., Tapponnier, P., Hermawan, I., … Sieh, K.

(2015). The 2012 Mw 8.6 Wharton Basin sequence: A cascade of great earthquakes generated by near-orthogonal, young, oceanic mantle faults. *Journal of Geophysical Research: Solid Earth*, *120*(5), 3723–3747. http://doi.org/10.1002/2014JB011703

Hines, T. T., & Hetland, E. A. (2016). Rapid and simultaneous estimation of fault slip and heterogeneous lithospheric viscosity from post-seismic deformation. *Geophysical Journal International*, *204*(1), 569–582. http://doi.org/10.1093/gji/ggv477

Hsu, Y. J., Simons, M., Williams, C., & Casarotti, E. (2014). Three-dimensional FEM derived elastic Green's functions for the coseismic deformation of the 2005 Mw 8.7 Nias-Simeulue, Sumatra earthquake. *Geochemistry, Geophysics, Geosystems*, *12*(7). http://doi.org/10.1029/2011GC003553

Hu, Y., Bürgmann, R., Banerjee, P., Feng, L., Hill, E. M., Ito, T., … Wang, K. (2016). Asthenosphere rheology inferred from observations of the 2012 Indian Ocean earthquake. *Nature*, *538*(7625), 368–372. http://doi.org/10.1038/nature19787

Hu, Y., & Wang, K. (2012a). Spherical-Earth finite element model of short-term postseismic deformation following the 2004 Sumatra earthquake. *Journal of Geophysical Research*, *117*(B5), 1–15. http://doi.org/10.1029/2012JB009153

Hu, Y., & Wang, K. (2012b). Spherical-Earth finite element model of short-term postseismic deformation following the 2004 Sumatra earthquake. *Journal of Geophysical Research: Solid Earth*, *117*(B5), n/a-n/a. http://doi.org/10.1029/2012JB009153

Ishii, M., Kiser, E., & Geist, E. L. (2013). Mw 8.6 Su matran earthquake of 11 April 2012: Rare seaward expression of oblique subduction. *Geology*, *41*(3), 319–322. http://doi.org/10.1130/G33783.1

Ito, T., Gunawan, E., Kimata, F., Tabei, T., Meilano, I., Agustan, … Sugiyanto, D. (2016). Co-seismic offsets due to two earthquakes (Mw6.1) along the Sumatran fault system derived from GNSS measurements. *Earth, Planets and Space*, *68*(1). http://doi.org/10.1186/s40623-016-0427-z

Ito, T., Gunawan, E., Kimata, F., Tabei, T., Simons, M., Meilano, I., … Sugiyanto, D. (2012). Isolating along-strike variations in the depth extent of shallow creep and fault locking on the northern Great Sumatran Fault. *Journal of Geophysical Research: Solid Earth*, *117*(6), 1–16. http://doi.org/10.1029/2011JB008940

Ito, T., Ozawa, K., Watanabe, T., & Sagiya, T. (2011). Slip distribution of the 2011 off the Pacific coast of Tohoku Earthquake inferred from geodetic data. *Earth, Planets and Space*, *63*(7), 627–630. http://doi.org/10.5047/eps.2011.06.023

Jacob, J., Dyment, J., & Yatheesh, V. (2014). Revisiting the structure, age, and evolution of the Wharton Basin to better understand subduction under Indonesia. *Journal of Geophysical Research: Solid Earth*, *119*(1), 169–190. http://doi.org/10.1002/2013JB010285

Jade, S., Shrungeshwara, T. S., Kumar, K., Choudhury, P., Dumka, R. K., & Bhu, H. (2017). India plate angular velocity and contemporary deformation rates from continuous GPS measurements from 1996 to 2015. *Scientific Reports*, *7*(1). http://doi.org/10.1038/s41598-017-11697-w

James, T. S., Gowan, E. J., Wada, I., & Wang, K. (2009). Viscosity of the asthenosphere from glacial isostatic adjustment and subduction dynamics at the northern Cascadia subduction zone, British Columbia, Canada. *Journal of Geophysical Research: Solid Earth*, *114*(4). http://doi.org/10.1029/2008JB006077

Johnson, K. M., Bürgmann, R., & Freymueller, J. T. (2009). Coupled afterslip and

viscoelastic flow following the 2002 Denali Fault, Alaska earthquake. *Geophysical Journal International*, *176*(3), 670–682. http://doi.org/10.1111/j.1365-246X.2008.04029.x

Karato, S. -i., & Wu, P. (1993). Rheology of the Upper Mantle: A Synthesis. *Science*, *260*(5109), 771–778. http://doi.org/10.1126/science.260.5109.771

Karato, S. I., & Jung, H. (2003). Effects of pressure on high-temperature dislocation creep in olivine. *Philosophical Magazine*, *83*(3), 401–414. http://doi.org/10.1080/0141861021000025829

Karato, S. ichiro. (2010). Rheology of the deep upper mantle and its implications for the preservation of the continental roots: A review. *Tectonophysics*, *481*(1–4), 82–98. http://doi.org/10.1016/j.tecto.2009.04.011

Kawakatsu, H., Kumar, P., Takei, Y., Shinohara, M., Kanazawa, T., Araki, E., & Suyehiro, K. (2009). Seismic evidence for sharp lithosphere-asthenosphere boundaries of oceanic plates. *Science*, *324*(5926), 499–502. http://doi.org/10.1126/science.1169499

Kennett, B. L. N., Engdahl, E. R., & Buland, R. (1995). Constraints on seismic velocities in the Earth from traveltimes. *Geophysical Journal International*, *122*(1), 108–124. http://doi.org/10.1111/j.1365-246X.1995.tb03540.x

King, S. ~D. (1995). *Models of mantle viscosity*. *Rock Physics and Phase Relations*. http://doi.org/10.1029/RF002p0227

Konca, A. O., Hjorleifsdottir, V., Song, T. R. A., Avouac, J. P., Helmberger, D. V., Ji, C., … Meltzner, A. (2007). Rupture kinematics of the 2005 Mw 8.6 m Nias-Simeulue earthquake from the joint inversion of seismic and geodetic data. *Bulletin of the Seismological Society of America*, *97*(1 A SUPPL.). http://doi.org/10.1785/0120050632

Kreemer, C., Blewitt, G., & Klein, E. C. (2014). A geodetic plate motion and Global Strain Rate Model. *Geochemistry, Geophysics, Geosystems*, *15*(10), 3849–3889. http://doi.org/10.1002/2014GC005407

Kreemer, C., Blewitt, G., & Maerten, F. (2006). Co- and postseismic deformation of the 28 March 2005 Nias Mw 8.7 earthquake from continuous GPS data. *Geophysical Research Letters*, *33*(7). http://doi.org/10.1029/2005GL025566

Lay, T., Ye, L., Ammon, C. J., Dunham, A., & Koper, K. D. (2016). The 2 March 2016 Wharton Basin Mw7.8 earthquake: High stress drop north-south strike-slip rupture in the diffuse oceanic deformation zone between the Indian and Australian Plates. *Geophysical Research Letters*, *43*(15), 7937–7945. http://doi.org/10.1002/2016GL069931

Le Pichon, X. (1968). Sea-floor spreading and continental drift. *Journal of Geophysical Research*, *73*(12), 3661–3697. http://doi.org/10.1029/JB073i012p03661

Lechmann, S. M., May, D. A., Kaus, B. J. P., & Schmalholz, S. M. (2011). Comparing thin-sheet models with 3-D multilayer models for continental collision. *Geophysical Journal International*, *187*(1), 10–33. http://doi.org/10.1111/j.1365-246X.2011.05164.x

Loveless, J. P., & Meade, B. J. (2016). Two decades of spatiotemporal variations in subduction zone coupling offshore Japan. *Earth and Planetary Science Letters*, *436*, 19–30. http://doi.org/10.1016/j.epsl.2015.12.033

Marone, C. J., Scholtz, C. H., & Bilham, R. (1991). On the mechanics of earthquake afterslip. *Journal of Geophysical Research*, *96*(B5), 8441. http://doi.org/10.1029/91JB00275

Masuti, S., Barbot, S. D., Karato, S. I., Feng, L., & Banerjee, P. (2016). Upper-mantle

water stratification inferred from observations of the 2012 Indian Ocean earthquake. *Nature*, *538*(7625), 371–377. http://doi.org/10.1038/nature19783

Matthews, K. J., Mller, R. D., Wessel, P., & Whittaker, J. M. (2011). The tectonic fabric of the ocean basins. *Journal of Geophysical Research: Solid Earth*, *116*(12). http://doi.org/10.1029/2011JB008413

Maulida, P., Meilano, I., Gunawan, E., & Efendi, J. (2016). Analysis of 2012 M8.6 Indian Ocean earthquake coseismic slip model based on GPS data. In *AIP Conference Proceedings* (Vol. 1730). http://doi.org/10.1063/1.4947396

McCaffrey, R. (2009). The Tectonic Framework of the Sumatran Subduction Zone. *Annual Review of Earth and Planetary Sciences*, *37*(1), 345–366. http://doi.org/10.1146/annurev.earth.031208.100212

McKenzie, D., Jackson, J., & Priestley, K. (2005). Thermal structure of oceanic and continental lithosphere. *Earth and Planetary Science Letters*, *233*(3–4), 337–349. http://doi.org/10.1016/j.epsl.2005.02.005

McKenzie, D. P., & Parker, R. L. (1967). The North Pacific: An example of tectonics on a sphere. *Nature*, *216*(5122), 1276–1280. http://doi.org/10.1038/2161276a0

Melosh, H., & Raefsky, A. (1981). A simple and efficient method for introducing faults into finite element computations. *Bulletin of the Seismological Society of America*, *71*(5), 1391–1400. Retrieved from http://www.bssaonline.org/content/71/5/1391.short

Meng, L., Ampuero, J. P., Stock, J., Duputel, Z., Luo, Y., & Tsai, V. C. (2012). Earthquake in a maze: Compressional rupture branching during the 2012 Mw 8.6 Sumatra earthquake. *Science*, *337*(6095), 724–726. http://doi.org/10.1126/science.1224030

Mierdel, K., Keppler, H., Smyth, J. R., & Langenhorst, F. (2007). Water solubility in

aluminous orthopyroxene and the origin of earth's asthenosphere. *Science*, *315*(5810), 364–368. http://doi.org/10.1126/science.1135422

Mitrovica, J. X. (1996). Haskell [1935] revisited. *Journal of Geophysical Research: Solid Earth*, *101*(B1), 555–569. http://doi.org/10.1029/95JB03208

Moore, J. D. P., Yu, H., Tang, C. H., Wang, T., Barbot, S., Peng, D., … Shibazaki, B. (2017). Imaging the distribution of transient viscosity after the 2016 Mw7.1 Kumamoto earthquake. *Science*, *356*(6334), 163–167. http://doi.org/10.1126/science.aal3422

Morgan, W. J. (1968). Rises, Trenches, Great Faults and Crustal Blocks. *Journal of Geophysical Research*, *73*(6), 1959–1982. http://doi.org/10.1016/0040-1951(91)90408-K

Müller, R. D., Sdrolias, M., Gaina, C., & Roest, W. R. (2008). Age, spreading rates, and spreading asymmetry of the world's ocean crust. *Geochemistry, Geophysics, Geosystems*, *9*(4). http://doi.org/10.1029/2007GC001743

Nikolaidis, R. M., & Bock, Y. (2002). Observation of Geodetic and Seismic Deformation with the Global Positioning System. *Earth Sciences*, *Ph.D*, 265. http://doi.org/10.1029/2001JB000329

Nobre Silva, I. G., Weis, D., Scoates, J. S., & Barling, J. (2013). The ninetyeast ridge and its relation to the Kerguelen, Amsterdam and St. Paul hotspots in the Indian Ocean. *Journal of Petrology*, *54*(6), 1177–1210. http://doi.org/10.1093/petrology/egt009

Nostro, C., Piersanti, A., Antonloll, A., & Spada @bullet, G. (1999). Spherical versus ttat models of coseismic and postseismic deformations. *JOURNAL OF GEOPHYSICAL RESEARCH*, *104134*(10), 115–13. http://doi.org/10.1029/1999JB900097

Ohta, Y., Miura, S., Iinuma, T., Tachibana, K., Matsushima, T., Takahashi, H., … Hasegawa, A. (2008). Coseismic and postseismic deformation related to the 2007 Chuetsu-oki, Niigata Earthquake. *Earth, Planets and Space*, *60*(11), 1081–1086.

Panet, I., Pollitz, F., Mikhailov, V., Diament, M., Banerjee, P., & Grijalva, K. (2010). Upper mantle rheology from GRACE and GPS postseismic deformation after the 2004 Sumatra-Andaman earthquake. *Geochemistry, Geophysics, Geosystems*, *11*(6). http://doi.org/10.1029/2009GC002905

Paul, J., Bürgmann, R., Gaur, V. K., Bilham, R., Larson, K. M., Ananda, M. B., … Kumar, D. (2001). The motion and active deformation of India. *Geophysical Research Letters*, *28*(4), 647–650. http://doi.org/10.1029/2000GL011832

Paul, J., Lowry, A. R., Bilham, R., Sen, S., & Smalley, J. (2007). Postseismic deformation of the Andaman Islands following the 26 December, 2004 Great Sumatra-Andaman earthquake. *Geophysical Research Letters*, *34*(19). http://doi.org/10.1029/2007GL031024

Paul, J., Rajendran, C. P., Lowry, A. R., Andrade, V., & Rajendran, K. (2012). Andaman postseismic deformation observations: Still slipping after all these years? *Bulletin of the Seismological Society of America*, *102*(1), 343–351. http://doi.org/10.1785/0120110074

Paulson, A., & Richards, M. A. (2009). On the resolution of radial viscosity structure in modelling long-wavelength postglacial rebound data. *Geophysical Journal International*, *179*(3), 1516–1526. http://doi.org/10.1111/j.1365-246X.2009.04362.x

Peltzer, G., Rosen, P., Rogez, F., & Hudnut, K. (1998). Poroelastic rebound along the Landers 1992 earthquake surface rupture. *Journal of Geophysical Research*,

103(B12), 30131. http://doi.org/10.1029/98JB02302

Petroy, D. E., & Wiens, D. a. (1989). Historical seismicity and implications for diffuse plate convergence in the northeast Indian Ocean. *Journal of Geophysical Research*, *94*(B9), 12301. http://doi.org/10.1029/JB094iB09p12301

Pollitz, F., Banerjee, P., Grijalva, K., Nagarajan, B., & Bürgmann, R. (2008). Effect of 3-D viscoelastic structure on post-seismic relaxation from the 2004 M = 9.2 Sumatra earthquake. *Geophysical Journal International*, *173*(1), 189–204. http://doi.org/10.1111/j.1365-246X.2007.03666.x

Pollitz, F. F. (1997). Gravitational viscoelastic postseismic relaxation on a layered spherical Earth. *Journal of Geophysical Research: Solid Earth*, *102*(B8), 17921–17941. http://doi.org/10.1029/97JB01277

Pollitz, F. F., Bürgmann, R., & Romanowicz, B. (1998). Viscosity of oceanic asthenosphere inferred from remote triggering of earthquakes. *Science*, *280*(5367), 1245–1249. http://doi.org/10.1126/science.280.5367.1245

Pollitz, F. F., Kobayashi, T., Yarai, H., Shibazaki, B., & Matsumoto, T. (2017). Viscoelastic lower crust and mantle relaxation following the 14–16 April 2016 Kumamoto, Japan, earthquake sequence. *Geophysical Research Letters*, *44*(17), 8795–8803. http://doi.org/10.1002/2017GL074783

Pollitz, F. F., Wicks, C., & Thatcher, W. (2001). Mantle flow beneath a continental strike-slip fault: Postseismic deformation after the 1999 Hector Mine earthquake. *Science*, *293*(5536), 1814–1818. http://doi.org/10.1126/science.1061361

Pratama, C., Ito, T., & Tabei, T. (2017). Inhomogeneous spherical-earth finite element model of coseismic offset due to the 2012 Indian Ocean Earthquake. In *AIP Conference Proceedings* (Vol. 1857). http://doi.org/10.1063/1.4987066

Prawirodirdjo, L., Bock, Y., Genrich, J. F., Puntodewo, S. S. O., Rais, J., Subarya, C.,

& Sutisna, S. (2000). One century of tectonic deformation along the Sumatran fault from triangulation and Global Positioning System surveys. *Journal of Geophysical Research*, *105*(B12), 28343. http://doi.org/10.1029/2000JB900150

Rajendran, K., Andrade, V., & Rajendran, C. P. (2011). The June 2010 Nicobar earthquake: Fault reactivation on the subducting oceanic plate. *Bulletin of the Seismological Society of America*, *101*(5), 2568–2577. http://doi.org/10.1785/0120110002

Rhie, J., Dreger, D., Bürgmann, R., & Romanowicz, B. (2007). Slip of the 2004 Sumatra-Andaman earthquake from joint inversion of long-period global seismic waveforms and GPS static offsets. *Bulletin of the Seismological Society of America*, *97*(1 A SUPPL.). http://doi.org/10.1785/0120050620

Robinson, D. P., Henry, C., Das, S., & Woodhouse, J. H. (2001). Simultaneous rupture along two conjugate planes of the Wharton Basin earthquake. *Science*, *292*(5519), 1145–1148. http://doi.org/10.1126/science.1059395

Royer, J. Y., & Gordon, R. G. (1997). The motion and boundary between the Capricorn and Australian plates. *Science*, *277*(5330), 1268–1274. http://doi.org/10.1126/science.277.5330.1268

Rummel, R. (2010). The interdisciplinary role of space geodesy-Revisited. *Journal of Geodynamics*, *49*(3–4), 112–115. http://doi.org/10.1016/j.jog.2009.10.006

Sager, W. W., Bull, J. M., & Krishna, K. S. (2013). Active faulting on the Ninetyeast Ridge and its relation to deformation of the Indo-Australian plate. *Journal of Geophysical Research: Solid Earth*, *118*(8), 4648–4668. http://doi.org/10.1002/jgrb.50319

Sasajima, R., & Ito, T. (2016). Strain rate dependency of oceanic intraplate earthquake b-values at extremely low strain rates. *Journal of Geophysical*

Research: Solid Earth, *121*(6), 4523–4537. http://doi.org/10.1002/2016JB013221

Sato, R. (1971). Crustal deformation due to dislocation in a multi-layered medium. *Journal of Physics of the Earth*, *19*(1). http://doi.org/10.4294/jpe1952.19.31

Satriano, C., Kiraly, E., Bernard, P., & Vilotte, J. P. (2012). The 2012 Mw 8.6 Sumatra earthquake: Evidence of westward sequential seismic ruptures associated to the reactivation of a N-S ocean fabric. *Geophysical Research Letters*, *39*(15). http://doi.org/10.1029/2012GL052387

Schaber, K., Bunge, H. P., Schuberth, B. S. A., Malservisi, R., & Horbach, A. (2009). Stability of the rotation axis in high-resolution mantle circulation models: Weak polar wander despite strong core heating. *Geochemistry, Geophysics, Geosystems*, *10*(11). http://doi.org/10.1029/2009GC002541

Shibazaki, B., Okada, T., Muto, J., Matsumoto, T., Yoshida, T., & Yoshida, K. (2016). Heterogeneous stress state of island arc crust in northeastern Japan affected by hot mantle fingers. *Journal of Geophysical Research: Solid Earth*, *121*(4), 3099–3117. http://doi.org/10.1002/2015JB012664

Simons, W. J. F., Socquet, A., Vigny, C., Ambrosius, B. A. C., Abu, S. H., Promthong, C., … Spakman, W. (2007). A decade of GPS in Southeast Asia: Resolving Sundaland motion and boundaries. *Journal of Geophysical Research: Solid Earth*, *112*(6). http://doi.org/10.1029/2005JB003868

Singh, S. C., Hananto, N., Qin, Y., Leclerc, F., Avianto, P., Tapponnier, P. E., … Barbot, S. (2017). The discovery of a conjugate system of faults in the Wharton Basin intraplate deformation zone. *Science Advances*, *3*(1), e1601689. http://doi.org/10.1126/sciadv.1601689

Stadler, G., Gurnis, M., Burstedde, C., Wilcox, L. C., Alisic, L., & Ghattas, O. (2010).

The Dynamics of Plate Tectonics and Mantle Flow: From Local to Global Scales. *Science*, *329*(5995), 1033–1038. http://doi.org/10.1126/science.1191223

Stein, C. A., & Stein, S. (1992). A model for the global variation in oceanic depth and heat flow with lithospheric age. *Nature*, *359*(6391), 123–129. http://doi.org/10.1038/359123a0

Subarya, C., Chlieh, M., Prawirodirdjo, L., Avouac, J. P., Bock, Y., Sieh, K., … McCaffrey, R. (2006). Plate-boundary deformation associated with the great Sumatra-Andaman earthquake. *Nature*. http://doi.org/10.1038/nature04522

Suito, H., & Freymueller, J. T. (2009). A viscoelastic and afterslip postseismic deformation model for the 1964 Alaska earthquake. *Journal of Geophysical Research: Solid Earth*, *114*(11). http://doi.org/10.1029/2008JB005954

Sun, T., Wang, K., Iinuma, T., Hino, R., He, J., Fujimoto, H., … Hu, Y. (2014). Prevalence of viscoelastic relaxation after the 2011 Tohoku-oki earthquake. *Nature*, *514*(7520), 84–7. http://doi.org/10.1038/nature13778

Tobita, M. (2016). Combined logarithmic and exponential function model for fitting postseismic GNSS time series after 2011 Tohoku-Oki earthquake. *Earth, Planets and Space*, *68*(1). http://doi.org/10.1186/s40623-016-0422-4

Wang, K. (2007). Elastic and viscoelastic models of crustal deformation in subduction earthquake cycles. *The Seismogenic Zone of Subduction Thrust Faults*, 540–575. Retrieved from ftp://ftp.gps.caltech.edu/pub/avouac/Ge177-2012/Readings/wang-review-2007.pdf

Wang, K., Hu, Y., & He, J. (2012). Deformation cycles of subduction earthquakes in a viscoelastic Earth. *Nature*, *484*(7394), 327–332. http://doi.org/10.1038/nature11032

Wang, K., Sun, T., Brown, L., Hino, R., Tomita, F., Kido, M., … Fujiwara, T. (2018).

Learning from crustal deformation associated with the M9 2011 Tohoku-oki earthquake. *Geosphere*, *14*(2), 552–571. http://doi.org/10.1130/GES01531.1

Wei, S., Helmberger, D., & Avouac, J. P. (2013). Modeling the 2012 Wharton basin earthquakes off-Sumatra: Complete lithospheric failure. *Journal of Geophysical Research: Solid Earth*, *118*(7), 3592–3609. http://doi.org/10.1002/jgrb.50267

Widiyantoro, S., & Van der HIlst Hilst, R. (1997). Mantle structure beneath Indonesia inferred from high-resolution tomographic imaging. *Geophysical Journal International*, *130*, 167–182. http://doi.org/10.1111/j.1365-246X.1997.tb00996.x

Wiens, D. A., DeMets, C., Gordon, R. G., Stein, S., Argus, D., Engeln, J. F., … Woods, D. F. (1985). A diffuse plate boundary model for Indian Ocean tectonics. *Geophysical Research Letters*, *12*(7), 429–432. http://doi.org/10.1029/GL012i007p00429

Wiens, D. A., & Stein, S. (1985). Implications of oceanic intraplate seismicity for plate stresses, driving forces and rheology. *Tectonophysics*, *116*(1–2), 143–162. http://doi.org/10.1016/0040-1951(85)90227-6

Wilson, J. T. (1965). A new class of faults and their bearing on continental drift. *Nature*, *207*(4995), 343–347. http://doi.org/10.1038/207343a0

Wu, H. H., Tsai, Y. Ben, Lee, T. Y., Lo, C. H., Hsieh, C. H., & Toan, D. Van. (2004). 3-D shear wave velocity structure of the crust and upper mantle in South China Sea and its surrounding regions by surface wave dispersion analysis. *Marine Geophysical Researches*, *25*(1–2), 5–27. http://doi.org/10.1007/s11001-005-0730-8

Yadav, R. K., Kundu, B., Gahalaut, K., Catherine, J., Gahalaut, V. K., Ambikapthy, A., & Naidu, M. S. (2013). Coseismic offsets due to the 11 April 2012 Indian Ocean earthquakes (Mw8.6 and 8.2) derived from GPS measurements.

Geophysical Research Letters, *40*(13), 3389–3393. http://doi.org/10.1002/grl.50601

Yamagiwa, S., Miyazaki, S., Hirahara, K., & Fukahata, Y. (2015). Afterslip and viscoelastic relaxation following the 2011 Tohoku-oki earthquake (M<inf>w</inf>9.0) inferred from inland GPS and seafloor GPS/Acoustic data. *Geophysical Research Letters*, *42*(1), 66–73. http://doi.org/10.1002/2014GL061735

Yoshioka, S., & Suzuki, H. (1999). Effects of three-dimensional inhomogeneous viscoelastic structures on postseismic surface deformations associated with the great 1946 Nankaido earthquake. *Pure and Applied Geophysics*, *154*(2), 307–328. http://doi.org/10.1007/s000240050231

Yue, H., Lay, T., & Koper, K. D. (2012). En échelon and orthogonal fault ruptures of the 11 April 2012 great intraplate earthquakes. *Nature*, *490*(7419), 245–249. http://doi.org/10.1038/nature11492

Zhao, S., Müller, R. D., Takahashi, Y., & Kaneda, Y. (2004). 3-D finite-element modelling of deformation and stress associated with faulting: Effect of inhomogeneous crustal structures. *Geophysical Journal International*, *157*(2), 629–644. http://doi.org/10.1111/j.1365-246X.2004.02200.x

Appendix A

Slip Distribution of Coseismic Fault Model

1. Wei et al. (2013) model

Slip distribution for Mw8.6 used in this study may found in the following link

https://agupubs.onlinelibrary.wiley.com/action/downloadSupplement?doi=10.1002%2Fjgrb.50267&attachmentId=80337379

Slip distribution for Mw8.2 used in this study may found in the following link

https://agupubs.onlinelibrary.wiley.com/action/downloadSupplement?doi=10.1002%2Fjgrb.50267&attachmentId=80337380

2. Hill et al. (2015) model

The lon and lat are the middle of the patch.
The patch length (along strike) and width (along dip) are in km
The slip is in meters.

Lon. (°)	Lon. (°)	Depth (km)	Length (km)	Width (km)	Rake (°)	Strike (°)	Dip (°)	Slip (m)

94.063538 1.909505 7.500000 31.918262 15.962667 170.000000 291.681022 70.000000 8.860852

93.797060 2.016393 7.500000 31.918262 15.962667 170.000000 291.681022 70.000000 8.717691

93.530552 2.123268 7.500000 31.918262 15.962667 170.000000 291.681022 70.000000 48.875988

93.264013 2.230122 7.500000 31.918262 15.962667 170.000000 291.681022 70.000000 43.248020

92.997440 2.336948 7.500000 31.918262 15.962667 170.000000 291.681022 70.000000 38.264669

92.730830 2.443740 7.500000 31.918262 15.962667 170.000000 291.681022 70.000000 5.908470

94.081722 1.955338 22.500000 31.918262 15.962667 170.000000 291.681022 70.000000 0.811223

93.815240 2.062235 22.500000 31.918262 15.962667 170.000000 291.681022 70.000000 2.163412

93.548728 2.169118 22.500000 31.918262 15.962667 170.000000 291.681022 70.000000 6.897006

93.282184 2.275979 22.500000 31.918262 15.962667 170.000000 291.681022 70.000000 5.000876

93.015605 2.382812 22.500000 31.918262 15.962667 170.000000 291.681022 70.000000 13.903155

92.748989 2.489610 22.500000 31.918262 15.962667 170.000000 291.681022 70.000000 2.960794

94.099907 2.001169 37.500000 31.918262 15.962667 170.000000 291.681022 70.000000 0.180820

93.833421 2.108075 37.500000 31.918262 15.962667 170.000000 291.681022 70.000000 1.282855

93.566906 2.214966 37.500000 31.918262 15.962667 170.000000 291.681022 70.000000 1.090439

93.300357 2.321835 37.500000 31.918262 15.962667 170.000000 291.681022 70.000000 1.232706

93.033772 2.428676 37.500000 31.918262 15.962667 170.000000 291.681022 70.000000 7.976866

92.767149 2.535480 37.500000 31.918262 15.962667 170.000000 291.681022 70.000000 3.900198

94.118095 2.047000 52.500000 31.918262 15.962667 170.000000 291.681022 70.000000 0.385373

93.851606 2.153915 52.500000 31.918262 15.962667 170.000000 291.681022 70.000000 0.000000

93.585085 2.260814 52.500000 31.918262 15.962667 170.000000 291.681022 70.000000 0.820763

93.318532 2.367691 52.500000 31.918262 15.962667 170.000000 291.681022 70.000000 1.704829

93.051941 2.474538 52.500000 31.918262 15.962667 170.000000 291.681022 70.000000 1.589968

92.785312 2.581348 52.500000 31.918262 15.962667 170.000000 291.681022 70.000000 1.954709

91.927603 2.799759 7.500000 30.405074 15.000000 170.000000 111.448558 90.000000 3.768973

92.182112 2.699208 7.500000 30.405074 15.000000 170.000000 111.448558 90.000000 23.472809

92.436580 2.598606 7.500000 30.405074 15.000000 170.000000 111.448558 90.000000 41.886915

91.927603 2.799759 22.500000 30.405074 15.000000 170.000000 111.448558 90.000000 4.615109

92.182112 2.699208 22.500000 30.405074 15.000000 170.000000 111.448558 90.000000 8.240546

92.436580 2.598606 22.500000 30.405074 15.000000 170.000000 111.448558 90.000000 9.725340

91.927603 2.799759 37.500000 30.405074 15.000000 170.000000 111.448558 90.000000 6.448321

92.182112 2.699208 37.500000 30.405074 15.000000 170.000000 111.448558 90.000000 6.983972

92.436580 2.598606 37.500000 30.405074 15.000000 170.000000 111.448558 90.000000 5.589521

91.927603 2.799759 52.500000 30.405074 15.000000 170.000000 111.448558 90.000000 3.521518

92.182112 2.699208 52.500000 30.405074 15.000000 170.000000 111.448558 90.000000 4.766882

92.436580 2.598606 52.500000 30.405074 15.000000 170.000000 111.448558 90.000000 2.708102

92.332738 1.462688 7.500000 31.425324 15.962667 0.000000 11.763034 110.000000 3.649054

92.390353 1.740918 7.500000 31.425324 15.962667 0.000000 11.763034 110.000000 3.075298

92.447992 2.019143 7.500000 31.425324 15.962667 0.000000 11.763034 110.000000 7.703734

92.505660 2.297360 7.500000 31.425324 15.962667 0.000000 11.763034 110.000000 9.851395

92.284710 1.472759 22.500000 31.425324 15.962667 0.000000 11.763034 110.000000 1.498832

92.342318 1.750992 22.500000 31.425324 15.962667 0.000000 11.763034 110.000000 1.577120

92.399951 2.029219 22.500000 31.425324 15.962667 0.000000 11.763034 110.000000 6.615063

92.457611 2.307440 22.500000 31.425324 15.962667 0.000000 11.763034 110.000000 3.414738

92.236681 1.482830 37.500000 31.425324 15.962667 0.000000 11.763034 110.000000 0.641392

92.294283 1.761065 37.500000 31.425324 15.962667 0.000000 11.763034 110.000000 1.324848

92.351908 2.039295 37.500000 31.425324 15.962667 0.000000 11.763034 110.000000 5.284512

92.409560 2.317519 37.500000 31.425324 15.962667 0.000000 11.763034 110.000000 3.219087

92.188651 1.492899 52.500000 31.425324 15.962667 0.000000 11.763034 110.000000 0.000000

92.246248 1.771136 52.500000 31.425324 15.962667 0.000000 11.763034 110.000000 0.284202

92.303866 2.049369 52.500000 31.425324 15.962667 0.000000 11.763034 110.000000 1.045316

92.361509 2.327596 52.500000 31.425324 15.962667 0.000000 11.763034 110.000000 0.589855

92.562556 2.563918 7.500000 28.861265 15.962667 0.000000 11.818105 110.000000 7.470827

92.615824 2.819369 7.500000 28.861265 15.962667 0.000000 11.818105 110.000000 1.491130

92.669127 3.074812 7.500000 28.861265 15.962667 0.000000 11.818105 110.000000 12.666309

92.722467 3.330246 7.500000 28.861265 15.962667 0.000000 11.818105 110.000000 3.875508

92.514507 2.574048 22.500000 28.861265 15.962667 0.000000 11.818105 110.000000 1.052385

92.567767 2.829503 22.500000 28.861265 15.962667 0.000000 11.818105 110.000000 0.507876

92.621059 3.084950 22.500000 28.861265 15.962667 0.000000 11.818105 110.000000 6.856429

92.674389 3.340389 22.500000 28.861265 15.962667 0.000000 11.818105 110.000000 3.342746

92.466458 2.584177 37.500000 28.861265 15.962667 0.000000 11.818105 110.000000 0.326044

92.519708 2.839636 37.500000 28.861265 15.962667 0.000000 11.818105 110.000000 0.302386

92.572991 3.095087 37.500000 28.861265 15.962667 0.000000 11.818105 110.000000 4.447132

92.626309 3.350530 37.500000 28.861265 15.962667 0.000000 11.818105 110.000000 3.747651

92.418408 2.594304 52.500000 28.861265 15.962667 0.000000 11.818105 110.000000 0.000000

92.471649 2.849766 52.500000 28.861265 15.962667 0.000000 11.818105 110.000000 0.224286

92.524921 3.105221 52.500000 28.861265 15.962667 0.000000 11.818105 110.000000 0.844272

92.578228 3.360669 52.500000 28.861265 15.962667 0.000000 11.818105 110.000000 2.587454

91.043312 1.554313 7.500000 33.346653 15.000000 180.000000 108.440890 90.000000 2.818652

91.327624 1.459038 7.500000 33.346653 15.000000 180.000000 108.440890 90.000000 15.532064

91.611909 1.363715 7.500000 33.346653 15.000000 180.000000 108.440890 90.000000 21.256548

91.896171 1.268351 7.500000 33.346653 15.000000 180.000000 108.440890 90.000000 9.563548

92.180412 1.172952 7.500000 33.346653 15.000000 180.000000 108.440890 90.000000 0.000000

92.464634 1.077527 7.500000 33.346653 15.000000 180.000000 108.440890 90.000000 0.090769

91.043312 1.554313 22.500000 33.346653 15.000000 180.000000 108.440890 90.000000 0.919751

91.327624 1.459038 22.500000 33.346653 15.000000 180.000000 108.440890 90.000000 4.670508

91.611909 1.363715 22.500000 33.346653 15.000000 180.000000 108.440890 90.000000 7.513954

91.896171 1.268351 22.500000 33.346653 15.000000 180.000000 108.440890 90.000000 2.088931

92.180412 1.172952 22.500000 33.346653 15.000000 180.000000 108.440890 90.000000 0.000000

92.464634 1.077527 22.500000 33.346653 15.000000 180.000000 108.440890 90.000000 0.000000

91.043312 1.554313 37.500000 33.346653 15.000000 180.000000 108.440890 90.000000 0.691081

91.327624 1.459038 37.500000 33.346653 15.000000 180.000000 108.440890 90.000000 2.502361

91.611909 1.363715 37.500000 33.346653 15.000000 180.000000 108.440890 90.000000 4.863432

91.896171 1.268351 37.500000 33.346653 15.000000 180.000000 108.440890 90.000000 0.518606

92.180412 1.172952 37.500000 33.346653 15.000000 180.000000 108.440890 90.000000 0.000000

92.464634 1.077527 37.500000 33.346653 15.000000 180.000000 108.440890 90.000000 0.000000

91.043312 1.554313 52.500000 33.346653 15.000000 180.000000 108.440890 90.000000 0.019749

91.327624 1.459038 52.500000 33.346653 15.000000 180.000000 108.440890 90.000000 0.184978

91.611909 1.363715 52.500000 33.346653 15.000000 180.000000 108.440890 90.000000 0.923710

91.896171 1.268351 52.500000 33.346653 15.000000 180.000000 108.440890 90.000000 0.007217

92.180412 1.172952 52.500000 33.346653 15.000000 180.000000 108.440890 90.000000 0.000000

92.464634 1.077527 52.500000 33.346653 15.000000 180.000000 108.440890 90.000000 0.000000

89.725477 1.683135 7.500000 33.531048 15.000000 0.000000 10.712158 90.000000 5.008530

89.781114 1.980936 7.500000 33.531048 15.000000 0.000000 10.712158 90.000000 8.124220

89.836709 2.278757 7.500000 33.531048 15.000000 0.000000 10.712158 90.000000 15.389719

89.892268 2.576597 7.500000 33.531048 15.000000 0.000000 10.712158 90.000000 28.741491

89.947794 2.874456 7.500000 33.531048 15.000000 0.000000 10.712158 90.000000 3.434271

90.003293 3.172331 7.500000 33.531048 15.000000 0.000000 10.712158 90.000000 2.775487

90.058768 3.470223 7.500000 33.531048 15.000000 0.000000 10.712158 90.000000 0.066294

89.725477 1.683135 22.500000 33.531048 15.000000 0.000000 10.712158 90.000000 1.940957

89.781114 1.980936 22.500000 33.531048 15.000000 0.000000 10.712158 90.000000 1.740455

89.836709 2.278757 22.500000 33.531048 15.000000 0.000000 10.712158 90.000000 4.708148

89.892268 2.576597 22.500000 33.531048 15.000000 0.000000 10.712158 90.000000 9.220113

89.947794 2.874456 22.500000 33.531048 15.000000 0.000000 10.712158 90.000000 0.372636

90.003293 3.172331 22.500000 33.531048 15.000000 0.000000 10.712158 90.000000 1.123992

90.058768 3.470223 22.500000 33.531048 15.000000 0.000000 10.712158 90.000000 0.290923

89.725477 1.683135 37.500000 33.531048 15.000000 0.000000 10.712158 90.000000 1.680340

89.781114 1.980936 37.500000 33.531048 15.000000 0.000000 10.712158 90.000000 0.467508

89.836709 2.278757 37.500000 33.531048 15.000000 0.000000 10.712158 90.000000 2.687499

89.892268 2.576597 37.500000 33.531048 15.000000 0.000000 10.712158 90.000000 5.295627

89.947794 2.874456 37.500000 33.531048 15.000000 0.000000 10.712158 90.000000 0.562863

90.003293 3.172331 37.500000 33.531048 15.000000 0.000000 10.712158 90.000000 0.789322

90.058768 3.470223 37.500000 33.531048 15.000000 0.000000 10.712158 90.000000 0.369874

89.725477 1.683135 52.500000 33.531048 15.000000 0.000000 10.712158 90.000000 0.856600

89.781114 1.980936 52.500000 33.531048 15.000000 0.000000 10.712158 90.000000 0.000000

89.836709 2.278757 52.500000 33.531048 15.000000 0.000000 10.712158 90.000000 0.527566

89.892268 2.576597 52.500000 33.531048 15.000000 0.000000 10.712158 90.000000 0.564100

89.947794 2.874456 52.500000 33.531048 15.000000 0.000000 10.712158 90.000000 0.528595

90.003293 3.172331 52.500000 33.531048 15.000000 0.000000 10.712158 90.000000 0.168613

90.058768 3.470223 52.500000 33.531048 15.000000 0.000000 10.712158 90.000000 0.078572

Appendix B

Other GNSS time series data with optimum model 1

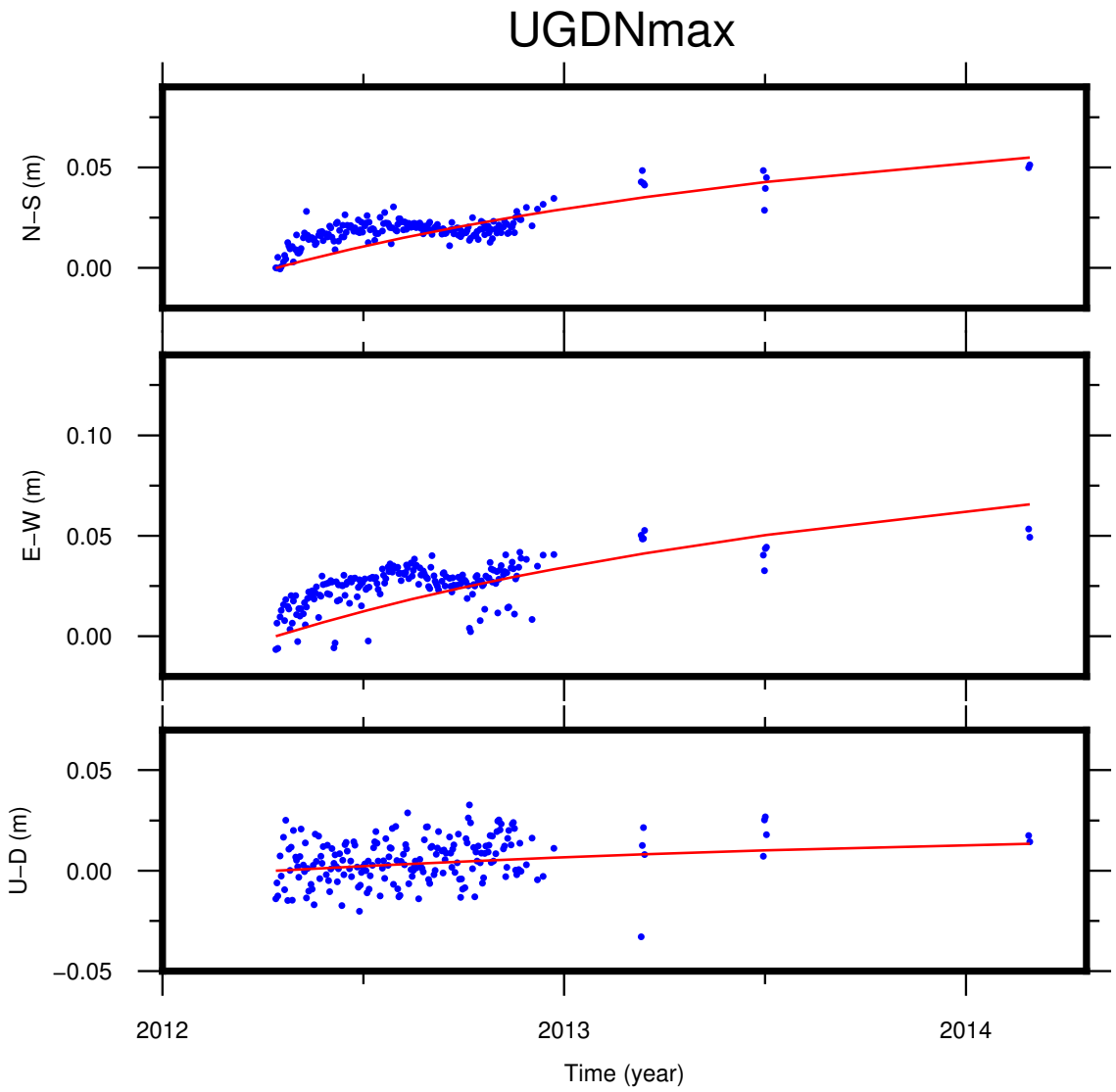

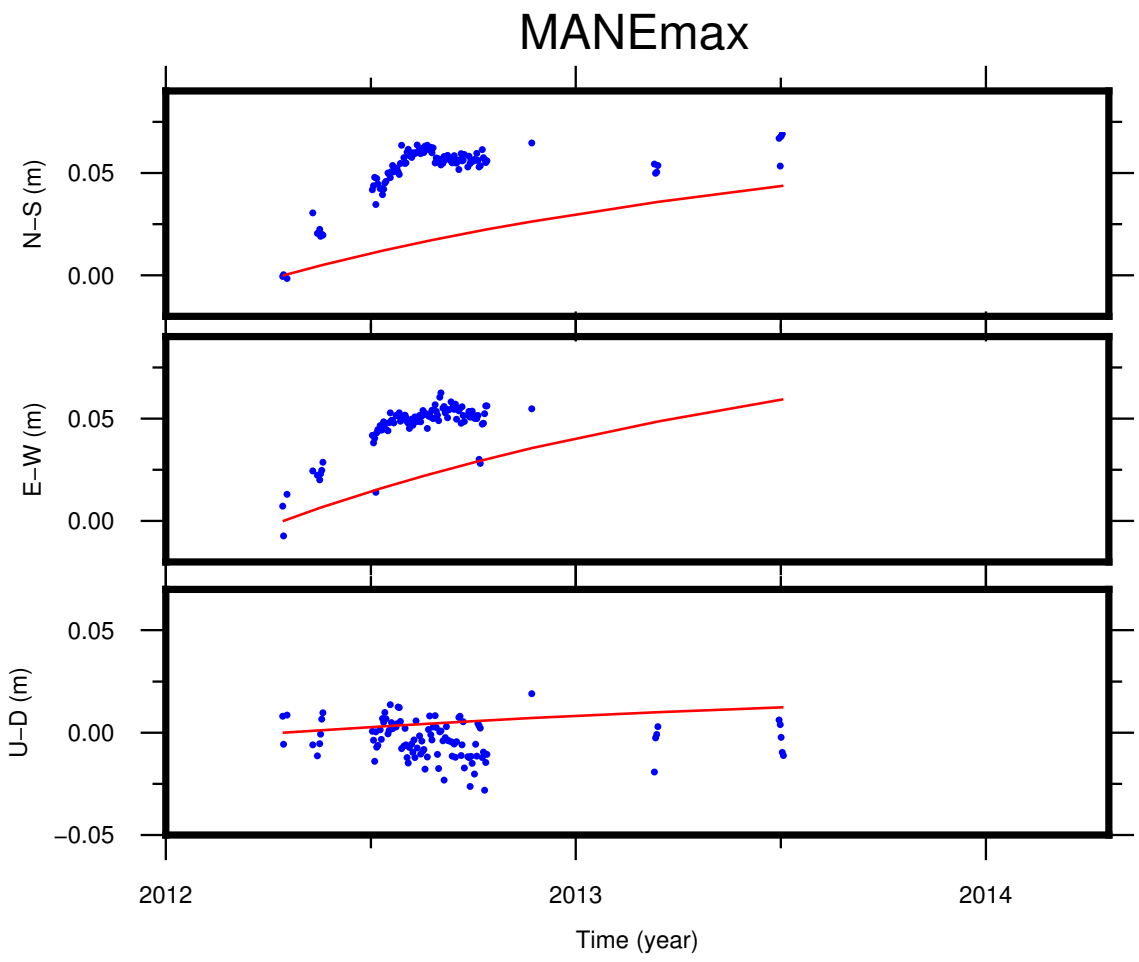
MANEmax
N–S (m)
0.05
0.00
E–W (m)
0.05
0.00
U–D (m)
0.05
0.00
−0.05
2012
2013
2014
Time (year)

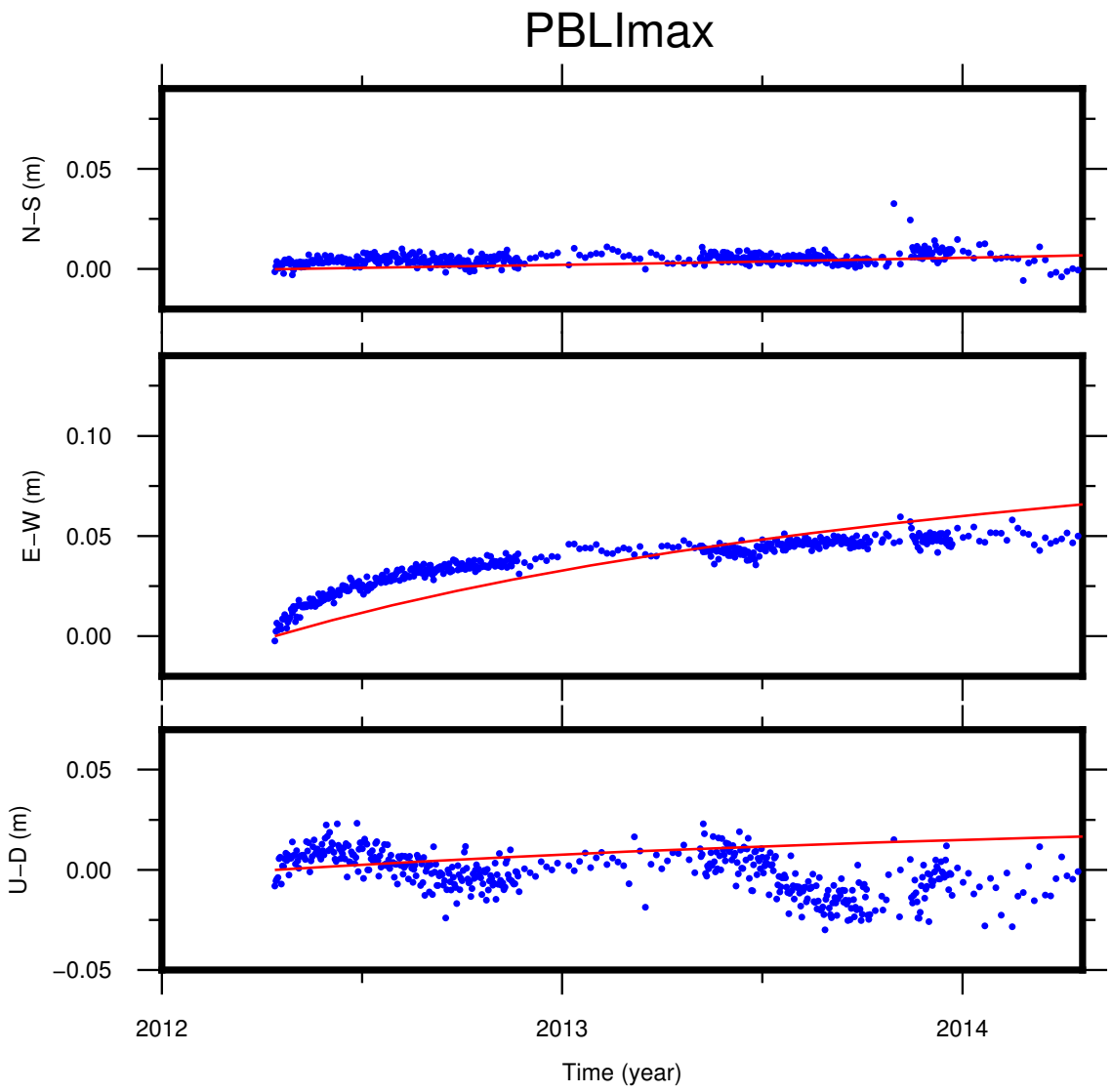
PBLImax
N–S (m)
0.05
0.00
E–W (m)
0.10
0.05
0.00
U–D (m)
0.05
0.00
−0.05
2012
2013
2014
Time (year)

Other GNSS time series data with optimum model 2

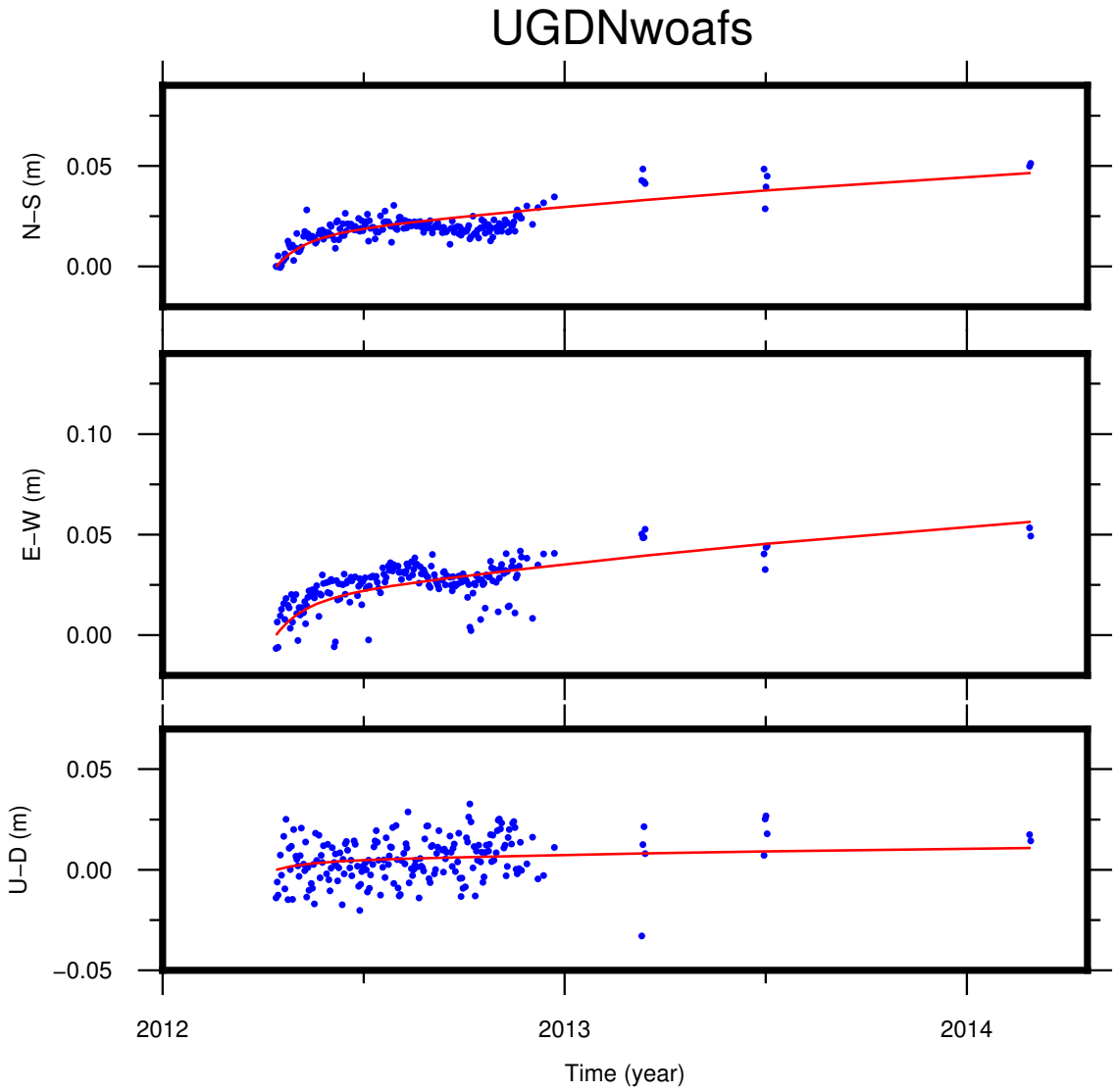

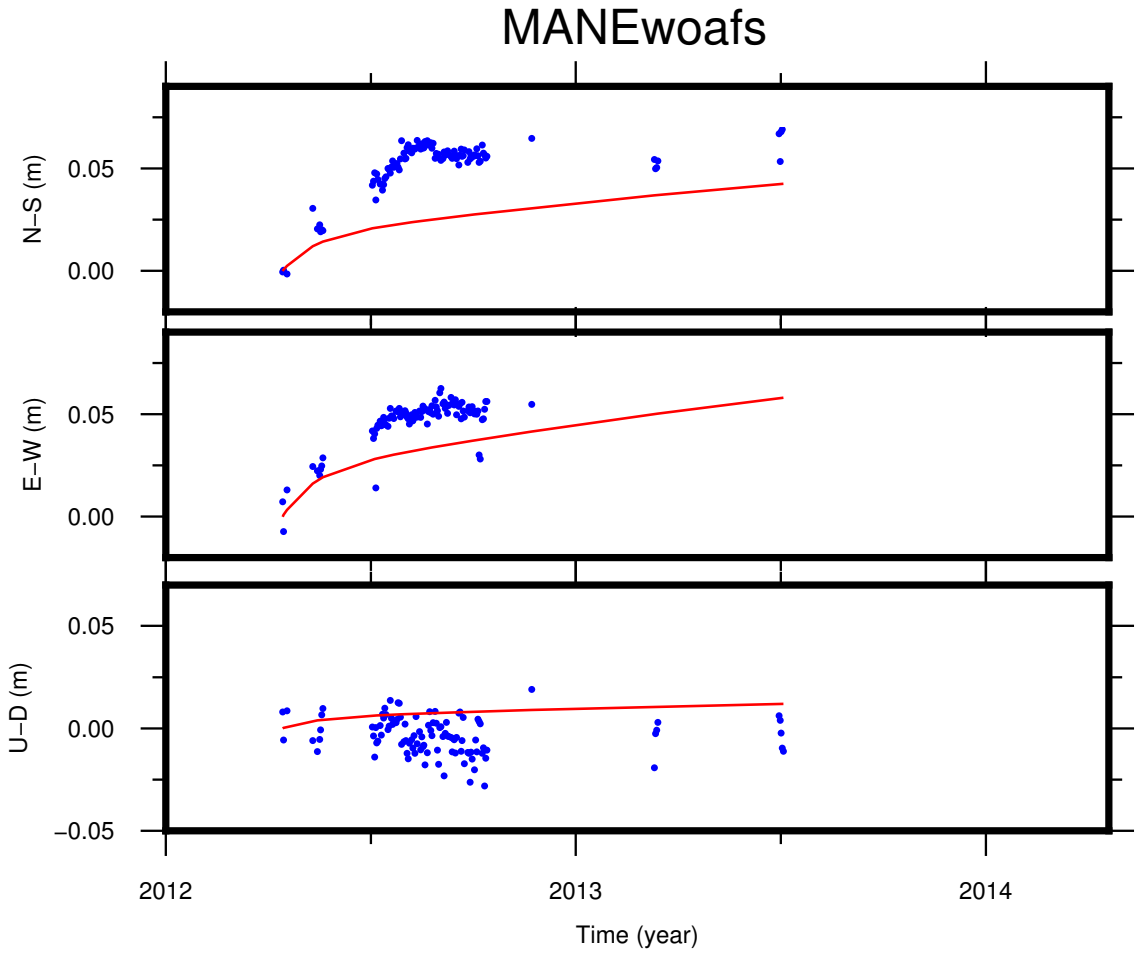
MANEwoafs
N–S (m)
E–W (m)
U–D (m)
0.05
0.00
−0.05
2012
2013
2014
Time (year)

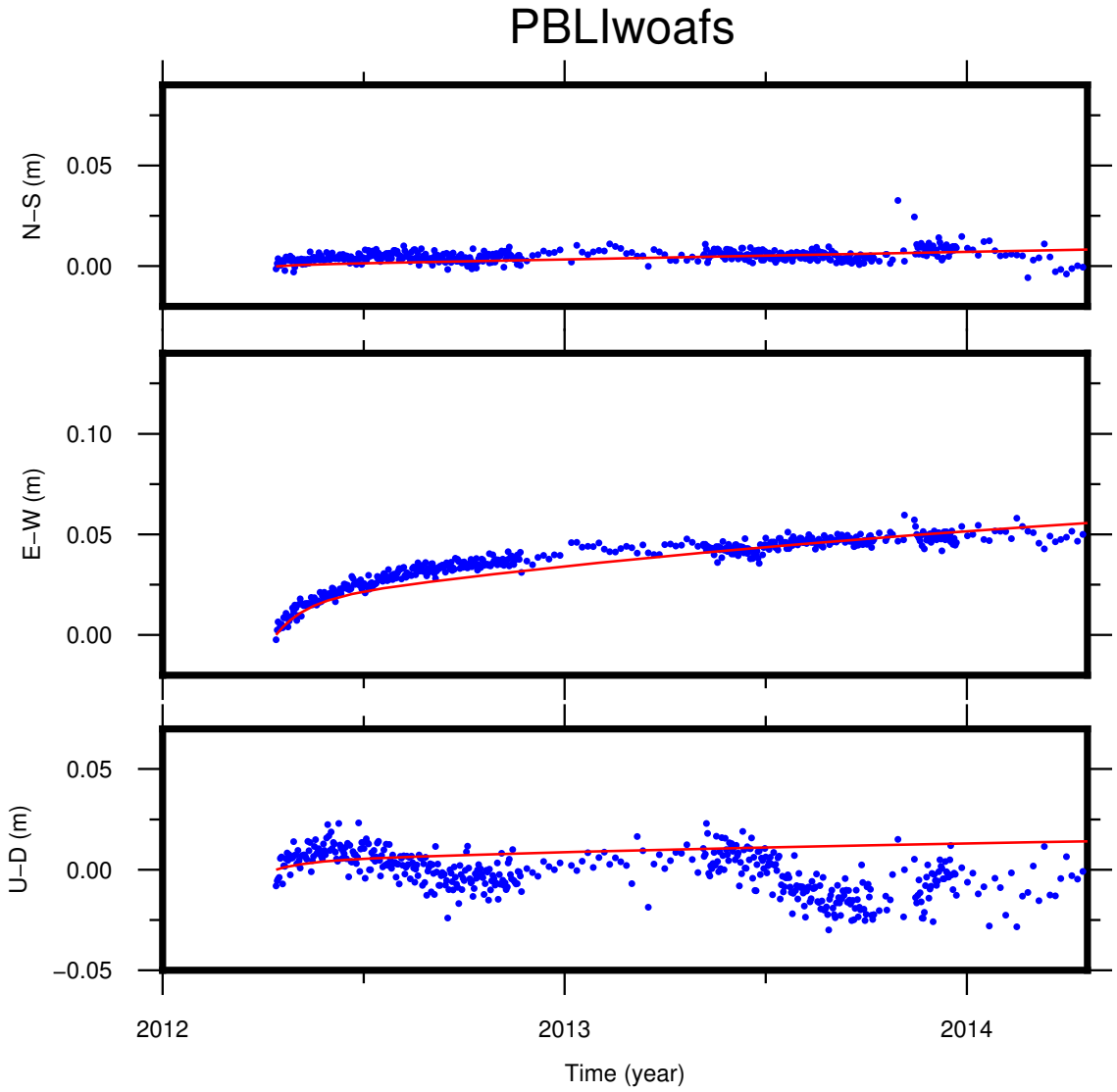
PBLIwoafs
N–S (m)
0.05
0.00
E–W (m)
0.10
0.05
0.00
U–D (m)
0.05
0.00
−0.05
2012
2013
2014
Time (year)

Other GNSS time series data with optimum model 3

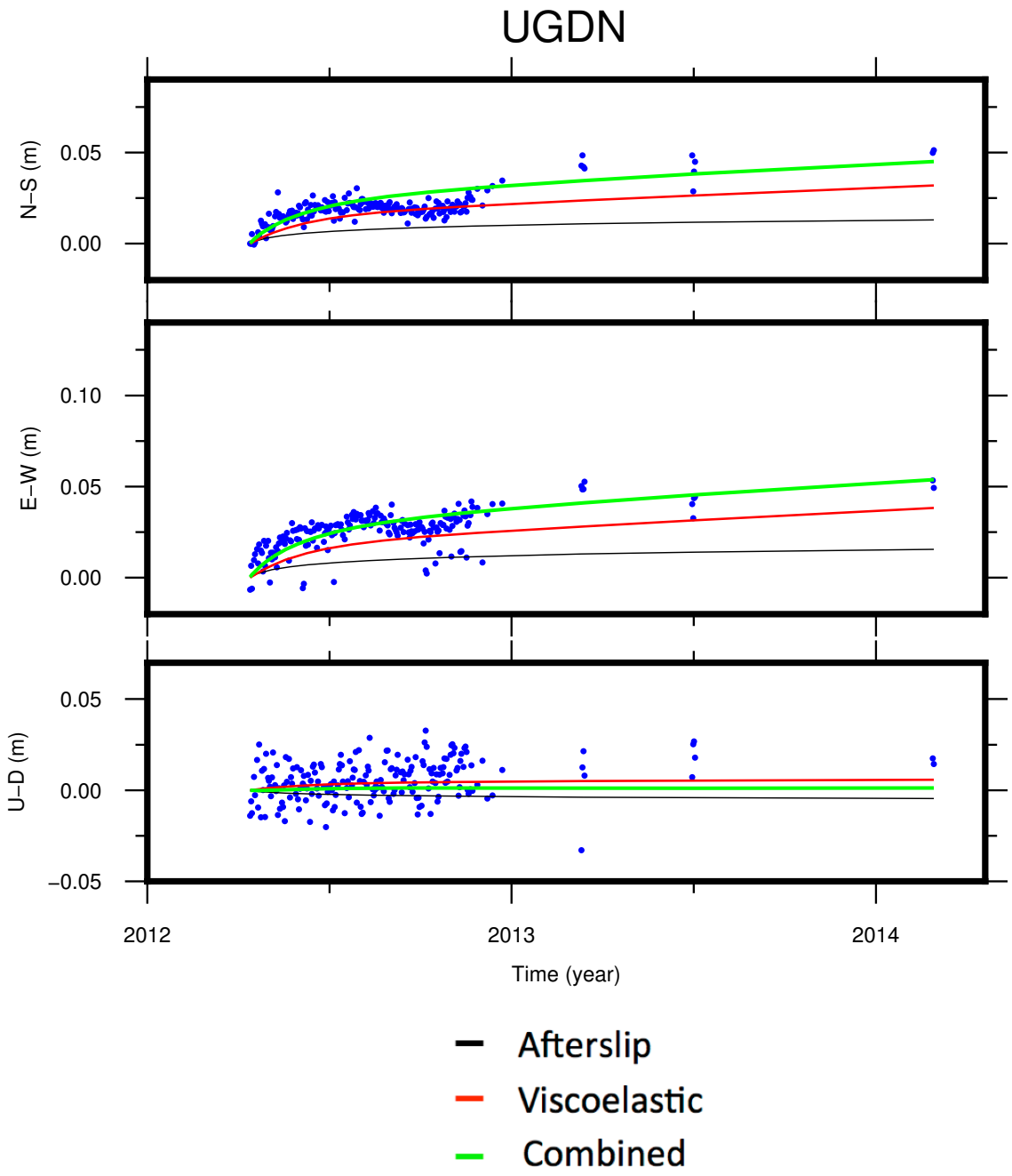

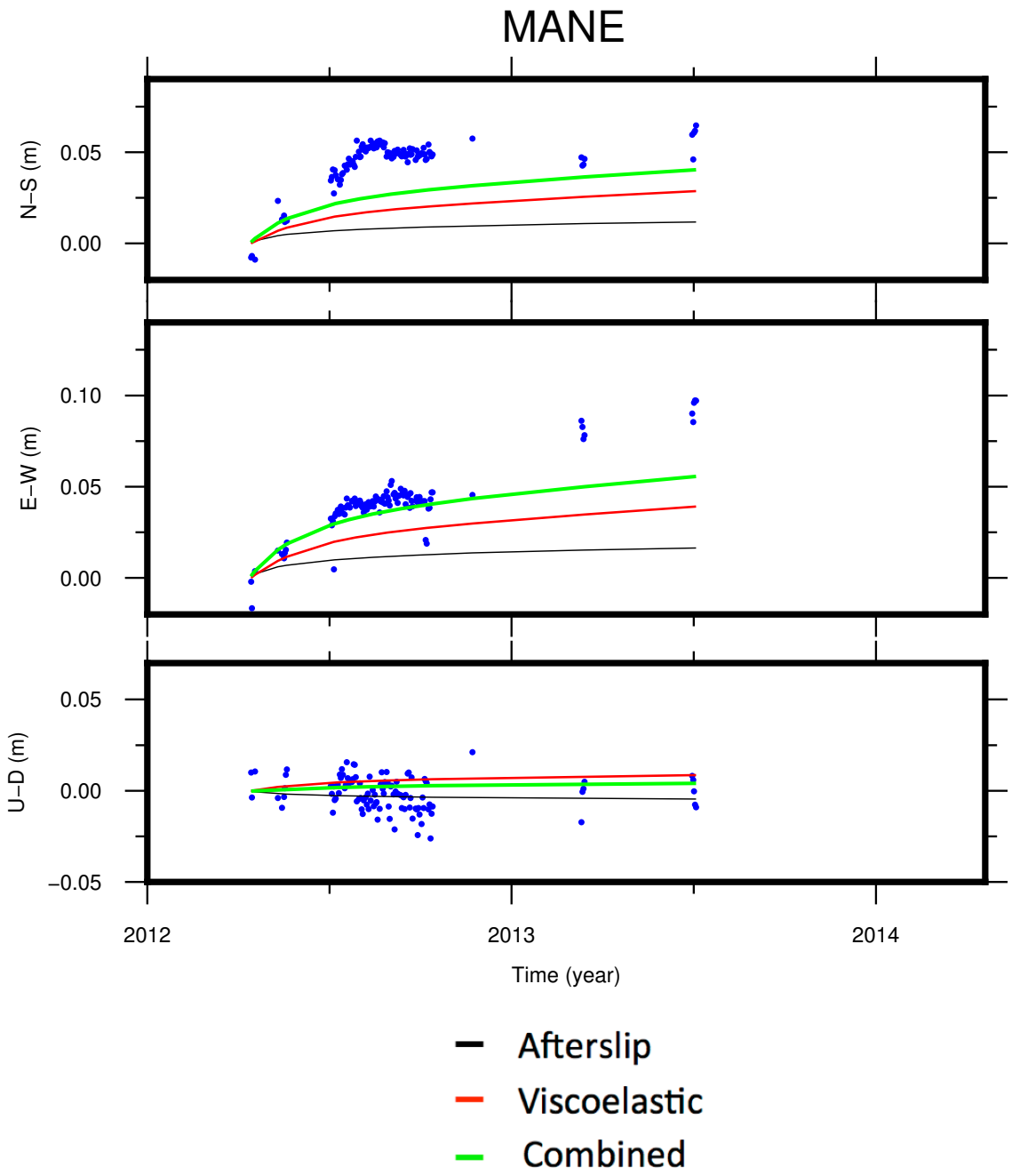
MANE
N–S (m)
0.05
0.00
E–W (m)
0.10
0.05
0.00
U–D (m)
0.05
0.00
−0.05
2012
2013
2014
Time (year)
Afterslip
Viscoelastic
Combined

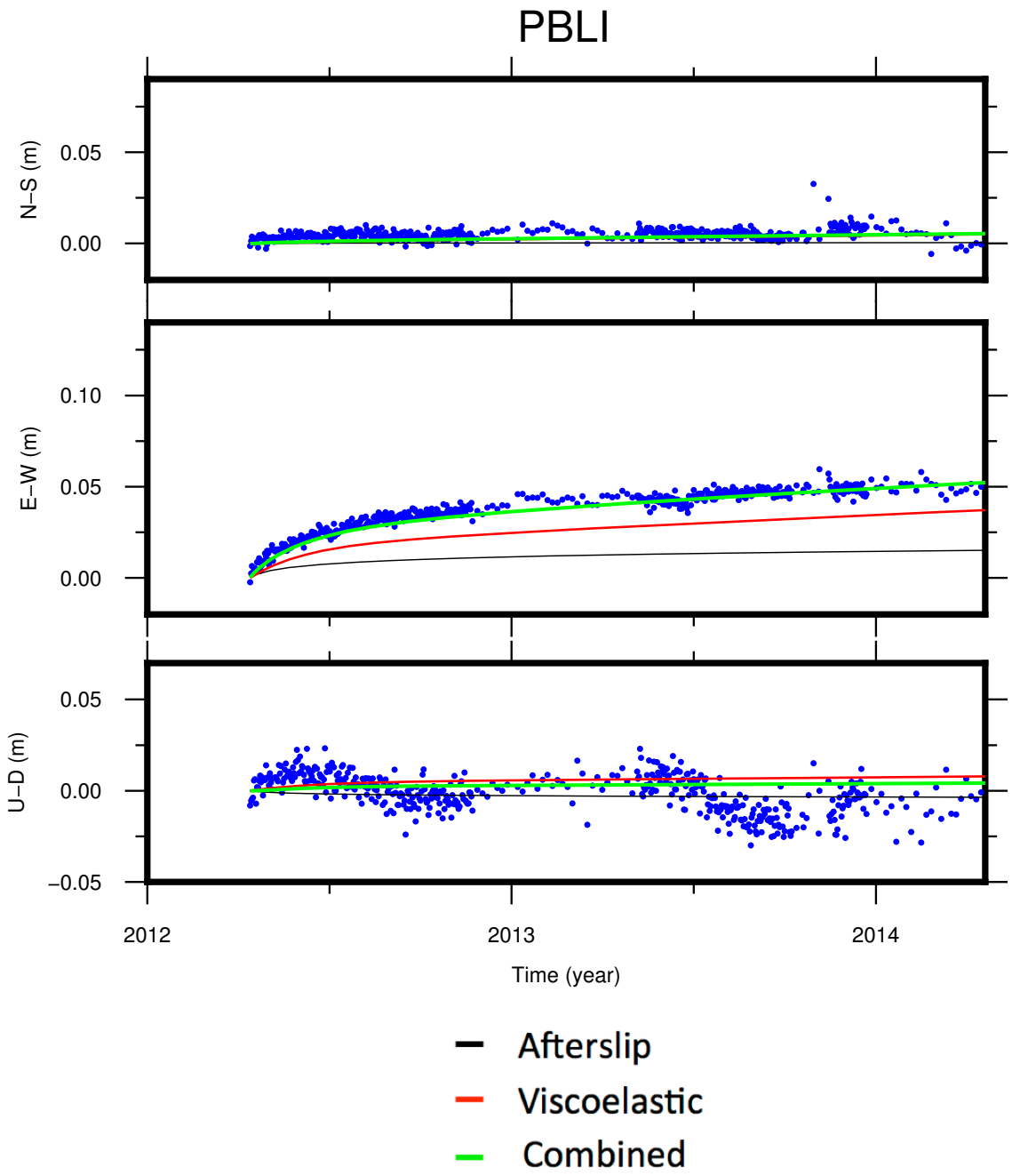
PBLI
N–S (m)
0.05
0.00
E–W (m)
0.10
0.05
0.00
U–D (m)
0.05
0.00
−0.05
2012
2013
2014
Time (year)
Afterslip
Viscoelastic
Combined

Appendix C

Chi-square Distribution Table

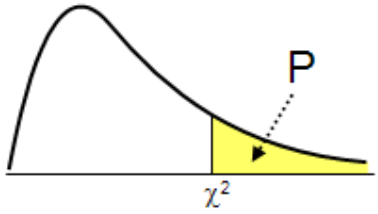

Yellow area is the probability corresponds to distribution area from the chi-square value χ^2 to positive infinity.

dof	$\chi^2_{0.05}$
10	18.307
20	31.410
30	43.773
40	55.758
50	67.505
60	79.082
70	90.531

dof	$\chi^2_{0.05}$
210	244.808
211	245.888
212	246.968
213	248.048
214	249.128
215	250.207
216	251.286

dof	$\chi^2_{0.05}$
220	255.602
230	266.378
240	277.138
250	287.882
300	341.395
350	394.626
400	447.632

Appendix D

Publications

Pratama, C., Ito T., Tabei T. (2017). Inhomogeneous spherical-earth finite element model of coseismic offset due to the 2012 Indian Ocean earthquake, AIP Conference Proceedings, 1857, 040002
http://doi.org/10.1063/1.4987066

Pratama, C., Ito T., Sasajima, R., Tabei T., Kimata, F., Gunawan E., Ohta Y., Yamashina T., Ismail N., Nurdin I., Sugiyanto D., Muksin U., Meilano I. (2017). Transient rheology of the oceanic asthenosphere following the 2012 Indian Ocean earthquake inferred from geodetic data, Journal of Asian Earth Sciences, 147, 50-59
https://doi.org/10.1016/j.jseaes.2017.07.049

Pratama, C., Ito T., Takao T., Kimata, F., Gunawan E., Ohta Y., Yamashina T., Nurdin, I., Sugiyanto D., Muksin U., Ismail N., Meilano I. (2018). Evaluation of the 2012 Indian Ocean coseismic fault model in 3-D heterogeneous structure based on vertical and horizontal GNSS observation, AIP Conference Proceedings, 1987, 0200211
https://doi.org/10.1063/1.5047296